Florian Kolb, BSc

Development of a Humidity Sensor based on Focused Electron Beam Induced PtC Deposition

MASTER THESIS

For obtaining the academic degree
Diplom-Ingenieur

Master Programme of
Technical Physics

TU Graz
Graz University of Technology
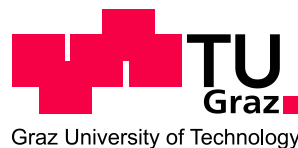
Graz University of Technology

Supervisor:

Ao.-Univ.-Prof. Dipl.-Ing. Dr. techn. Werner Grogger

Co-Supervisor:

Dipl.-Ing. Dr. techn. Harald Plank

Institute of Electron Microscopy and Nanoanalysis

Graz, May 2013

Abstract

Focused electron beam induced deposition (FEBID) is a very versatile direct write method, enabling the fabrication of 3D structures even on non-flat substrates. The deposition process is based on the interaction between electrons and functional precursor molecules on the substrate surface. The interaction process decomposes the precursor molecules into volatile fragments, which are pumped away from the vacuum chamber, and into non-volatile parts which are immobilized and therefore remain at the place of dissociation. Therefore, the controlled movement of the electron beam allows the fabrication of complex (3D) structures with specific functionalities depending on the used precursor material. For this thesis a $MePtCpMe_3$ precursor has been used which results in Pt nanograins with a diameter of about $2 - 3$ nm, embedded in a non-conducting carbon matrix. Electrical transport in such PtC metal-matrix nanocomposits is governed by tunnelling effects between adjacent Pt grains through the insulating carbon matrix in between. Defined exposure of such layers to different environmental conditions entail a conductivity variation and can therefore be used as sensing element which is content of this master thesis.

The study starts with a detailed electric basic characterization of PtC layers with different thicknesses ranging from 60 nm down to 3 nm which reveals a dimensional change of the transport regime from 3D to 2D, respectively. Time dependent investigations of electrical conductivity shows furthermore a thickness dependent self-curing effect as a result of the rapid deposition process. Subsequently, the devices have been subjected to specific gas exposure experiments including all gas components of ambient air. Error influences by means of electrode related effects and electromigration have been thoroughly conducted to exclude cross-influences. The PtC layers reveal increasing device currents during humidity exposure by polar H_2O molecules, while no effects are observed for non-polar O_2, CO_2 and N_2 gases. The sensor response is fast, fully reversible and allows quantitative humidity measurements with increasing sensitivities for decreasing device thicknesses.

A theoretic model is developed to explain the conductivity variation during exposure to polar gas molecules. The central statement of this model is that the insulating carbon matrix in between the Pt nanograins acts as transducing element in the presence of polar molecules by a decrease of its dielectric constant. This variation leads then to a higher tunnelling probability for charge carries in neighbouring Pt grains and by that to a higher electric current through the device. The model is furthermore supported mathematically by deriving a sensitivity factor as function of the dielectric matrix constant which is in good agreement with the experimental observations.

This study represents the development of the first gas sensor worldwide which is based on focused electron beam induced deposition and shows clear potential for special industrial applications due to their simple fabrication and the high performance.

Kurzfassung

Die Abscheidung mittels fokussierten Elektronenstrahlen ist eine vielseitige, sogenannte direkte Schreibmethode, welche die Herstellung von 3D Strukturen selbst auf unebenen Oberflächen ermöglicht. Der Abscheidungsprozess basiert auf der Wechselwirkung zwischen Elektronen und funktionellen Precursormolekülen an der Probenoberfläche. Die Interaktionen spalten die Precursormoleküle in flüchtige Komponenten, welche aus der Probenkammer abgepumpt werden, und nichtflüchtige Komponenten auf, welche aufgrund ihrer Unbeweglichkeit am Platz des Aufspaltungsprozesses verbleiben. Die kontrollierte Bewegung des Elektronenstrahles ermöglicht die Erzeugung von komplexen (3D) Strukturen mit spezifischen Eigenschaften, welche durch die jeweilig verwendeten Precursormaterialien gegeben sind. In der vorliegenden Master Thesis wurde MePtCpMe3 als Ausgangsmaterial verwendet, welches aufgrund des Abscheidungsprozesses zur Bildung von Pt Nanokristallen im Bereich von 2 - 3 nm führt, welche in einer nichtleitenden Kohlenstoffmatrix eingebettet sind. Der Ladungstransport in derartigen PtC Metall-Matrix Verbundmaterialien wird durch Tunneleffekte zwischen benachbarten Pt Körnern bestimmt, welche durch die nichtleitende Kohlenstoffmatrix getrennt sind. Die kontrollierte Aussetzung derartiger Metall-Matrixstrukturen unter verschiedenen Umgebungsbedingungen bedingt eine Veränderung der Leitfähigkeit, weshalb sie sich als Sensorelemente eignen was das Kernthema dieser Masterthesis darstellt.

Die Studie startet mit einer detaillierten Charakterisierung der elektrischen Grundeigenschaften unterschiedlich dicker PtC Strukturen im Bereich zwischen 60 nm und 3 nm, welche eine Änderung des räumlichen Ladungstransportregimes von 3D auf 2D erkennen lassen. Die zeitabhängigen Untersuchungen der elektrischen Leitfähigkeiten weisen darüber hinaus einen dickenabhängigen self-curing Effekt auf, welcher durch den sehr schnellen Abscheidungsprozess bedingt ist.

In weiterer Folge wurden die Proben unterschiedlichen Gasen ausgesetzt, welche Bestandteile gewöhnlicher Umgebungsluft sind. Eine sorgfältige Untersuchung von Fehlereinflüssen, unter anderem bedingt durch die verwendete Elektrodenstruktur sowie durch Elektromigration, wurde durchgeführt um mögliche Nebeneinflüsse auszuschließen. Die PtC Strukturen weisen in der Gegenwart von polaren H_2O Molekülen einen Anstieg des elektrischen Stromes auf, während nichtpolare Gase wie O_2, CO_2 und N_2 keine Reaktion verursachen. Die Sensoren reagieren schnell, vollständig reversibel und erlauben die quantitative Messung der Luftfeuchte mit erhöhter Empfindlichkeit bei abnehmender Probendicke.

Die Entwicklung eines theoretischen Modelles ermöglicht die Erklärung der Leitfähigkeitsänderungen unter Einfluss von polaren Gasmolekülen. Die zentrale Aussage dieses Modelles beinhaltet, dass die dielektrische Konstante der isolierenden Kohlenstoffmatrix zwischen den Pt Kristallen als vermittelndes Element fungiert und in der Gegenwart von Wassermolekülen abnimmt. Diese Änderung führt zu einer erhöhten Tunnelwahrscheinlichkeit der Ladungsträger zwischen den Pt Kristallen wodurch ein höherer elektrischer Strom durch die Probe ermöglicht wird. Darüber hinaus wird das entwickelte Modell mathematisch durch die Herleitung eines Sensitivitätsfaktors in Abhängigkeit der dielektrischen Konstante unterstützt, welcher sich im Einklang mit den experimentellen Beobachtungen befindet.

Die vorliegende Arbeit repräsentiert die Entwicklung des weltweit ersten Gassensors auf Basis von fokussierter Elektronenstrahlabscheidung und zeigt deutlich das Potential für spezielle, industrielle Anwendungen aufgrund der einfachen Herstellung und der Leistungsfähigkeit.

Acknowledgements

Table of Contents

List of Abbreviations

AE	…	*Auger electron*	LIMS	…	*liquid ion metal source*
AFM	…	*atomic force microscopy*	LLE	…	*low loss electron*
BSE	…	*backscattered electrons*	LPF	…	*low pass filter*
c-VRH	…	*correlated-variable range hopping*	MTL	…	*mass transport limited*
DBM	…	*dual beam microscope*	PoP	…	*point pitch*
DT	…	*dwell time*	PSD	…	*position sensitive detector*
EDXS	…	*energy dispersive x –ray spectroscopy*	RGB	…	*red, green, blue*
ETD	…	*Everhart-Thornley detector*	RRL	…	*reaction rate limited*
FEBID	…	*focused electron beam induced deposition*	SE	…	*secondary electron*
FIBID	…	*focused ion beam induced deposition*	SEM	…	*scanning electron microscope*
FEG	…	*field emission gun*	TEM	…	*transmission electron microscope*
FWHM	…	*full width half maximum*	TLD	…	*through the lens detector*
GIS	…	*gas injection system*	WD	…	*working distance*
GUI	…	*graphical user interface*	FIB	…	*focused ion beam*
HME	…	*humidity measurement environment*	TET	…	*total exposure time*
LED	…	*light emitting diode*			

1 Introduction

In recent years the interest on the detection of different gas species like O_2, O_3, CO, CO_2, SO_2, NH_3 and H_2O has attracted increasing attention due to their manifold application ranges, such as environmental monitoring, automotive emission, industrial process control and so on. The list of requirements for specialized sensors is quite long, very demanding and sometimes even contrary. Ideally, they should be 100 % selective but tunable for a wide range of different gas species in order to determine the individual composition with low detection limits in the ppm range even under harsh conditions. Furthermore, they should be easy to fabricate at low costs, show compact dimensions and should not demand special operation conditions like high temperatures and / or time consuming reformation cycles after the gas detection. Finally, the read-out should be easy and fast without the necessity of expensive equipment.

Although it is practically impossible to meet all requirements, many different sensor concepts have been developed e.g. using mass sensitive, optical, resistive or capacitive detection designs. The sensor materials include typically metal-oxides, metal nanoparticles, carbon nanotubes or thin-film polymers. Capacitive sensor designs belong to the most commonly used sensor principle consisting of a dielectric polymer which is used as a transducing material via swelling and / or dielectric constant variation during gas exposure and the entailed gas absorption by the polymer. Both reactions lead to a change of the capacitance which is either directly detected via counter-electrodes or realized by the implementation of such polymer films as gate dielectric in field effect transistors. However, these concepts show often drawbacks like sophisticated fabrication procedures which are time and cost intensive, or long reformation cycles leading to slow detection rates. Consequently, a perfect sensor concept meeting all or at least almost every requirement has not yet been developed independently on the aimed gas type to be detected.

During the last decade focused electron beam induced deposition (FEBID) of gaseous precursor molecules has attracted considerable attention due to the ability to fabricate multifunctional structures with spatial nanometer resolution. As a big advantage, FEBID is a mask less technique without the need of any pre- or post-preparation steps as for resist based lithography approaches, giving FEBID the character of a direct-write tool. Initially, this technique had also the reputation of a prototyping tool as a result of slow deposition rates and small writing fields. However, strong efforts with respect to fundamental relations between process parameters, morphology and chemistry has brought FEBID in a state of maturity where such process can also be applied in full-scale productions together with the current introduction of multi-electron-beam instrumentations (up to 500.000 electron beams simultaneously).

Compared to the faster deposition via focused ion beams, FEBID provides higher spatial resolution and does not show sputtering effects, high thermal stress or unwanted ion implantation which can alter or even inhibit the intended functionality of the precursor which can be conductive, semi-conducting, insulating, magnetic, or optical. Functional FEBID nanostructures have a wide field of application like repair of photomasks used in lithography, fabrication of on-demand electrodes in mix-and-match applications, tip modification for atomic / magnetic / electrical force microscopy, or the direct fabrication of photonic structures.

Beside these passive applications, so far only two types of active devices have been demonstrated during the last years: 1) Co based precursor have been used for the fabrication of nanosized Hall sensor with outstanding properties; and 2) the special metal-matrix structure of Pt based precursor was used as stress strain sensor due to varying inter-grain distances and the entailed electrical response. The present master thesis demonstrates the third FEBID based sensor concept in general and the first gas sensing device which reveals the enormous potential of this direct-write method.

2 Instrumentation and Pre-work

2.1 Dual Beam Microscope (DBM)

2.1.1 Basic Concept

The dual beam microscope (**DBM**) is a combination of a scanning electron microscope (**SEM**) and a focused ion beam microscope (**FIB**). The setup enables the investigation of a specific area of the sample with both beams simultaneously (Figure 1, left) or independently depending on the individual purpose. The DBM allows the SEM analysis of a specimen surface as well as subsurface regions by local material removal via ion milling with the FIB (Figure 1, left). Such DBMs are often equipped with an energy dispersive X-ray spectroscopy (**EDXS**) system for qualitative and quantitative chemical analysis as well as for laterally resolved elemental mapping of specific regions. The DBM used during this Master Thesis is a NOVA 200 Nanolab from FEI (Figure 1, right) [1], additionally equipped with a XFlash 4010 EDXS system from BRUKER [2].
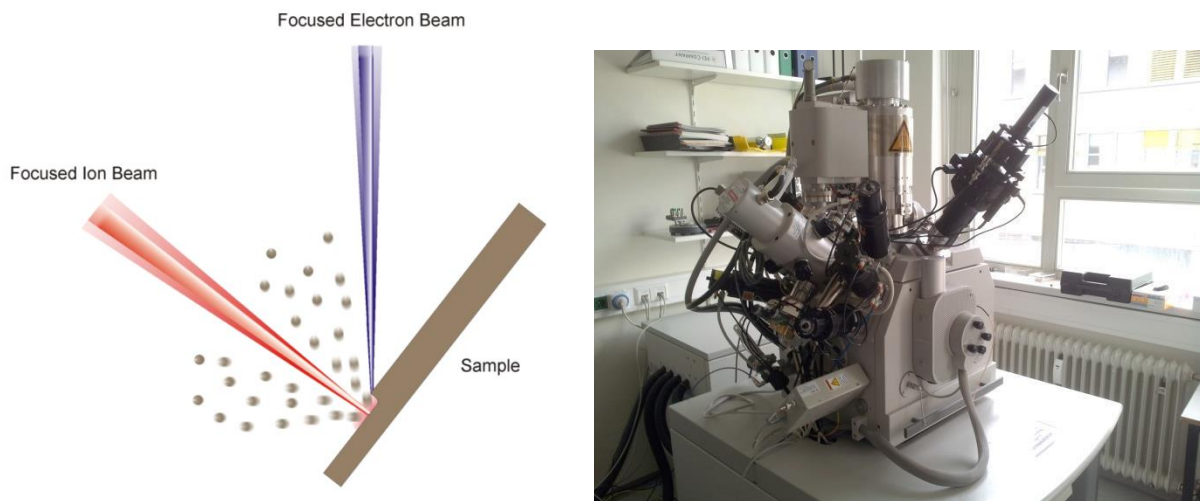
Figure 1: left: the dual beam concept which allows for simultaneous electron and ion beam microscopy [3]; right: the NOVA200 Nanolab (FEI) used during this master thesis.

DBMs can be used in manifold ways such as electron / ion beam related metrology, chemical analyses, subsurface investigations, 3D bulk reconstructions or nanofabrication applications which is the main part of this thesis. Most established, however, is the DBM based site-specific preparation of ultrathin lamellas with thicknesses below 50 nm as can be seen in Figure 2 from a front (left and top view (right). Such lamellas are needed for transmission electron microscopy (**TEM**) related investigations which allow insights down to subatomic resolutions [4].
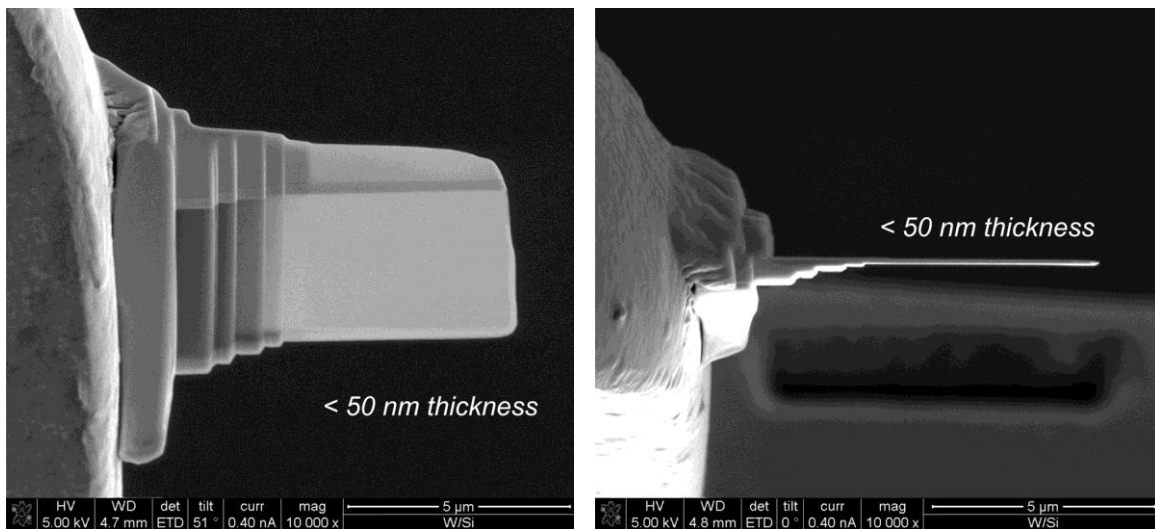
Figure 2: SEM image of a DBM prepared lamella in a front (left) and in a top (right) view [3] typically used for TEM investigations.

FIB based nanofabrication becomes more and more interesting due to the direct write character and the possibility of fast adaption to actual problems which gives DBMs the status of a rapid prototyping tool for the micro- and nanoscale. Figure 3 shows just two examples about the variable 3D structuring possibility (a) or the direct fabrication of plasmonic gold structures via subtractive FIB milling (b).

a)   *b)*
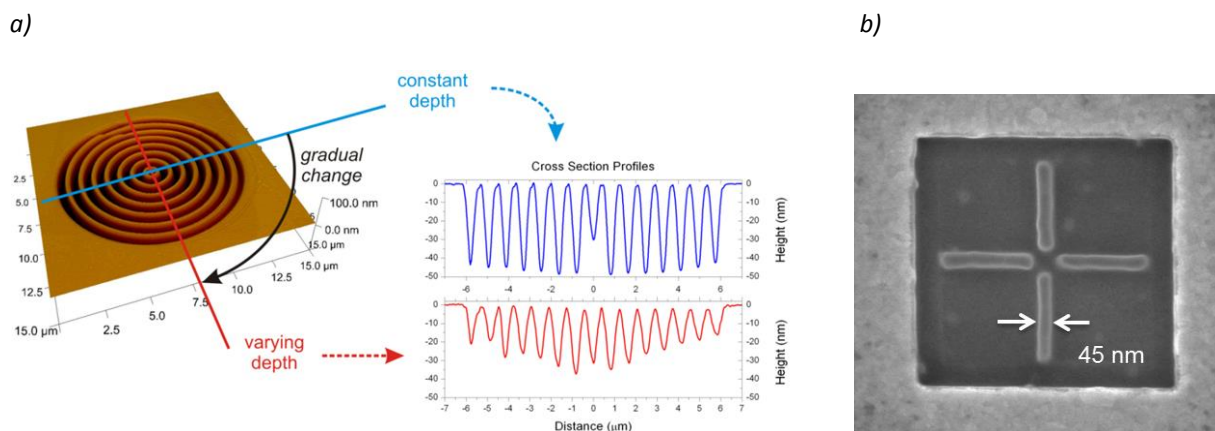
Figure 3: direct write prototyping capabilities of a FIB system by means of variable 3D control (a) or the direct fabrication of plasmonic nanostructures (Au on SiO$_2$) as shown in b) [3].

By the manifold possibilities of DBMs such microscopes have become an integrative part for science and industry during the last decade. The present thesis will focus on the additive fabrication of functional nanostructures via the electron beam which attracts more and more attention during the last few years. This work presents the worldwide first gas sensor based on this technique which indicates an important step forward for the community and might open industrial interest for special purposes.

2.1.2 Scanning Electron Microscope (SEM)

The SEM focuses an electron beam down to the nanometre range and moves it systemically over a specific region of the specimen. It is very versatile with respect to the magnification, covering a range from a few millimetres down to the nanometre scale (Figure 4), allowing overview inspections of large areas or high resolution investigations on the nanoscale, respectively. The inspected specimens have to be electrical conductive or at least coated with a conductive layer and have furthermore to be suitable for SEM high vacuum conditions in classical SEMs like the DBM used. The main parts of a SEM are the source where the electrons are generated, electromagnetic or electrostatic lenses for focussing and rastering the beam and relevant detectors, making the specimen and its properties accessible for the operator at the desired information.
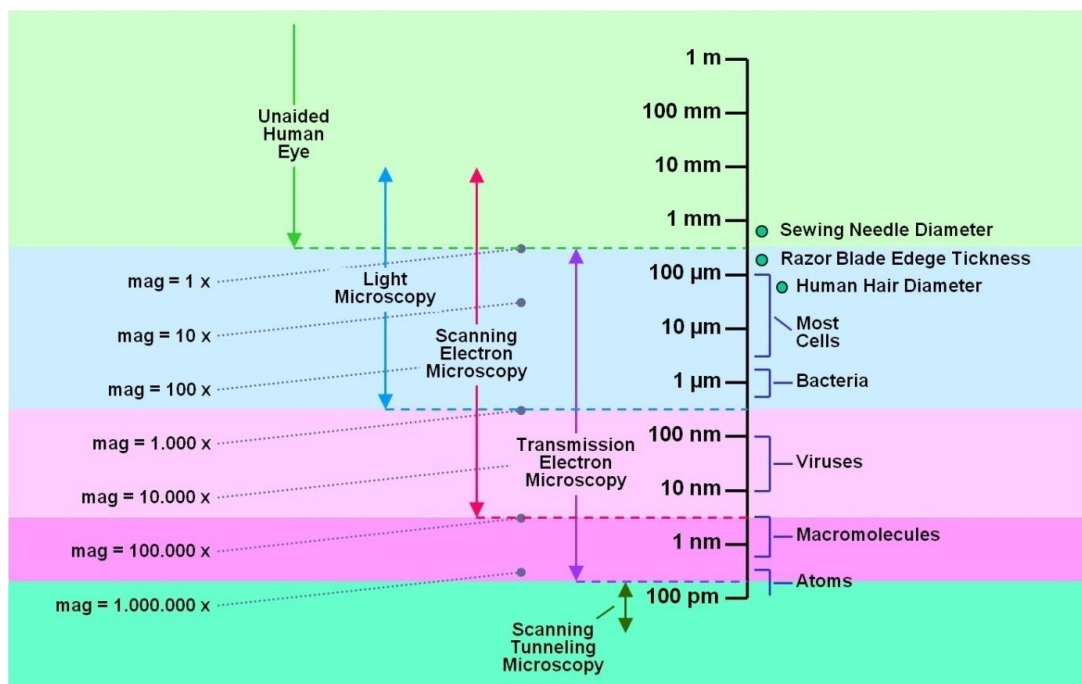
Figure 4: magnification abilities for different types of microscopes [25].

2.1.3 Electron Source and Lenses

The starting point for an electron on its way down to the surface of the specimen is the electron gun. Their purpose is to establish a highly stable flow of electrons in a small beam diameter. The electron current can be generated in different ways, like thermionic emission in a Tungsten filament (Figure 5a), via LaB_6 elements (Figure 5b), or by field emission guns (**FEG**, Figure 5c). Their characteristics differ with respect to the brightness or the life-time [5]. A very common type of thermionic FEGs utilizes a heated tungsten wire, which is additionally exposed to a strong electric field. This design lowers the thermic energy needed to generate the electron current and the emission mechanism is established through tunnelling of the electrons from the curved metal tip outside. Subsequently the electrons are focused by a grid cap, the so called Wehnelt cylinder, into the first cross-over which is constant independently on finally used beam energies and currents (Figure 5d).
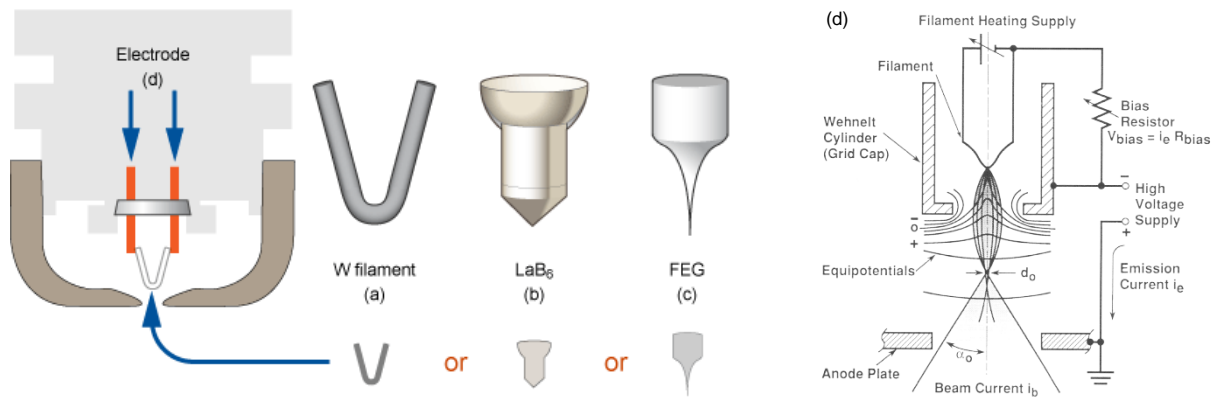
Figure 5: left: filament in form of a tungsten hair pin emitting the electron current; right: FEG scheme including the Wehnelt cylinder and the most important first crossover d₀ [5].

The main purpose of the electron lenses is to demagnify the image of the bundled electron beam after departing the grid cap (d_0, Figure 5). Electron beams can be focussed either by electrostatic or electromagnetic fields. Due to their lower inherent aberrations electromagnetic lenses are commonly used for focussing the electron beam, while electrostatic lenses are used for bundling ion beams. The basic design of an electromagnetic lens can be seen in Figure 6. An electron with the velocity $\vec{v}_z$ enters the area between the two pole pieces. In this area a homogenous magnetic field is generated by an electric current flowing through the windings of the integrated lens coil. The magnetic field $\vec{B}$ can be separated in the two components $\vec{B}_z$ and $\vec{B}_r$ which interact with the electron. Consequently, the electron is forced to change its direction towards the optical axis. As a result of this interaction the electron beam is focussed (Figure 6).
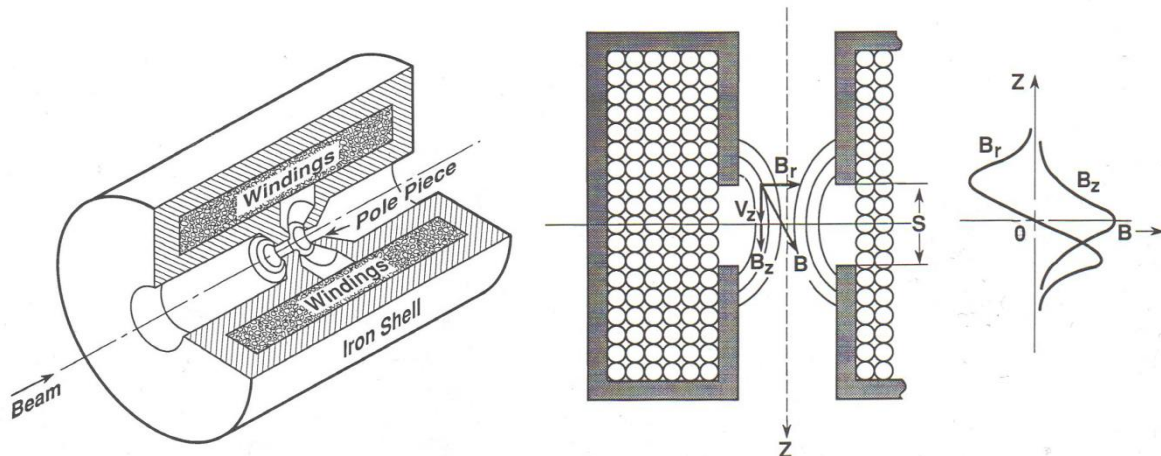
Figure 6: left: internal of an electromagnetic lens, typical used in a SEM; right: schematic cross-section of the electromagnetic lens with the magnetic flux B_r and B_z in the lens including the plot of the magnetic components along the optical axis [5].

Figure 7 shows conceptual design of the electron column for the used DBM. The electron beam is accelerated by applying a voltage of 30 kV, subsequently passing the condenser lens system C1 and C2. This lens system shrinks further the diameter of the beam and aligns the electron beam by centring and parallelizing it to the optical main axis. Before the aperture, the finally desired electron energy is achieved by appropriate deceleration lenses. The beam movement is controlled by 2 subsequent duplex lenses DC_{UPPER} and DC_{LOWER}, moving the beam in X and Y direction, respectively.

Axial astigmatism, a lens error which will be discussed in detail in chapter 2.1.6, is also corrected by those two lenses because of the isolated X and Y character of the duplex lens systems. Finally, the electron beam is focussed onto the specimen with the objective lens (search lens and UHR lens in normal and high resolution mode, respectively).
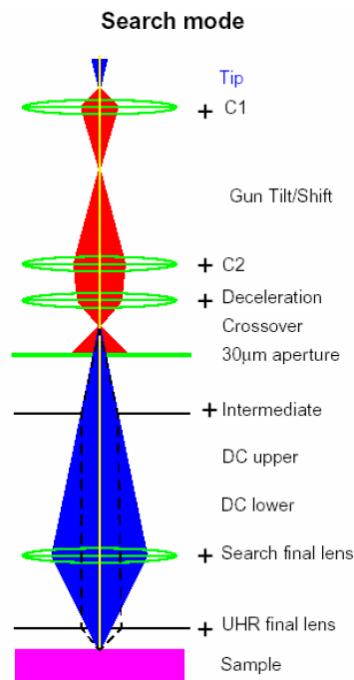
Figure 7: design of the SEM lens system for the used DBM [1].

Considering an electron beam, free of aberrations and axial astigmatism, the size of the beam on the substrate can be described as a radially distributed electron flux on the surface plane of the substrate. The flux can usually be described by a Gaussian distribution

$$f(r) = \frac{\left(I_p/e\right)}{2\pi a^2} \exp\left(\frac{r^2}{2a^2}\right)$$

<div align="right">Equation 1</div>

where *f(r)* has the unit electron per unit area and time, I_p the electron current normalized by the elementary charge *e* and the standard deviation described by the term *a*. However, with this definition the intensity electron beam is not radially uniform. Therefore, the size of the beam is described in different ways such as the *1/e*, *1/e²*, the full width half maximum (**FWHM**) or the full width including 50 % or 90 % of the incident electrons (Figure 8 left). The size of the beam is also affected by the so called working distance (**WD**) which is the distance between the final lens aperture and the surface of the sample. The size of the beam is slightly decreased by a smaller working distance but in case of electron beam induced deposition processes the choice of the working distance is limited due to the required space for the gas injection systems.
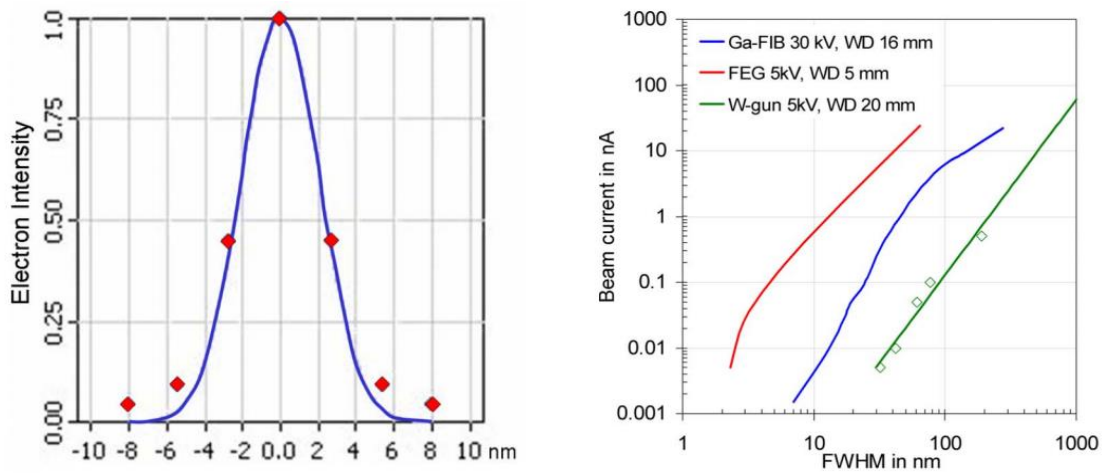
Figure 8: left: Gaussian distribution of a focused electron beam with a FWHM = 4.4 nm; right: beam current in dependence on the FWHM for an electron point source (Schottky field emission gun, FEG), ion beam (liquid Ga metal source) and a thermionic W filament [12].

Another very important characteristic of the electron beam is the beam energy and its spatial distribution within the bulk and on the surface in particular which affects strongly dissociation processes during deposition (see chapter 2.1.10). The beam current is classically defined by amount of electrons (=charge) per unit time impinging on the substrate surface which influences the size of the beam by increasing diameters for increasing currents (Figure 8 right). Furthermore, the beam current has also an effect on the dissociation process due to different levels of depletion (growth rates) but also on the finally achievable chemistry (see chapter 2.1.10).

2.1.4   Electron – Matter Interaction and Detection

After the electron beam has penetrated the specimen surface the electron trajectories changes due to the interaction processes with the electron clouds of the specimen [5]. This interaction is also called scattering and can be divided in two different cases: 1) inelastic scattering where energy is exchanged; and 2) elastic scattering process where the electron energy is conserved. Both scattering types lead to a change of the propagation direction of the electron, where elastic scattering processes shows larger scattering angles as schematically shown in Figure 9 at the left [5]. The total volume where interaction takes place is called interaction volume which is typically pear shaped (Figure 9 at the right by means of a Monte Carlo simulation [6]). Inelastic scattering transfers the energy from the electron to the particles of the specimen, subsequently generating secondary electrons (**SE**), phonons, X-rays and Auger electrons [5]. The last two products of the inelastic scattering are caused by the ionization of the inner core shells of the atoms in the specimens.

Considering the energy distribution from surface emitted electrons as shown in Figure 10, the low energy range up to 50 eV is defined as the SE range. Due to this low energy such SE cannot travel very far (typically clearly less than 10 nm [5]) and stem therefore from a 10 nm voxel close to the surface. Beside SE, a fraction of the incident electrons can be scattered back out from the sample. These electrons are called back scattered electrons (**BSE**) and have a higher energy than the SE since elastic scattering events are mainly responsible for the BSE emission [5]. Consequently, they originate from deeper regions of the specimen which depends on the primary electron energy but also from the material used as substrate [5].
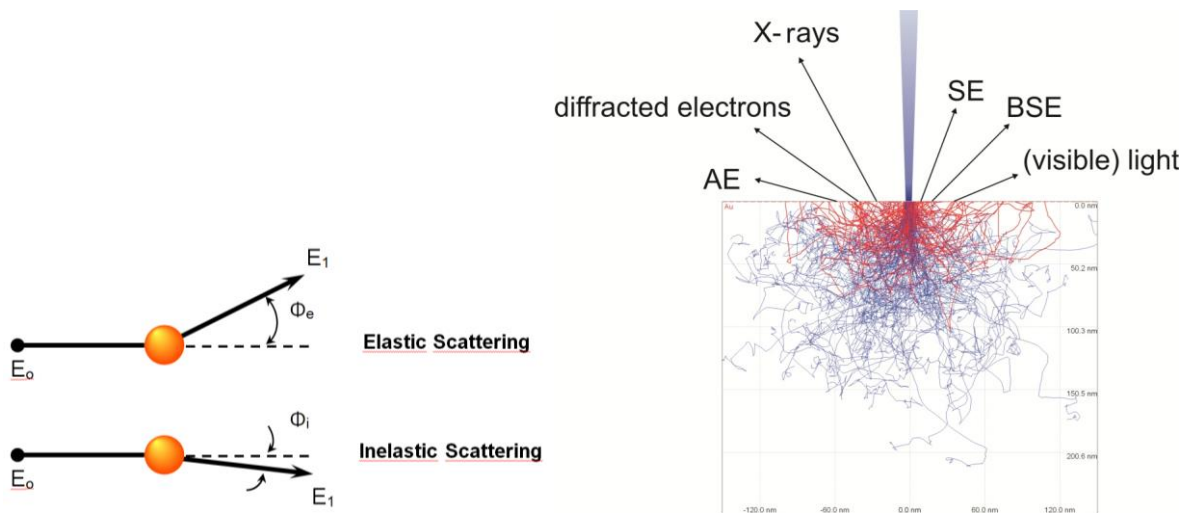
Figure 9: left: schematic of elastic and inelastic scattering processes resulting in different scattering angles [5]; right: Monte Carlo simulation of the interaction region in the specimen with elastic and inelastic events indicated by the red and blue trajectories, respectively [6].

Finally, characteristic X-ray can be excited by inner shell ionization due to the incident electron. The recombination of the generated free electron position by an electron from a higher energy shell results in the emission of characteristic X-rays. Analysis of this characteristic emission allows a material identification via energy dispersive X-ray spectroscopy (EDXS) [5]. The combination of individual X-ray detection with the scanning electron beam allows then the generation of so called elemental maps, revealing the material composition with a laterally resolved character [5].
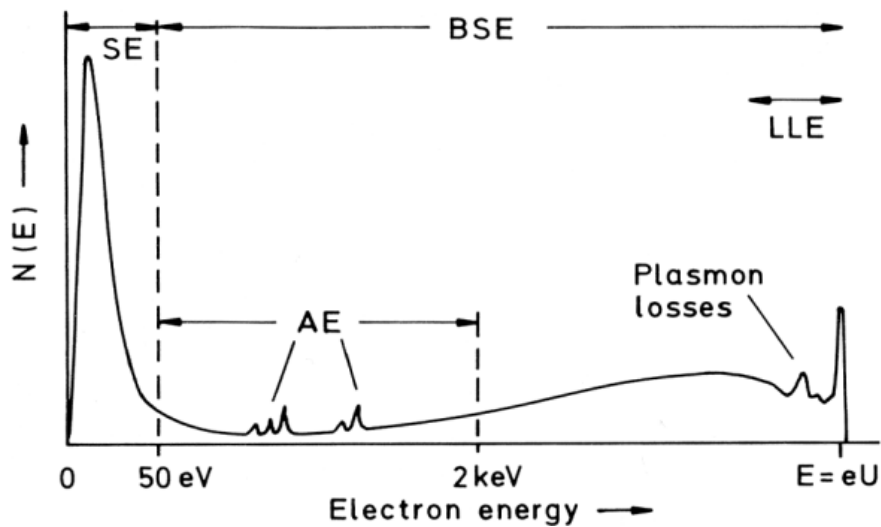
Figure 10: energy distribution of surface emitted electrons primarily irradiated with electron energies E (=e.U) [25] (SE … secondary electrons, BSE … backscattered electrons, AE … Auger electrons, LLE … low loss electrons, U … acceleration energy).

Due to the low SE energies and the related short "blurring" of actual generation sites makes the use of SEs as high resolution electron species highly beneficial. The most commonly used detector for SEM imaging is the Everhart-Thornley detector (**ETD**). Electrons are attracted by the detector due to a positively or negatively charged potential by a pre-mounted cage and hits subsequently the

scintillator behind [5]. This interaction produces photons which are multiplied by a subsequently mounted photomultiplier and guided to a photo device (photocathode, CCD-chip) transforming the photon flux into an electron current which can be handled by the hardware. The tilted angle in which typical ETDs are mounted together with the low energy of SE causes a "shadowing effect" where areas facing the detector are brighter (more electrons) than averted areas, resulting in a 3D like image of the surface. Applying a negative bias on the ETD cage (see above) can be used to exclude SE (see Figure 10) which restricts the signal to BSE. This signal carries material information due to material dependent BSE yields. This gives a qualitative material distribution, however, with lower signals compared to SE. If shadowing effects are unwanted another type of detector, the so called through the lens detector (**TLD**) can be used which is installed within the last part of the electron column, hence, giving a perpendicular detection view of the sample. They can be used for the detection of SE and enable imaging of the specimen in high resolution, but have the drawback of a low efficiency due to their limited collection angle compared to the ETD [5]. At the end, the individual imaging purpose decides about the detector choice.

2.1.5   Image Formation and Magnification

The SEM images are obtained by systematic rastering the specimen area of interest with the electron beam. The motion of the electron beam is typically not continuous but step-like which is defined by two quantities: 1) the point pitch (**PoP**) which is the distance of two adjacent raster points, and 2) the dwell time (**DT**) which indicates the individual irradiation duration. During the DT, the detector intensity is recorded accordingly together with its coordinates, giving a laterally resolved intensity image of the investigated area [5].

The magnification of the scanned area can be increased by decreasing the PoP variation of the raster, while leaving the number of points of the raster constant. Hence, the maximum magnification of the investigated area is limited by the diameter of the electron beam.

The signal to noise ratio of the image can be varied by changing the DTs. However, increasing DTs for gaining higher intensities of each point can cause damages in case of materials, like polymers, which react sensitive to the significantly higher electron doses [5]. This parameter adaption also leads to a sample drift caused by local charging of the material worsening the achievable lateral resolution. Another approach often used at modern SEM is to keep DTs small and subsequently treating the gained intensity mathematically to increase the brightness of the image. The optimal setting of the signal to noise ratio has to be found by the operator using a DT adapted to the material abilities of sustaining damages caused by electron irradiation.

The resolution of the image is also limited by the lens errors, such as spherical aberration, chromatic aberration, aperture diffraction and the ability of the lenses to focus the electron beam in a diameter as small as possible (a particular problem for low energy electrons due to mutual repulsion [5]). Another lens error affecting the resolution is axial astigmatism, which can easily be corrected by the operator and which will be discussed in the following chapter.

2.1.6   Axial Astigmatism

Due to fabrication related tolerances electron lenses work not ideal. Deviations from the rotational symmetry lead to a non-perfect focussing behaviour of the electron lens and the path of the electron beam is distorted depending on the position it runs through the electromagnetic lens. This effect is called axial astigmatism and limits the resolution of the image.

Figure 11 shows the effect of the axial astigmatism on a cross shaped object with equally long structures. Depending on the position of the electron beam passing the lens the lengths of the bars are elongated or shrunk, leading to a distorted image [5]. The correction of this aberration is done by a special lens system, which is composed of at least four poles. Nowadays, this type of system is built in every SEM or FIB to enable imaging at the highest possible resolution.

In case of electron beam induced deposition axial astigmatism leads to structure shapes which are different from the intended one. For example a deposit in the desired shape of a rectangular would result in a deposited structure shaped in form of a rhomboid. As the properties of the deposits depend on their dimension a comparison of the obtained results is impossible. Therefore, the correction of the axial astigmatism is *essential* and has to be done prior to the beginning of each deposition process (see also section 2.1.10).
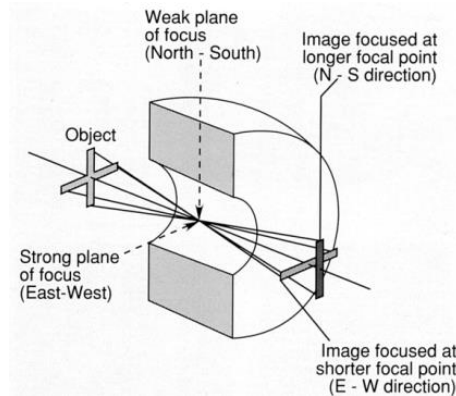
Figure 11: schematic diagram of image distortions related to axial astigmatism [5].

2.1.7   Focused Ion Beam (FIB) Microscope

Focused ion beam (FIB) microscopes work with the same principle as SEMs described above. The difference between a SEM and a FIB microscope is the nature of the particle beam rastering the specimen surface. While SEMs work with electrons the particles used by a FIB microscope are charged atoms: ions. FIB microscopes are not intended for imaging as the high mass of the ions destroy the initial topography of the surface through local material removal called sputtering. Additionally, the used ions are implanted within the specimen materials structure, thus changing their properties. One original application of ion beams was the semiconductor modification based on resist masks. During the years, this application has been expanded by the scanning aspect. Another type of application was the defined material sputtering which has also been expanded by a moving beam for a defined control. Nowadays, FIB microscopes has an excellent reputation as site specific preparation tool for ultrathin TEM lamellas as mentioned at the very beginning of this chapter. The fabrication of functional (nano)deposits is also possible with a FIB microscope, but is often limited due to heat effects, implantation aspects, co-sputtering and the beam size together with its related

collateral effects discussed in section 2.1.9. Therefore, FIB based fabrication of functional (nano)structures has not been used for this thesis. In our case the FIB application was restricted to electrode related cutting procedures between individual experiments as discussed in section 3.1. Nevertheless, a brief FIB introduction is given in the following since it is an essential part of the modern DBMs.

2.1.8   Ion Source and Lenses

The ion source, also called ion gun, consists of a small reservoir, filled with a liquid metal. Due to the high melting point of most metals the variety of appropriate materials is quite limited. Another requirement for the choice of a sufficient material is a low vapour pressure as the ion gun is operated under high vacuum conditions. Nowadays common ions sources use liquid gallium (melting point: 29.8°C) wetting a small tungsten hair pin. The hair pin is vertically aligned so the liquid metal creeps down and forms a small droplet at the very bottom of the hairpin (Figure 12). According to their functionalities such sources are called liquid ion metal source (**LIMS**) [7,8].
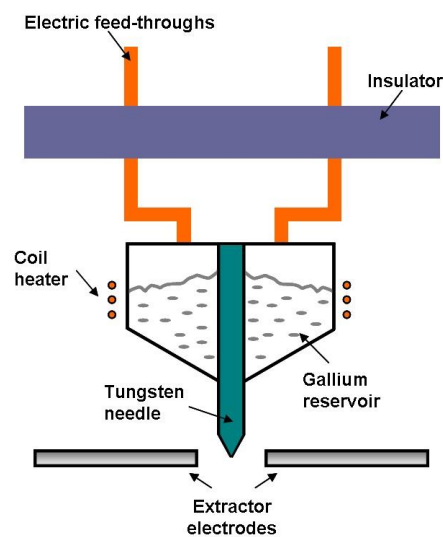
Figure 12: schematic diagram of a liquid metal ion source (LIMS) [9].

The shape of the droplet is changed into a cone by applying a high electric field with the extractor electrodes (see Figure 12). The concavely shaped cone, also called Taylor cone, reduces the applied electric field needed to extract single Ga^+ ions from the liquid layer and accelerates them towards the specimen [7,8]. Subsequently, the ion beam is directed through the beam acceptance aperture and passes through the condenser lens system. This lens system configures beam energy in the range from 5 keV to 30 keV. The beam defining aperture enables the variation of the beam current from 1 – 20000 pA. A very important feature in the ion beam column is the beam blanker which redirects the ion beam into a faraday cup, thus preventing unintentional destruction of areas on the specimen. The octopole coils corrects astigmatism effects of the ion beam and raster the ion beam accordingly. The final objective lens focusses the beam on the specimen identically as in a SEM.
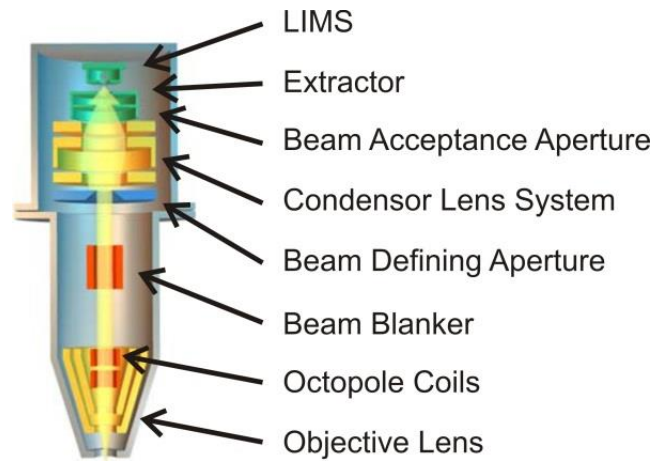
Figure 13: schematic cross section of a focused ion beam [1].

Ion beams are focussed by electrostatic lenses instead of electromagnetic lenses, which are used at a SEM, as a result of the faster response [7,8]. Such lenses are subdivided into different consecutive electrode systems each having a different voltage instead of windings used for electromagnetic lenses. In addition to the usual lens errors affecting the shape and the diameter of the ion beam the size of the beam is widened due to the Coulomb interaction between Ga^+ ions [7,8].

2.1.9 Ion Matter Interaction

Due to the higher mass compared to electrons and the larger size of the utilized ions the specimen material is much more affected by the impinging ion beam than for an electron beam. The ion beam transfers its (significant) momentum to the structure of the specimen, which leads to the removal of specimen atoms, ions or large particle clusters at the direct impact area. This process is called sputtering and utilized for localized and controllable ion milling process (e.g. sub-surface investigations or TEM lamella fabrication). However, ions located in deeper regions cannot leave specimen again in a straightforward manner and are therefore implanted permanently. This can also generate lattice vacancies and distort the initial lattice structure of the specimen. The total loss of crystallinity is then called amorphization, while molecules investigated by the ion beam are chemically degraded. The displacement of the lattice ions in the specimen triggers subsequent cascade collision effects inside the material, including valence electron emission, re-emissions of atoms, ions and particle clusters plus the creation of further lattice vibrations leading to an additional temperature of areas distant from the ion beam as graphical summarized in Figure 14 [7,8].

Finally, the incident ion beam heats the material to very high temperatures especially at areas close to the beam centre. Simulations reveal temperatures of more than 2000°C. However, the lateral distribution of the temperature depends on the thermal conductivity and the specific heat capacity of the specimen. In case of sensitive materials such as polymers or biomaterials, this effect can strongly limit the applicability. Nevertheless, big efforts at the FELMI revealed crucial improvements of FIB processing for such sensitive materials by the introduction of an alternative patterning strategy which massively reduces local thermal stress [10,11].

The ion – material interactions creates also a vast amount of SE as a result of the high momentum and thermal energies during these processes. The signals can be detected by the ETD or the TLD which makes simultaneous imaging possible.
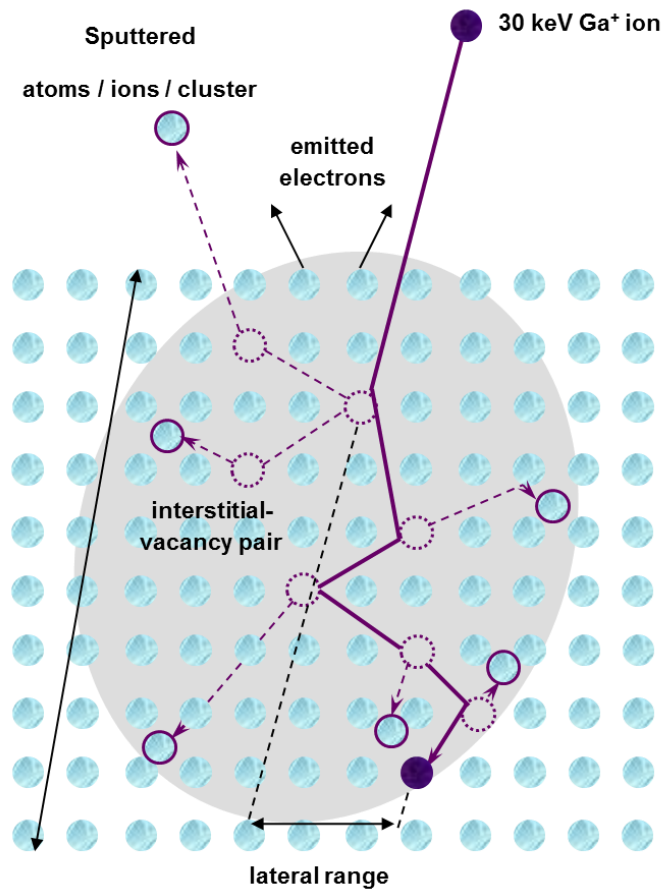
Figure 14: interaction effects between a focused ion beam and the specimen [4].

All in all we can conclude that the focused ion beam is perfectly suited to remove material locally and very defined. However, material implantation, chemical degradation and amorphization in the close proximity of the ion beam are unavoidable while elevated temperatures can be reduced to a minimum by the use of alternative patterning strategies. Therefore, if carried out carefully and aware of the drawbacks, FIB processing is an extremely powerful tool for surface modification in many different ways.

2.1.10 Focused Electron Beam Induced Deposition (FEBID)

Focused electron beam induced deposition (**FEBID**) is a very versatile direct write method which enables the deposition of functional 3D structures with spatial nanometre resolution [12]. The structures can even be deposited on a non-flat substrate, which is a crucial advantage to other methods like electron beam lithography [13]. Beside basic morphological structures, FEBID can be used to fabricate passive applications such as photonic structures [12]. Recent publications have shown that deposits produced with the FEBID process can also work as active devices, like nano Hall-sensors or as stress-strain sensors, which can be used as alternative detection system for the deflections of the AFM cantilever [14].
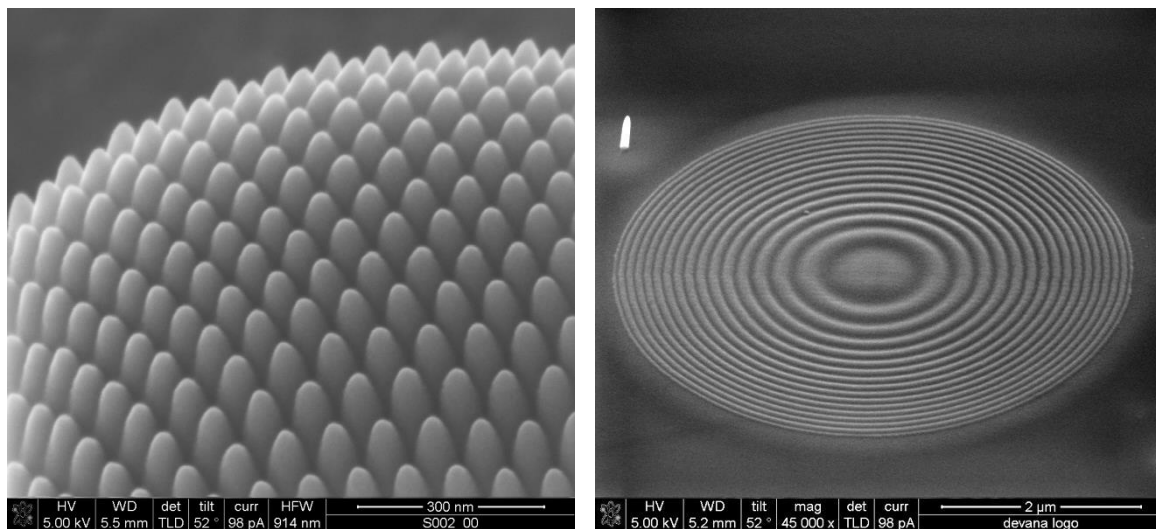
Figure 15: left: FEBID based 3D nanostructures on a non-flat surface; right: quasi-planar Gabor lens (right) [3].

The FEBID process can be described as an interaction process of electrons with precursor gas molecules adsorbed on the surface of a substrate resulting in a structure composed of nano-granules embedded in an amorphous matrix [12]. The interaction process leads to the dissociation of the gas molecules, cracking the precursor into volatiles parts, which are removed via the vacuum system and non-volatiles parts contributing to the growth of the desired structure. Therefore, to establish a constant growth of the structure, the precursor molecules have to be steadily replenished by a gas supply-system and the parameters must be chosen in such a way that local depletion is kept low [15,16,17,18]. The type of utilized precursor molecules defines the property of the deposited structures, which can be conducting, semi-conducting, insulating or magnetic [19].

2.1.10.1   Basic Principle

The most important components needed for the FEBID process is the electron beam, generated in an electron column similar to those used in an SEM, and the gas injection system, which supplies the gaseous precursor molecules (Figure 16).

The movement of the electron beam during the deposition process resembles to the scanning procedure of an SEM. The electron beam moves from one point to the next one, typically in a raster strategy, which has the shape of the desired pattern. The electron beam stops at each point for a specific time, which is again called the dwell time t_d. In analogy to the SEM, the distance between two adjacent points is called the point pitch (PoP). The achievable spatial resolution of the structure is influenced by the diameter and profile of the primary electron beam on the substrate surface. Furthermore, the spatial resolution is also affected by proximity effects, which broadens the size of the gained structure and has been investigated in detail at the FELMI [16,20].

The precursor needed for the deposition process is usually stored in a crucible which is part of a gas injection system (**GIS**). Preliminary to any deposition experiment the precursor is heated above its melting point to provide a stable gas phase. After reaching the desired temperature gaseous precursor molecules can be delivered to the vacuum chamber through a metallic needle at the end of the GIS with a diameter of 0.5 mm in our case. The end of the GIS needle is positioned close to the incident electron beam (X and Y) and placed between 150 µm and 200 µm above the sample surface.

The requirements the precursor molecules have to fulfil are quite contradictory. From a thermodynamic point of view, the vapour pressure of the precursor molecules has to be high enough to supply a sufficient amount of gaseous precursor molecules during the deposition process. In contrast the vacuum in the chamber has to be low, so water and hydrocarbons, adsorbed on the surface of the sample can be removed by the chamber vacuum, avoiding unwanted contamination of the final deposits. The precursor molecules injected into the vacuum chamber have to adhere on the surface of the sample for an adequate period of time (residence time), while this behaviour is not desired for the volatile parts of the molecules obtained after the dissociation process [12]. From an electronic point of view, the precursor molecule should be dissociated in one single electron event for electron energies ranging from very low to even mid-range energies (~ 10 eV $\rightarrow$ 5 keV) which is also not given for most of the precursors. As can be seen, the requirements for a proper FEBID process are manifold and depend strongly on the thermodynamic and electronic properties of the precursor molecules.
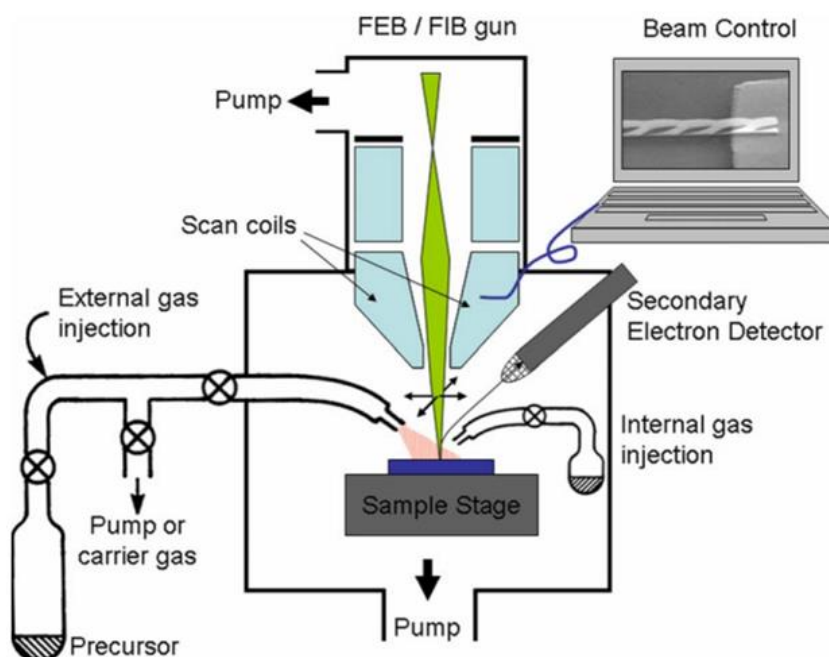
Figure 16: schematic diagram of an FEBID system with the main components and their alignment [12].

As mentioned at the beginning of this section there are a vast number of different precursor molecules, covering the wide range of applications suitable for the FEBID process. In general the structure of the precursor molecule consists of a central functional atom or ion surrounded by ligands. Volatility of the precursor molecules is established through the absence of a dipole moment and a high polarizability [12]. Both properties are working contrary to the requested sticking ability of the molecules on the surface of the sample. The classes of the utilized precursor molecules include alkanes, silanes, metal halogens, carbonyls, phosphines and acetyl acetones depending only on the functionality of the yielded depositions. An extensive survey of the typically used precursor molecules and their properties is given in [12] and [19].

An important factor for the growth rate is the number of adsorbed molecules $\boldsymbol{n(r)}$, which changes during the deposition process as a result of the changing morphology [15,17]. The behaviour of the precursor molecules covering the surface of the substrate can be described as a Langmuir adsorption, with the additional assumption that only weak interactions between precursor molecules and substrate appear. Furthermore, it is assumed that the coverage of the precursor molecules on the surface plane is limited to a monolayer. The molecule adsorption rate is basically governed by four different processes (Figure 17, Equation 2):

1. **Adsorption** of the molecules depend on the flux of the precursor molecules $\boldsymbol{J}$ and the sticking probability $\boldsymbol{s}$ on the surface of the surface introduced by the GIS
2. **Desorption** processes can be induced by thermic processes or physically through collisions of the precursor molecules with the incident electron beam, both processes depending on a specific resident time $\boldsymbol{\tau}$ respectively
3. **Diffusion** of the precursor molecules along the surface of the substrate
4. **Dissociation** generating the desired structure

$$\frac{\partial n(r,t)}{\partial t} = \underbrace{sJ\left(1 - \frac{n(r,t)}{n_{ML}}\right)}_{\text{adsorption}} - \underbrace{\frac{n(r,t)}{\tau}}_{\text{desorption}} + \underbrace{D\left(\frac{\partial^2 n}{\partial^2 r} + \frac{1}{r}\frac{\partial n}{\partial r}\right)}_{\text{diffusion}} - \underbrace{\sigma f(r)n(r,t)}_{\text{dissociation}}$$

Equation 2

The interaction processes of the electrons and the precursor molecule are summarized in Table 1. In general the energy relevant for the dissociation process covers a range from 1 meV, according to the energy of very slow SEs, up to the keV energy range for primary electrons. The complexity of the dissociation process is further increased due to the coupling of the precursor molecule with the substrate, which provides additional electronic and vibrational excitation channels. Therefore, only a few data sets for some selected precursor molecules describing the cross section of the interaction process between electron and precursor molecule are available [12].
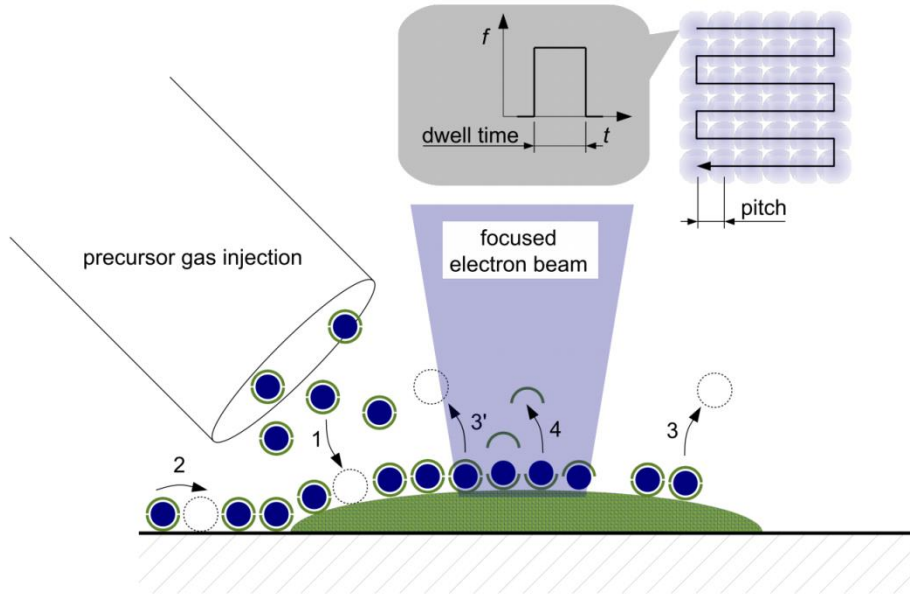
Figure 17: schematic of the different interaction processes during deposition, including adsorption (1), diffusion (2), thermic desorption (3), physical desorption (3') induced by collision processes and dissociation (4) [14].

The growth rate *R(r)* of the FEBID structures depends on the density of adsorbed molecules *n(r)* and the density of incident electrons. It can be described under the assumption of rotational symmetry as

$$R(r) = Vn(r) \int_0^{E_0} \sigma(E)f(r,E)dE$$

Equation 3

with *V* as the volume of the decomposed precursor molecule, *n(r)* as the number of adsorbed molecules, *E₀* as the energy of the incident electron beam, *σ(E)* as the energy dependent electron impact dissociation cross section and *f(r,E)* as a convolution of the primary beam and the emitted secondary and backscattered electrons with respect to their energy spectrum. As it can be seen, precursor dynamics, morphology and a varying electron yield on the surface influence the final growth rate which is then very complicated to be kept constant. Nevertheless, if sticking on some simple rules it is possible to maintain a constant and very high growth rate as described in [16] which is also part of an on-going master thesis at the FELMI (by Robert Winkler, 2013).

Table 1: interaction processes of electrons with precursor molecules during FEBID processes; E_i is the initial kinetic energy of the electron, while E_r stands for the residual kinetic energy of the electron after the interaction process [14].

	process type
$e^-(E_i) + AB \rightarrow AB + e^-(E_i)$	elastic scattering
$e^-(E_i) + AB \rightarrow AB(v) + e^-(E_r)$	vibrational excitation (VE)
$e^-(E_i) + AB \rightarrow AB^* + e^-(E_r)$	electronic excitation (EE)
$e^- + AB \rightarrow A^\bullet + B^-$	dissociative electron attachment (DEA)
$e^- + AB \rightarrow A^\bullet + B^\bullet + e^-$	neutral dissociation (ND)
$e^- + AB \rightarrow A^\bullet + B^+ + 2e^-$	dissociative ionization (DI)
$e^- + AB \rightarrow A^- + B^+ + e^-$	bipolar dissociation / ion pair formation (BD)

2.1.10.2   Materials

The structural composition of the FEBID deposits can be subdivided into three categories: **1)** amorphous; **2)** nanogranular or nanocomposite; and **3)** polycrystalline in case of pure deposits (Figure 18) [12]. Single crystalline deposits have also been demonstrated but are so complicated to fabricate that it can be packed into an own class so far. The properties, like electron transport or mechanical strength, depend on the structure of the gained material. The composition of the FEBID structures is commonly measured by EDXS, while in case of organic precursors Fourier infrared spectroscopy, Raman spectroscopy, Rutherford scattering or scanning TEM electron energy loss spectroscopy (STEM EELS) is applied. The structure can be changed by post-growth treatments like heating the sample which leads to a growth of the nanosized particles [19]. Another approach is the additional exposure to the electron beam, also resulting in slightly larger nanograins [17,21]. However, during this treatment procedure a small fraction of carbon can be removed from a thin surface region which changes then the relative composition anisotropically [17].
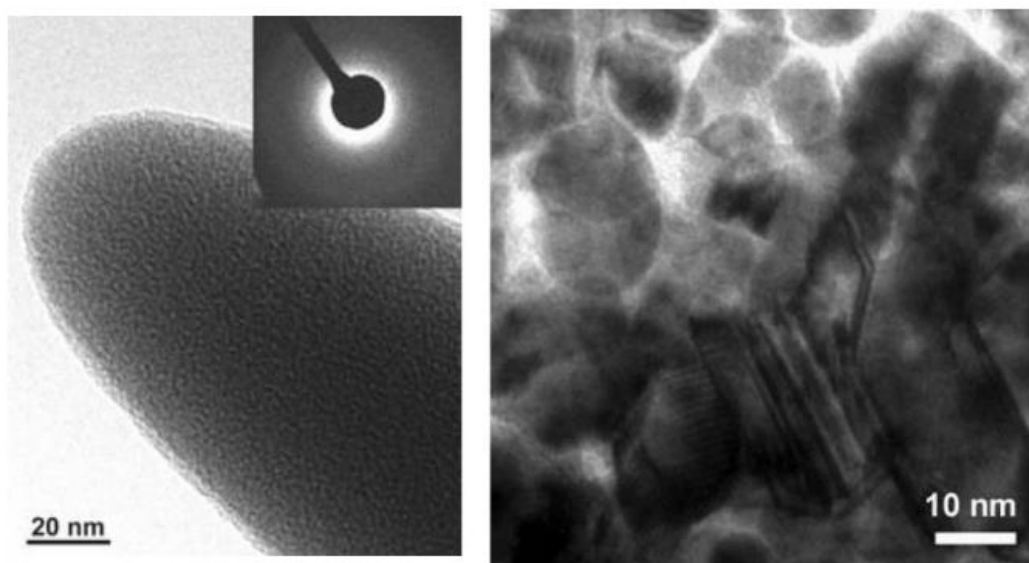
Figure 18: TEM image of FEBID deposits with different structures; left: amorphous Si-O-C structure (precursor: TEOS), right: polycrystalline structure of pure gold (precursor: AuClPF$_3$) [12].

The utilized precursor during the course of this thesis is MePtCpMe$_3$, resulting into a nanogranular structure (Figure 19). The structure consists of Pt-granules with a size between 2 - 3 nm, which are embedded in an insulating hydrocarbon structure [15,16,17]. No post-treatment procedures have been done, so every measurement concerning the characterization of the resistivity and the sensing abilities was done at structures in the so called as-prepared state. EDXS measurements revealed that the metal content of the fabricated deposits is in between 10 -15 at.%, while the carbon content was found to be in the range of 85 – 90 at.% [16]. From literature it is known that this precursor is not dissociating entirely in a single electron event but requires several interaction events before it is dissociated completely [22]. Particular problem is the cyclopentadiene group which is complicated to be dissociated fast enough.
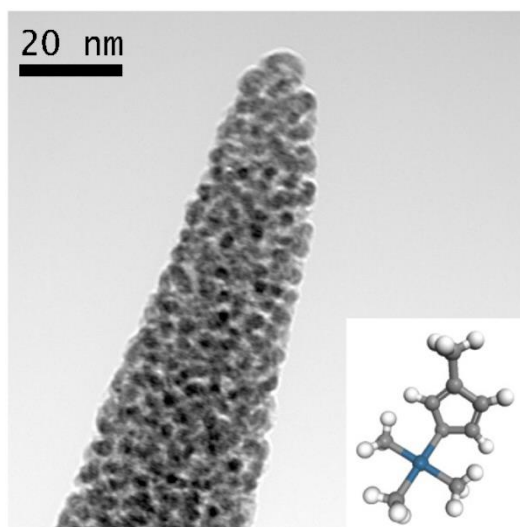
Figure 19: TEM bright field image of the nanogranular PtC deposit where the black areas indicate the metallic Pt granules. The inlet shows the chemical structure of the utilized MePtCpMe₃ precursor molecule [3].

2.1.10.3 Working Regimes

The working regimes during the fabrication of FEBID structures can be distinguished into two regimes, namely mass transport limited (**MTL**) and reaction rate limited (**RRL**) precursor regimes. The MTL regime is characterized by a lack of precursor molecules compared to the potentially dissociating electron species. This electron excess provides very high dissociation degrees for the MTL regime but also a higher number of incorporated carbon as a result of electron induced polymerization of precursor fragments and / or chamber residue. MTL conditions are basically found for high DTs (strong depletion), small PoPs (proximity depletion), short refresh times (complicated replenishment), low gas fluxes, morphologically challenging situations (e.g. nanopillar provide only a very narrow pathway) or high electron beam currents [16]. On the other hand, RRL conditions are defined by a lack of potentially dissociating electron species or very high coverages of the precursor molecules on the surface. In this case, the dissociation process is not finished for most molecules which are then incorporated into the deposit. Post-growth e-beam curing can then finish the process without incorporating unwanted carbon fragments. By that, the overall composition is widely kept constant while the functionality is increased due to slightly growing Pt grains which simplify the grain-to-grain tunnelling [17]. RRL conditions are achieved for very short DTs, large PoPs, long refresh times, high gas fluxes, simple morphologies and low electron currents which altogether keep the total precursor coverage very high [16]. The growth rates of structures fabricated in the RRL regime are found to be higher compared to structures produced in the MTL regime. The fabrication of the FEBID structures during this thesis was done in both regimes, MTL and RRL. The influence of the process regimes is discussed for the height growth and the resistivity in chapter 3.2 and chapter 3.3.3 respectively. Please note, MTL conditions are much easier to establish while real RRL conditions can be complicated to be recognized. Hence, as will be shown in the results section, MTL conditions have finally been chosen for the sensors developed in this master thesis.

2.1.10.4   Charge Transport in Nanogranular Materials

FEBID structures fall into the class of disordered electronic materials. Nanogranular materials consist of nanocrystallites embedded in a dielectric matrix, so their type of structure lies in between the cases of fully amorphous deposits and polycrystalline structures [14].

The tunnelling conductance **G** is defined through a finite tunnelling probability of the electrons between the nanosized grains. Normalization of the tunnelling conductance with the conductance quantum leads to the coupling strength

$$g = \frac{G}{\left(\frac{2e^2}{h}\right)}$$ **Equation 4**

with **e** as the elementary charge and **h** as the Planck constant. If **g** is larger than the critical coupling strength **g_c**, the nanostructures are then considered to be metallic, meaning they have a finite conductance for temperatures close at 0 °K. In the opposite case, the nanogranular structures are insulating, having no conductance when approaching very low temperatures [14].

Inside individual grains the electron transport is considered to be diffusive because of intragrain- and surface-scattering. The intragrain energy scale is defined by the mean spacing **δ**, which describes the difference of the one-electron levels close at the chemical potential. Mathematically the mean spacing is defined as

$$\delta = \frac{1}{(N_F V)}$$ **Equation 5**

with **N_F** as the number of electron states close to the Fermi level and **V** as the volume of the nanograin. Hence, the mean energy depends on the size of the nanogranule, and is large for small particles [14]. Additionally, the energy levels close to the chemical potential are broadened because of the tunnel-coupling occurring between the nanograins. This effect is described by the broadening parameter Γ.

$$\Gamma = g\delta$$ **Equation 6**

Figure 20 shows the phase diagram for the different transport regimes which are encountered for nanogranular structure.

Finally the Coulomb charging energy **E_c** has also to be considered. This is the energy needed to add an electron on a non-charged particle [14]. It depends on the capacitance of the nanograin, which itself depends on the size of the nanogranules. At very low temperatures the Coulomb energy suppresses the electron transport, which is the reason why the structures become insulating. In case of very small nanograins the intragrain mean spacing **δ** can exceed the Coulomb charging energy, but this is not the case for FEBID structures as the diameter **D** of the nanogranules is in the nanometre scale.

The intergranular electronic coupling, which governs the conductance of the nanogranular structures, is subdivided into two different regimes by the product of tunnelling strength times the number of next neighbours for a nanogranule. If this product is < 1, which is the case for nanostructures with a very high tunnel coupling or with a very low metal content, the conductance can be best described by concept of the **weak-coupling regime**. The opposite case is called the **strong-coupling regime**. The electric conductance of nanogranular structure is a very complex topic and the description of both coupling regimes would go far beyond the scope of this thesis. In our case the conductance is established in the weak coupling regime. Therefore, the strong-coupling regime will not be explained in further details. The reader is referred to [23], which gives a detailed survey of all the concepts used to describe the conductance of nanogranular structures.
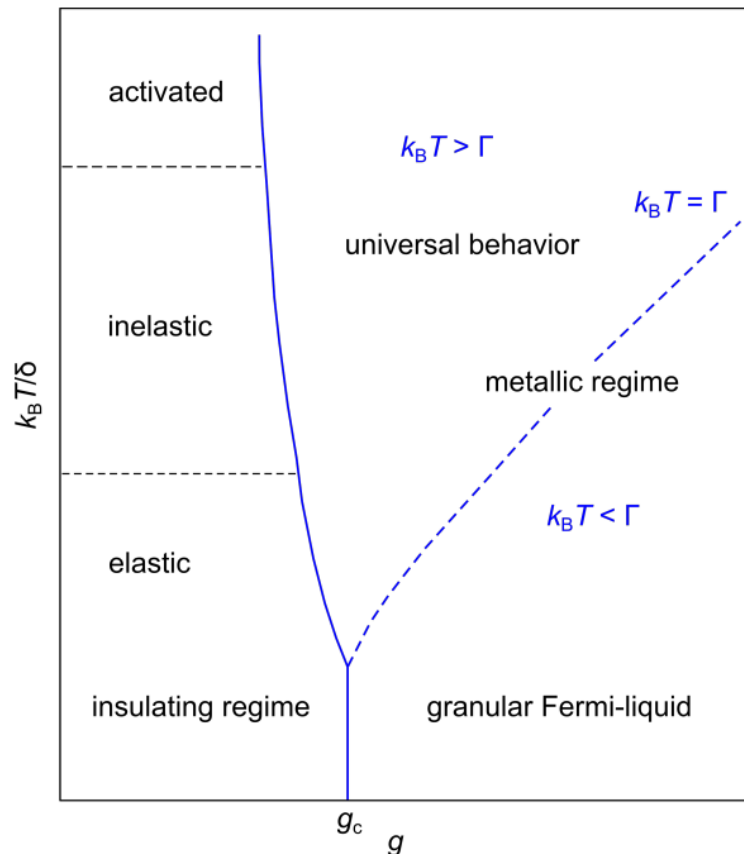
Figure 20: phase diagram for the classification of different transport regimes with respect to the tunnelling strength *g* and the ratio of the thermic energy k_B.*T* to the mean spacing [14].

The weak coupling regime is further divided into two different regimes, which depend on the temperature. For low and medium temperatures the behaviour of the conductance is well described by the correlated variable range hopping (**c-VRH**) regime, while at lower temperatures the behaviour of the conductance resembles to the Arrhenius regime. However, as the U / I characterizations and the investigations of the sensing capabilities are carried out at room temperature the conductance behaviour of the FEBID structures can be considered to be in the c-VRH regime [14,23].

The temperature dependent conductivity in the c-VRH regime goes as

$$\sigma\,(T) = \ \sigma_0 \exp\left[-\left(\frac{T_0(\kappa)}{T}\right)^{1/2}\right] \qquad \text{Equation 7}$$

with the material parameter T_0. The size of this parameter is governed by the dielectric constant κ of the nanogranular structure and the attenuation length ξ of the wave function, which is the quantum-mechanically concept to describe the behaviour of the electron. The dielectric constant of the structure is calculated by the Maxwell-Garnett approximation [14,23]. The material parameter is mathematically described by the following equation

$$T_0 \approx \frac{e^2}{4\pi\varepsilon_0\kappa\xi(T)k_B} \qquad \text{Equation 8}$$

The attenuation length is subdivided with respect to the temperature into two co-tunnelling channels. The attenuation length ξ_{el} of the elastic co-tunnelling channel shows no temperature dependency and is given by

$$\xi_{el} = \frac{2D}{\ln(\bar{\bar{E}}\pi/_{c_{el}g\delta})} \qquad \text{Equation 9}$$

with $\bar{E}$ as the geometrical average of the electron and hole excitation energy and the boundary condition c_{el} which can be set as 1 if the Coulomb interactions are restricted to short distances. In case of inelastic co-tunnelling the attenuation length reads as

$$\xi_{in}(T) = \frac{2}{\ln\left(\bar{E}^2\Big/16\pi c_{in}gk_B^2T^2\right)} \qquad \text{Equation 10}$$

With the boundary condition c_{in} that can be again chosen as 1, when only short ranges of the Coulomb interactions are considered. The attenuation lengths are used to describe the hopping distance r^*. This is the distance an electron can pass, when tunnelling from one grain side to the next one.

$$r^* = \sqrt{\frac{E_C}{k_BT}\xi D} = \sqrt{\frac{e^2\xi}{8\pi\kappa k_BT}} \qquad \text{Equation 11}$$

The hopping distance can be varied by the temperature and is decreased for higher temperatures. Furthermore, changing the dielectric constant leads also to a variation of the hopping distance (see chapter 3.5.4). Another approach to manipulate the conductivity is to change the distance between

the nanogranules mechanically. This is the working principle used at the FEBID stress strain sensor, introduced at the beginning of this chapter.

2.2   Atomic Force Microscopy (AFM)

In contrast to SEM investigations, atomic force microscopy (**AFM**) enables the quantitative 3D visualization of surface features down to the atomic scale [24]. AFM can also be used to manipulate the features of the surface. During this master thesis AFM was used to measure the actual dimensions of the fabricated deposits, mainly focussing on the gained structure heights.

2.2.1   Basic Principle

A cantilever with a small tip with an end radius of less than 10 nm on one end is systemically moved over the surface and gets deformed (bended and distorted) due to the interaction forces between the tip and the material of the specimen. The deflection of the cantilever is optically detected by a laser system and a position sensitive detector (**PSD**) which is then used as the input signal for further processing based on the cantilever distortion (Figure 21).
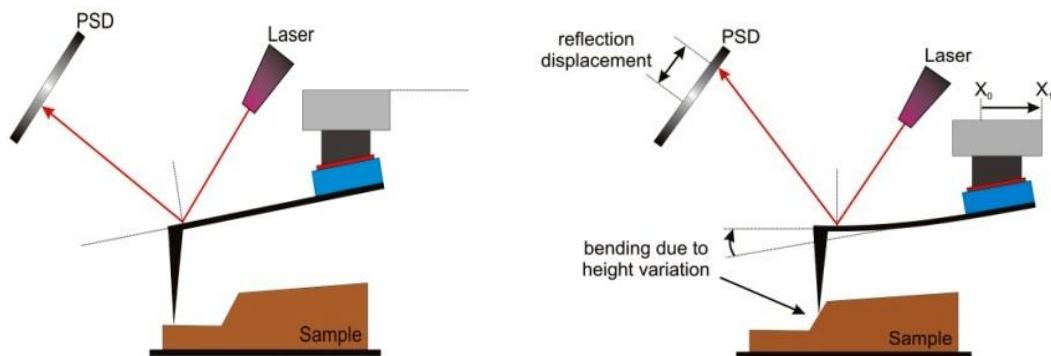
Figure 21: schematic of the detection principle used in an AFM. The interaction of material and cantilever cause a deformation of the cantilever from its initial (left) to its deflected (right) position [3].

The cantilever is moved in X and Y direction with the motion system, which is composed by 4 piezoelectric elements arranged in form of a tube (Figure 22). Applying a voltage on the piezoelectric elements causes a contraction or elongation, depending on the polarity of the voltage. The motion of the cantilever is achieved by applying opposite voltage polarities on the elements facing each other. Movements of the cantilever in Z direction is done by applying a voltage on the electrode seated above the piezoelectric elements (Figure 22).

AFM images can be obtained by using the contact or the tapping mode. In the contact mode the tip of the cantilever touches the surface of the specimen resulting in a cantilever distortion detected by the PSD. Based on this displacement, the Z piezo is varied accordingly to restore the original laser position which is then equal to same forces between tip and sample. By saving the Z value for every X/Y position generates the quantitative height image.
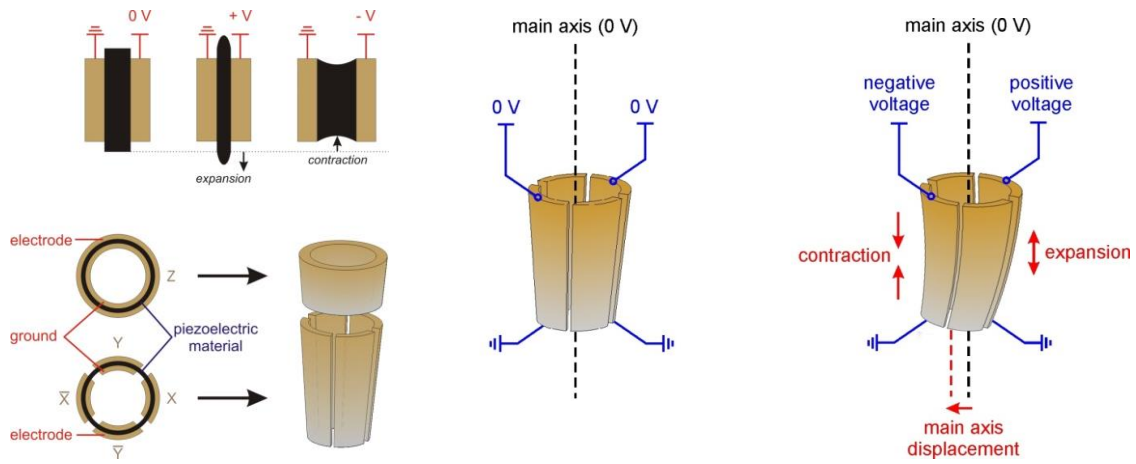
Figure 22: schematic diagram of the motion system with the 4 piezoelectric elements (left) and the operation method of the tube (middle & right) [3].

In contrast, the tapping mode excites the cantilever with an additional piezo into its mechanical resonance frequency ω_{freq} and only taps the surface of the specimen instead of permanent contact. If the cantilever approaches features on the surface it gets attracted or repulsed by the interaction forces between the tip and the sample. The occurring forces can be described as the derivative of the Lennard-Jones potential, mainly depending on the distance between tip and sample. The interaction forces cause a shift from the initial resonance frequency to the intrinsic tip-sample related frequency $\omega_{coupled}$ (see Figure 23 *a* and *b*). As a result, the amplitude is decreased which acts now as input signal for the electronics. The according movement in Z direction restores again the initial amplitude (and resonance frequency). The Z coordinate for every point in the scanned area is captured and used for the generation of the quantitative height image. To get a more realistic description of the interaction a dissipative energy term has to be added, further increasing the dampening of the amplitude. However, their explanation would go far beyond the scope of this thesis. Therefore the reader is referred to [24].
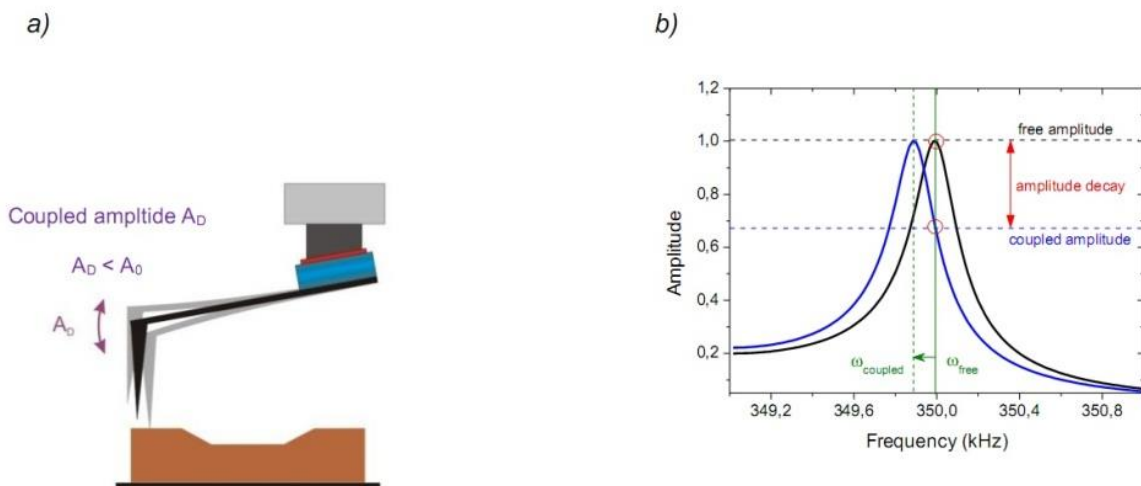
Figure 23: (a) basic principle of the tapping mode; (b) decay of the amplitude due to the frequency shift caused by interaction processes depending on the distance between tip and sample [24].

2.3 Sensor Related Acquisition Setup

The main issue of this thesis is the electric characterization of the fabricated PtC deposits and the investigations of resistivity changes due to different ambient conditions. Feasibility studies concerning the same issue have partly been done during an earlier thesis [25], including the first investigations regarding to the changes induced by exposure to ambient air conditions by venting the DBM chamber. In contrast to the mentioned previous study which has been performed at constant currents, the experimental setting in this master thesis uses of a constant voltage applied to the deposits while the electric current is measured. The advantage of this setting is the direct observation of a varying current representing the direct response upon variable tunnelling barriers upon different gas exposures. The resistivity ρ is calculated by applying Ohm's law and subsequently scaling the results by a factor considering the cross section A and the length l, which the current has to pass through the deposition. The cross section can be varied by the width and the height of the deposit while the length is fixed by the distance between the pre-patterned electrodes (see next section).

$$R = \frac{U}{I} \; ; \; R = \rho \, \frac{l}{A} \qquad\qquad \textbf{Equation 12}$$

$$\rho = \frac{A}{l} * \frac{U}{I} \qquad\qquad \textbf{Equation 13}$$

2.3.1 Substrate Layout

The substrate used during the investigations is a highly boron doped silicon wafer in the dimensions of 25 x 12 x 2 mm ($l\,x\,w\,x\,h$) with a 500 nm isolating SiO_2-layer on the upper side. The non-conducting SiO_2-layer prevents additional currents in between the electrodes and the grounded silicon wafer, respectively.

To connect the PtC-deposits with the measurement equipment, on each substrate there are four 2-point structures and one 4-point structure as schematically shown in Figure 24 (top). The electrode structures were designed and fabricated at the Karl-Franzens-University Graz together with Dr. Andreas Hohenau (Institute for Physics, Graz University, Austria). The structures were processed via mix-and-match approaches. This technique consists of an initial e-beam lithography step followed by subsequent physical vapour deposition of two metals. The material used for the electrodes was gold because of its high electrical conductance and its chemical stability. A thin Cr-layer (around 5 nm) between the SiO_2 substrate and the gold structures enhances the adhesion. This arrangement makes the structures more sustainable and therefor easier to handle. The final height of the structures is in the range of 40 - 60 nm (see Figure 24 at the bottom).

There are two different experimental approaches to contact the deposits for resistivity determination, which are the 2-point method and the 4-point method. While at the 2-point method, the applied voltage and the traced current are measured on the same circuit path, the 4-point method uses two different paths. Utilizing the 4-point method brings the advantage that the electric current passing through the deposition can be measured very accurate and contact resistances can be mathematically eliminated. However, for 4-point measurements a special design of the hardware

setting is needed where a constant current passes the deposit while the voltage is tracked. This is not ideal for our experimental setup because we want to observe the current variations directly instead recalculating ρ from voltage variations. For the 2-point method every resistance in the transmission line, like connector cables or the intern-resistance of the measurement devices, contribute to the finally measured current directly which is what we want to observe. Although this leads to a higher resistivity calculated for the investigated deposits, the contributions of the devices along the transmission line are considered to be very small compared and therefor can be neglected. To validate the reliability of 2-point measurements, a direct comparison between 4-point and 2-point measurements has been carried out in a previous study [25] which revealed identical qualitative behaviour, however, with slightly increased resistivities due to the contact resistances. Therefore, the use of 2-point measurements is reliable and used throughout this thesis unless otherwise stated.
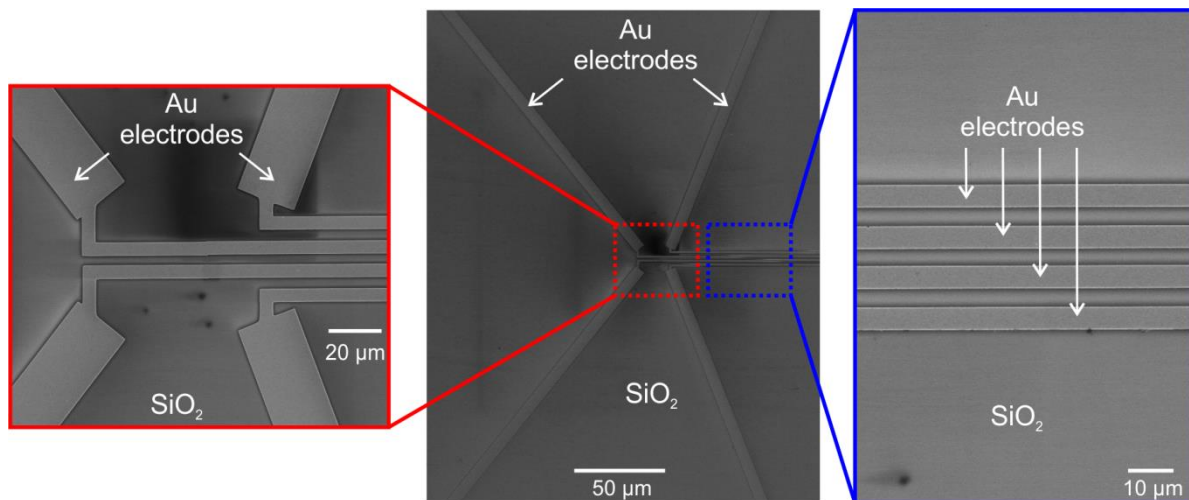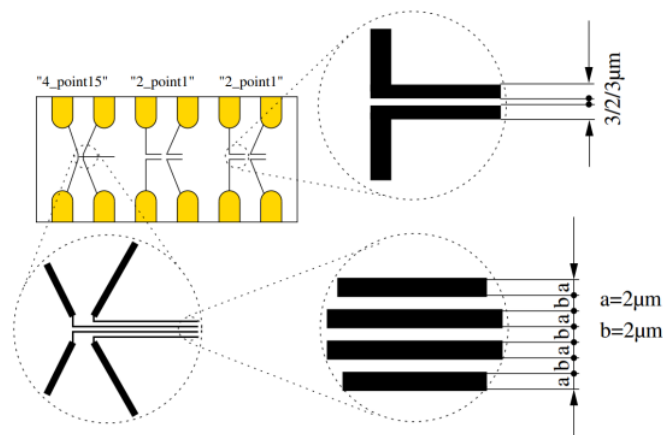
Figure 24: top: electrode layout of the used substrate; bottom: SEM overview of the central area of a 4-point structure (centre) with detail images at the left and right.

Hence, until not specified differently, all electrical measurements in this thesis are based on 2-point measurements.

2.3.2 Electrical Measurements – FELMI

2.3.2.1 Hardware

The specimen is mounted on the specimen holder, which was designed during an earlier master thesis [25]. Metallic clamps on the sample holder are fixing the specimen in its position and connects the macroscopic electrodes of the specimen via shielded leads with the measurement devices, seated outside the vacuum chamber of the DBM. To keep the vacuum level inside the chamber unaffected the leads inside and outside the chamber are connected by a RS232 interface.
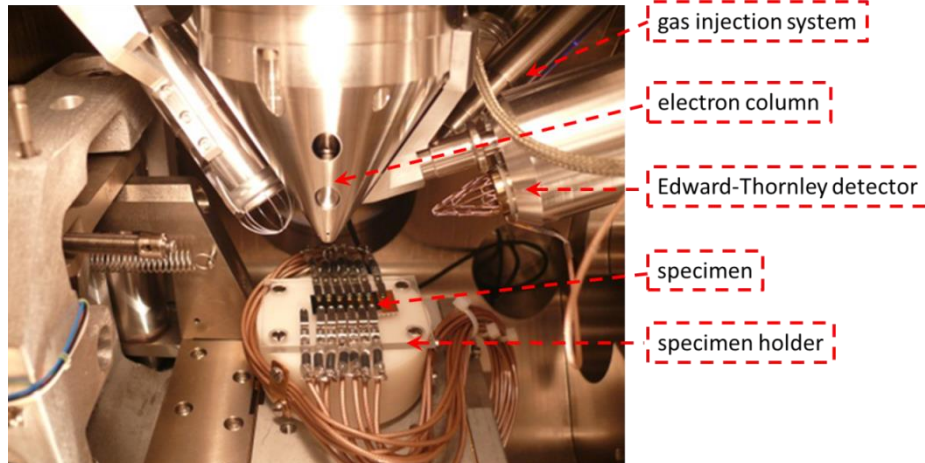
Figure 25: specimen holder with electrically connected specimen inside the vacuum chamber of the utilized DBM.

For the used hardware setup the applied voltage is provided by a Keithley 230 constant voltage source [26]. This device has an additional feature which enables the user to do voltage sweeps with a custom set of different voltages, each applied for a specific period of time. To ensure safe operation conditions for the PtC deposits and other measurement devices in the transmission line the voltage source has been programmed with 3 different current limits depending on the individual measurements (compliance limits of 2 mA, 20 mA and 100 mA).
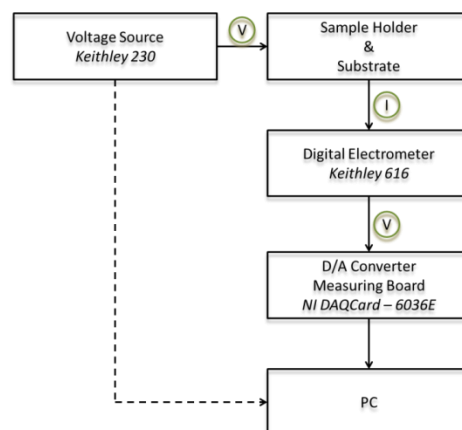
Figure 26: schematic of the measurement setup and the type of the transmitted signal (voltage V, current I).

The electric current is measured by a Keithley 616 [26]. The device transforms furthermore the measured current linearly into an equivalent voltage signal, which can be processed by the analogue – digital (A/D) converter. For this a DAQ 6036-E [27] measurement card with a PC interface was used

to allow electronic data acquisition, online and offline data treatment and storage which is described in detail in section 2.3.2.2. The schematic overview of the used hardware setting can be seen in Figure 26.

2.3.2.2   Software

As mentioned above basic software packages were programmed in a previous master thesis [25]. Since the basic setup is now different, it had to be adapted to the current situation. Prior to analysing the measured data the utilized software is divided in 3 different steps: **1)** acquisition, **2)** post-processing of the data and **3)** graphical presentation where further treatments like fitting can be / have been done. Graphic presentation were realized by appropriate software (ORIGIN [28]), the other two parts by using intern developed software programs via LabView [29]. These software programs provided a graphical user interface (**GUI**) which enabled the user of comfortable editing the filtering and smoothing parameters used during the post-processing steps and a data display to monitor the results of this editing. In the following the 3 parts are discussed in more detail to provide an understanding of the programming and the post-process necessities and procedures applied.

The required software for the acquisition task was developed with LABVIEW [29] because of an ideal hardware support and easy programming. A short survey of the sub-routines building up the recording software program is given in Figure 27.
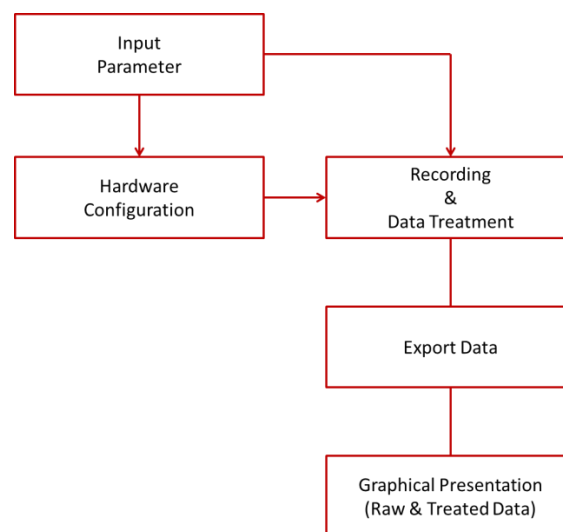
Figure 27: schematic of the sub-routines building up the recording program.

The GUI of the acquisition software is shown in Figure 28. On the right there are two data displays enabling the user to monitor both the raw and the online treated data in a period of one second (lower panel) and a period of time that can freely be chosen (upper display). While the upper display allows for the direct observation of overall trends, the lower panel shows details which can be very important for proper processing. Treatment of the data involved filtering of the input signal with a digital low pass filter (**LPF**) in the Butterworth design. The Butterworth filter coefficients needed for the filtering process are automatically generated by the built-in LABVIEW software package. Subsequently, the filtered signal is further smoothed with a median filter. At this filter type a single data point X and a specific number of neighbouring data points next to X is separated from the whole

data sequence obtained during one acquisition step. Subsequently the subroutine searches the median of the separated data sequence around the data point X and replaces the initial value of X with the median. This procedure is repeated for every data point of the whole data sequence. The required program subroutines were taken from the built-in program library of LABVIEW and therefore had not to be developed separately [29].
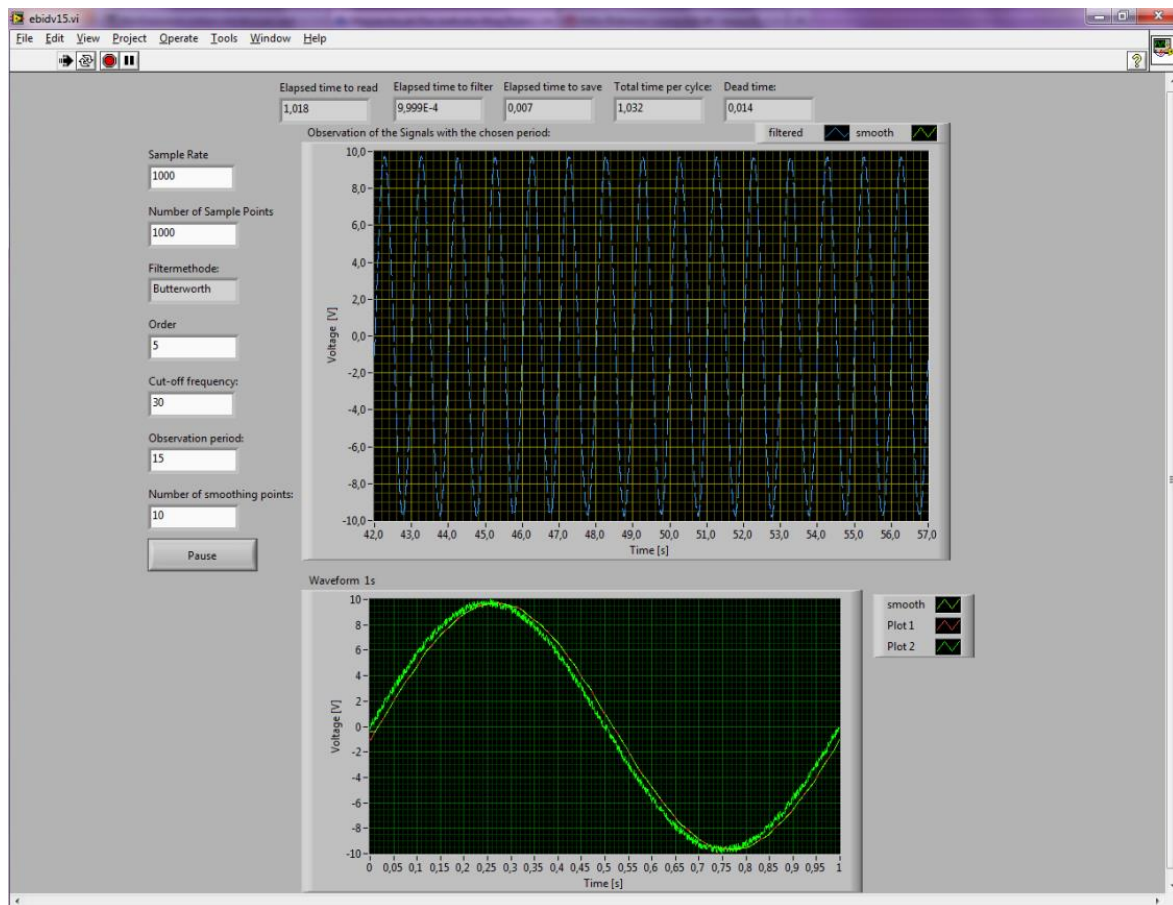
Figure 28: graphical user interface (GUI) of the recording program.

The text fields on the left of the GUI are used for editing the filtering parameters during an acquisition session. The presented default values were used during the whole measurement series.

- **Sample rate**: is frequency in Hz used to sample the data (default: 1 kHz)
- **Number of sample points**: number of data points per acquisition step. It is highly recommended to take the same value as chosen for the sample rate (default: 1000).
- **Order**: order of the used Butterworth LPF. The higher the order of the filter the smoother the treated input data. A low order value leads to a noisy result, quite similar to the original data sequence while a high order value could flatten the slope of the treated data too much. Consequently small changes of the measured current cannot be identified anymore. (default: 3).
- **Cut-off frequency**: the value corresponds to the highest frequency of the input signal surpassing the Butterworth LPF. Higher frequencies lead to an unsteady slope of the treated data due to the different noise effects. It is recommended to choose a value lower than the utility frequency of the electric power grid (< 50 Hz, default: 30 Hz).

- **Observation period**: period of time which is chosen to monitor the medium term behaviour of the deposits (default: 15 s).
- **Number of smoothing points**: number of data points used for finding the median around a specific data point (default: 10).

The time needed for every post-processing step of the incoming data is tracked and presented above the upper data display in various text boxes for every acquisition step. Between two consecutive acquisition steps a small period of time is passed before data acquisition starts again. The delay can be averaged to approximately 63 milliseconds and is caused during storing the data sequence of one acquisition step to the hard disk of the computer. Compared to the total amount of recorded time of 1 second this value is quite small and can be neglected. In case of an automated measurement setting like the I/U characterization these delays add up and have to be considered in further treatment steps (see chapter 2.3.2.2).

The main task of post-processing software was extracting relevant data-points from the data set acquired during one recording session for further treatment or graphical interpretation. In this step the initial data sequences of the measurement signal are treated again, while the data sets that have been already treated with LABVIEW are left unattended. Typical problems which are convoluted to the measurement signal are frequencies of the electronic power grid and different noise effects from the involved electronic devices like thermal noise and flicker noise. The software programs for offline processing were developed using MATLAB [30] and provided also a GUI for comfortable editing the post-processing parameters during the data treatment. Furthermore the program has two different program modes; both specialized to characterize the behaviour of the deposits depending on the kind of experiment (Figure 29).
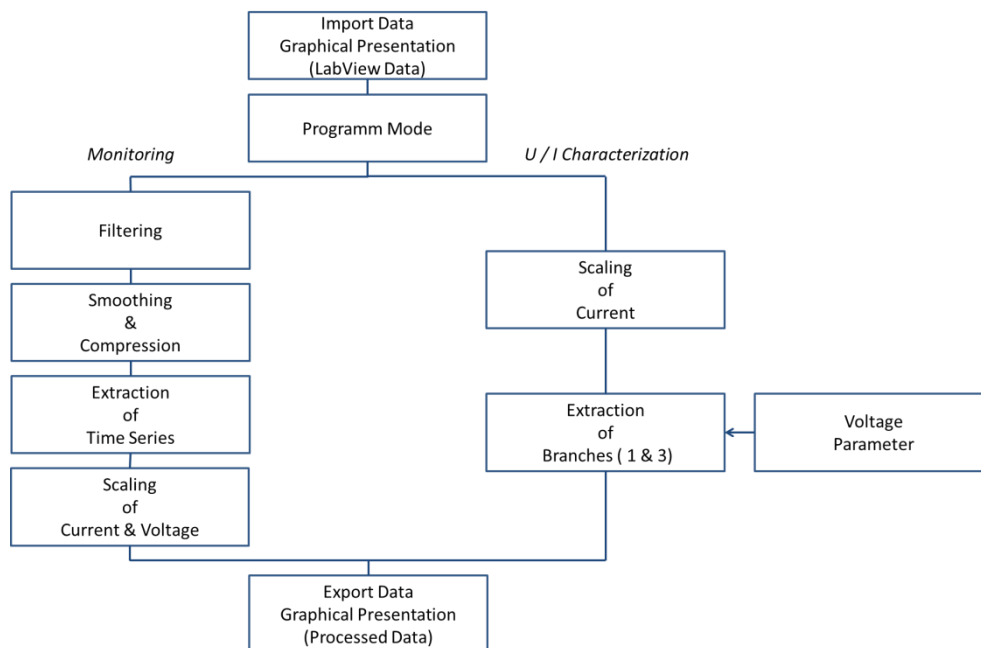
Figure 29: schematic illustration of the steps built in the post-processing software.

Data treatment begins with importing the whole data set obtained during one acquisition session. This step is finished by a graphical presentation of the data set and according to the kind of experiment the proper program mode has to be chosen. The program mode "Monitoring" has to be

applied for experiments concerned on the sensing abilities of the deposition. "I/U Characterization" is designed to treat data-sets obtained during the conductivity measurements.
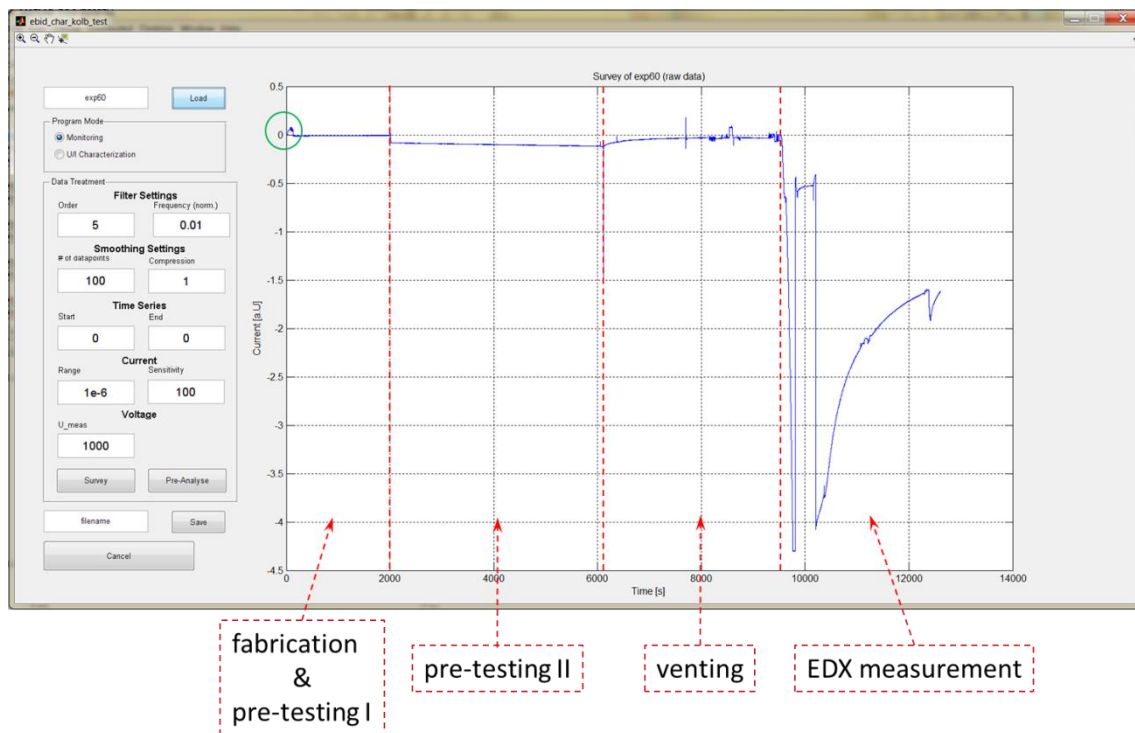
Figure 30: GUI to support analysing the results obtained during investigation of sensing abilities.

At the "Monitoring" application data sets can be filtered and smoothed, enabling data treatment with different process parameters than during the recording session (Figure 30). An additional feature is compression of the data set, where a specific amount of data points is averaged into one data point minimizing the size of the data set and thus speeding up subsequently treatment steps. Separating a specific data set from the whole recording session can be done by declaring start and end of the specific time series. Finally the extracted data set can be scaled to its actual dimension by declaration of used measurement range at the electrometer and the applied voltage. Figure 30 shows the fabrication and some experiments which have been conducted afterwards. The part where the fabrication happened is highlighted by the green circle and lasted about 100 s, resulting in a deposit of about 5 nm. During the first pre-testing part a voltage of 10 mV was applied to investigate the self-curing process of the deposit. In the next part the voltage had been raised to a value of 50 mV, leading to an accelerated speed of the self-curing process. Subsequently the deposit was exposed to ambient air, by venting the vacuum chamber of the DBM, which resulted in an increase of the current. The behaviour of the deposit responding to the exposure to ambient air with a humidity of ≈ 30% is discussed in more detail in section 3.5.1. This series of experiments was finished by EDXS measurements to investigate whether an electromigration of the Pt crystal can be observed, which did not happen (see section 3.4). The massive increase of the current can be explained due to the additional electron dose during the EDXS measurement. This leads to a further fragmentation of incompletely dissociated precursor molecules and small growth of Pt crystals, leading to an improved conductivity of the nanogranular structure [17].
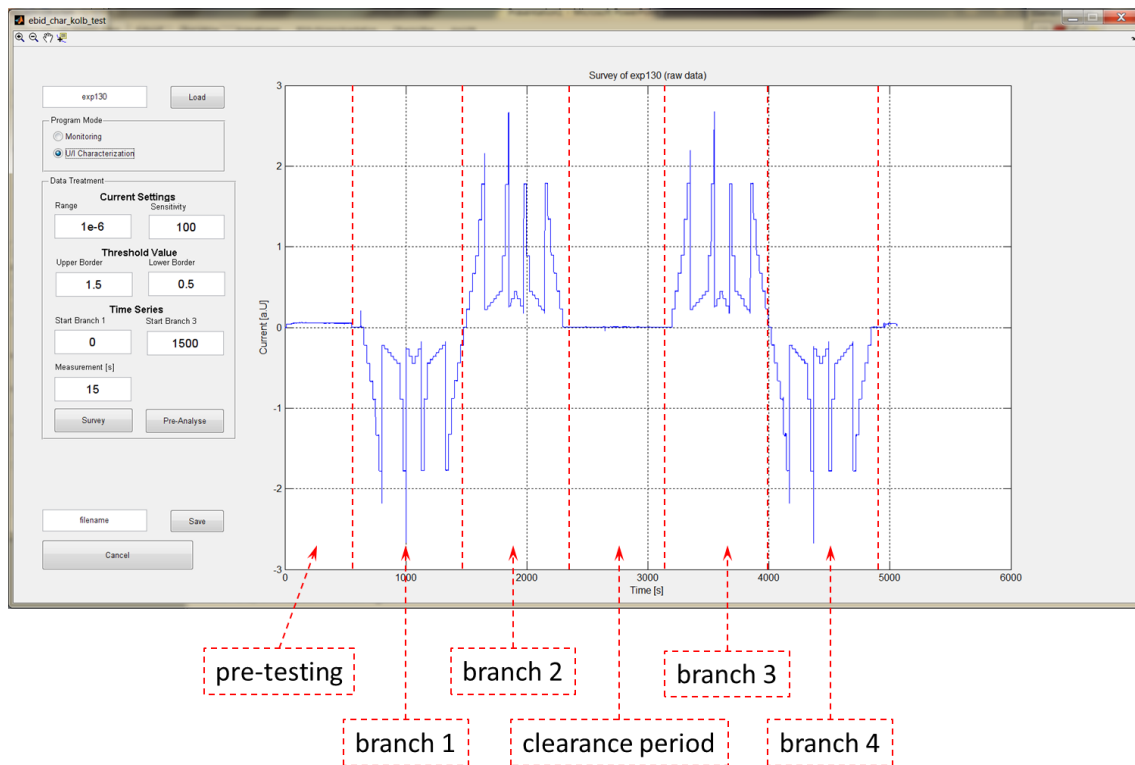
Figure 31: GUI to support post-treatment steps of the data obtained during U / I characterization.

Data sets obtained during I / U characterization are not treated by post-processing steps like filtering and smoothing. The main task of this program mode is to extract measured currents during voltage sweeps for each applied voltage respectively. The values of the applied voltages are loaded separately from a data file created by the user previous to the treatment step. To calculate the resistance and later on the resistivity the currents are scaled in the right dimension according to applied range and sensitivity of the electrometer. Figure 31 shows a typical result obtained from the U / I characterization. This procedure is subdivided into four different voltage sweeps in the range of ± 1V. Every sweep is further divided in different voltage steps, which can be chosen freely and have to be entered separately by the operator in the programmable voltage source (see section 3.3.1). The four pyramid-like shaped slopes in the data display are representing each measurement branch of the U / I characterization. The steps-like features of the slope display the different voltages, applied for a specific period. However, the slopes of the pyramids are not increasing steadily, caused by the changing sensitivity level which scales the data points by a factor of 10, when a value of ± 2 is exceeded. The occasionally occurring spikes in the slopes are generated because of the changing sensitivity level. Furthermore the size of the sensitivity level has to be noted by the operator at the beginning of each measurement, so the currents can be scaled in the right dimension.

2.3.3 Humidity Measurements – NTC

The investigation of the sensing capabilities of the fabricated PtC deposits has been done at the humid measurement plant at the NTC WEIZ [31] together with DI Kerstin Schmoltner and Dr. Andreas Klug.
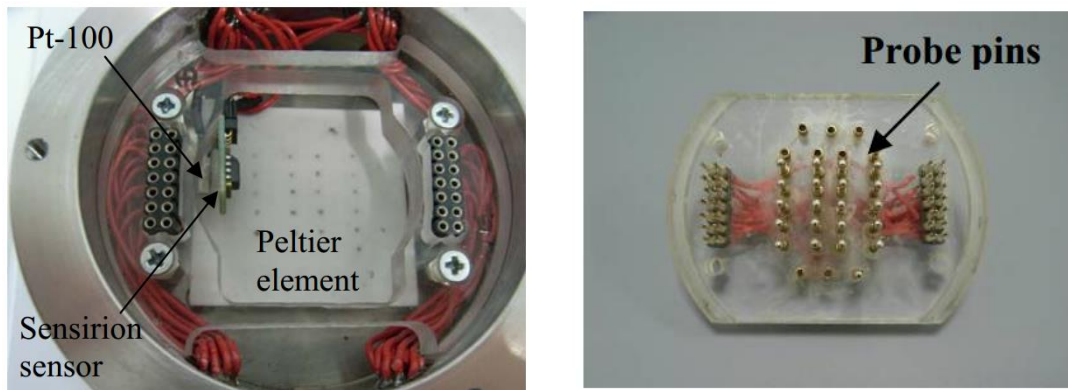
Figure 32: left: probe chamber of the measurement plant at NTC WEIZ; right: cover of the probe chamber with probe pins contacting the substrate [32].

The substrate with the PtC devices is placed on a Peltier element for variable temperature experiments as shown in Figure 32 on the left. The sample is contacted in the probe chamber by probe pins via constant spring force. The pin array is shown in Figure 32 at the right which is placed on top of the entire sample holder shown on the left of Figure 32. Desired humidity levels can be achieved by mixing dry and wetted N_2 gases (Figure 33). The N_2 gas gets wetted by bubbling through a humidifier. The amounts of the dry N_2 gas and the humidified N_2 gas are varied in each case by the mass flow controller HFC-302 (Teledyne Hastings Instruments) with a Schaefer Flow-Controller Power Supply PSCT, max 1 and 5 SLMP (1.69 Pa m^3s^{-1} and 8.4 Pa m^3s^{-1}) for nitrogen, respectively.
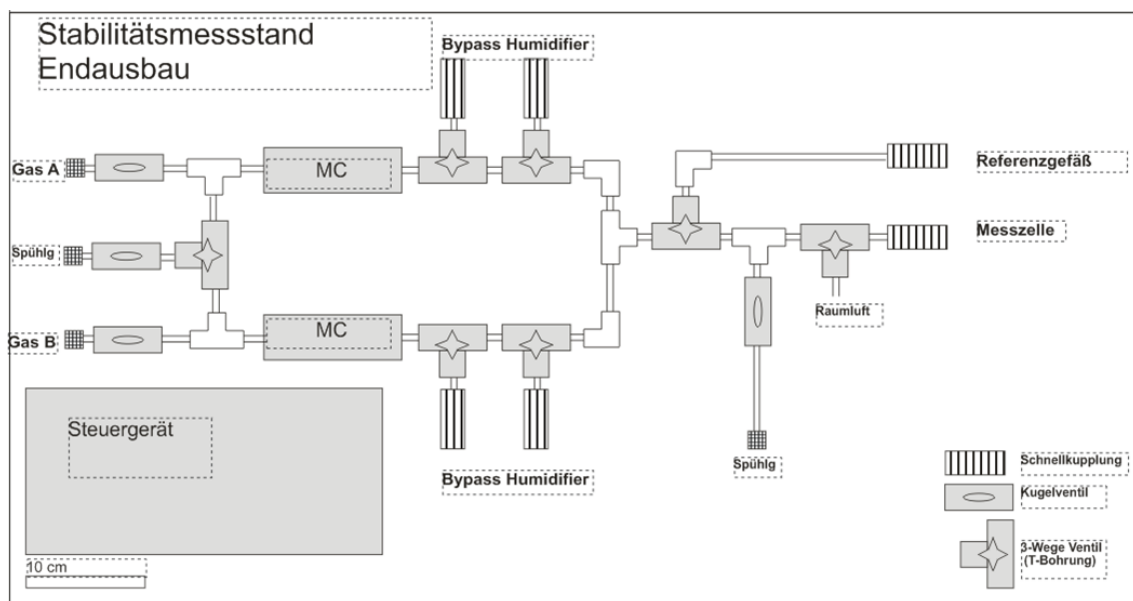
Figure 33: scheme of the utilized humidity measurement plant at NTC WEIZ [33].

Inside the probe chamber there is a temperature sensor and a humidity sensor positioned next to the substrate (Figure 32). The temperature sensor is a Pt-100, while for the humidity sensor the SHT21 (Sensirion) is used. The humidity sensor provides an additional temperature sensor. Measured temperature and humidity levels are tracked by a custom LABVIEW software program which is called Humidity Measurement Environment (**HME**). Furthermore the HME software regulates the amount of gas passing through the mass flow controller. This enables automated cyclic humidity variations or reaching a desired humidity level and staying on this level for a specific period of time. The

temperature inside the probe chamber can be changed by a Peltier element. However the temperature of the Peltier element cannot be regulated by the HME, but by varying the applied voltage manually. To figure out the right voltage level for the desired temperature inside the probe chamber a table containing the voltage values is used. The temperature inside the probe chamber is then checked by HME software and if necessary, the applied voltage on the Peltier element is varied again.

At the beginning of the humidity measurements the substrate is mounted inside the probe chamber. Subsequently the probe chamber is sealed by fixing the cover on top of the chamber and the substrate is electrically conducted with the probe pins. In the next step the probe chamber is evacuated with an attached membrane vacuum pump and a turbo molecular pump, until a pressure of 10^{-4} mbar is reached [32]. The humidity level inside the probe chamber reaches very low values beyond 5 %. After reaching the final pressure the probe chamber is flooded with dry N_2 gas and a clearance period is introduced until the humidity level is stabilized at a value of 5 %. Desired humidity levels can be reached by increasing or decreasing a fraction of the whole gas amount passing through the mass flow controller which is connected to the consecutively arranged humidifier. As the two temperature sensors are located at different positions a slight temperature difference between the temperature of the gas and the temperature of the substrate is observed. This discrepancy is caused due to the different locations the sensors and will be discussed in further detail in section 3.5.1.1.
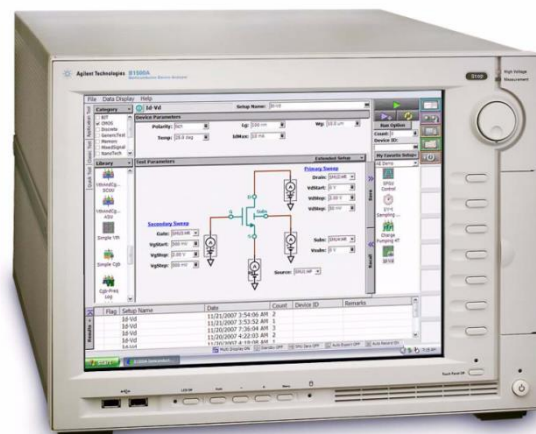
Figure 34: the utilized parameter analyser Agilent 1500A [34].

2.3.4 Electrical Measurements - NTC

The electrical characterization is done via an Agilent 1500A parameter analyser. It is a so called one-box-solution which enables the measurement / output of DC voltages and currents plus AC output of a signal and impedance measurements. Furthermore this device provides the operator with a GUI and a touchscreen in form of a LCD panel for comfortable editing the individual parameters in the GUI at the measurement device without the requirement of an additional PC equipped with appropriate data acquisition software.

The Agilent 1500A consist of two SMUs, enabling various operation modes like applying a voltage and measure the current, applying a current and measure the voltage, applying a current and measure the current as well as applying a voltage and measure the voltage (Figure 35). For our purposes the

used operation mode was to apply a voltage and measure the current, which was the same mode as it had been done for the measurements conducted at the FELMI institute. The results of this investigation are presented in section 3.5.1.1 and 3.5.1.2 respectively.
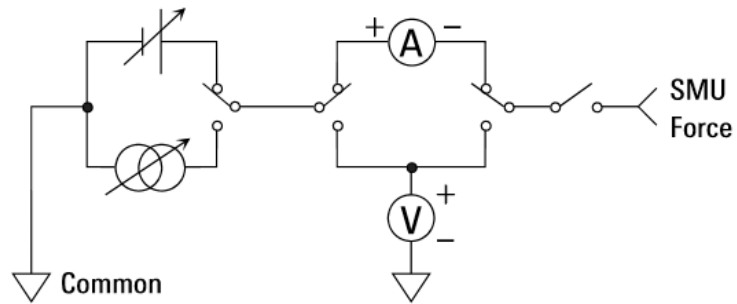
Figure 35: schematic circuit diagram of the SMUs in the utilized Agilent 1500A [34].

3 Experimental Results

3.1 PtC Sensor Fabrication

Prior to the actual fabrication step of the deposits, the properties of the electron beam especially with the inserted GIS-needle have to be checked and, if necessary, changed as these parameters strongly influence the geometric shape and chemical composition of the deposits. For reliable device comparisons it is important that the deposit footprint stays the same while its height is varied, which is controlled by the deposition time.

After optimization of the electron beam, the beam was blanked to prevent unwanted carbon contamination and the correct patterning parameters depending on the desired working regime (RRL-regime or MTL-regime) have been set. After opening the GIS valve, an additional stabilization period of at least 5 minutes was introduced to ensure an thermodynamic equilibrium state of the precursor molecules on the surface (high coverage and adsorption rate = desorption rate; see section 2.1.10.3). For all experiments the electron beam voltage was set to 5 kV while the current of the electron beam was fixed at 1600 pA as a result of pre-investigations [25,16]. The yielded deposits show a typical Pt content of around 10 - 15 at.% with Pt grain diameters between 1.7 and 2.2 nm [15,17] as representatively shown in Figure 36 by TEM bright field image.
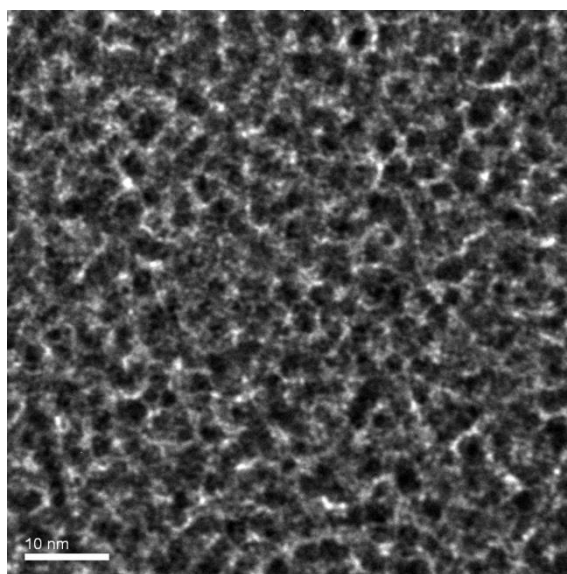
Figure 36: zero-loss filtered bright field TEM image of a typical PtC deposit revealing the small Pt grains (~ 1.7 nm – 2.2 nm) as dark parts embedded in the carbon matrix (bright parts) [3].

After finishing the deposition procedure the GIS needle is moved back in its initial position and an additional clearance period of at least 15 minutes is introduced to remove volatile precursor molecules from the substrate surface and the vacuum chamber. The electron beam is kept in its blanked position to prevent any changes of the nanogranular system of the deposit introduced by an additional electron dose (see chapter 2.1.10.3) [17]. Please note that initial pre-experiments allowed the estimation of a lateral drift during deposition based on local charging which has been found to be acceptable compared to the final footprints used for the actual sensors.

Table 2 and Table 3 summarize the applied patterning parameters for the PTC deposits with respect to AFM height calibration (section 3.2), I / U characterization (section 3.3) and the investigation of the sensing abilities (section 3.5). The slight difference in the point pitch and the dwell time between Table 2 and Table 3 originates from the final adaption of the process parameter during U / I characterization to 10 s frame time due to synchronization reasons. The effect on height, however, is found to be negligible.

Table 2: applied process parameters for AFM height calibrations.

footprint of deposits					
length: X = 20 µm					
width: Y = 5 µm					
applied process parameters					
mass-transport-limited (MTL) regime			reaction-rate-limited (RRL) regime		
dwell time (t_d) :	10	[µs]	dwell time (t_d) :	10	[µs]
point pitch :	13,5	[nm]	point pitch :	115	[nm]
defocus :	0	[µm]	defocus :	250	[µm]
frame time (t_f) :	5,52	[s]	frame time (t_f) :	76,5	[ms]

Table 3: applied process parameters for U / I characterization and investigation of sensing abilities.

footprint of deposits					
length: X = 20 µm					
width: Y = 5 µm					
applied process parameters					
mass-transport-limited (MTL) regime			reaction-rate-limited (RRL) regime		
dwell time (t_d) :	18	[µs]	dwell time (t_d) :	10	[µs]
point pitch :	13,5	[nm]	point pitch :	115	[nm]
defocus :	0	[µm]	defocus :	250	[µm]
frame time (t_f) ::	10	[s]	frame time (t_f) :	137,8	[ms]

After completing electrical pre-characterization, the relevant deposit is separated from the electrode structure by a FIB assisted double cut across all gold leads as shown in Figure 37. The parameters for the focused ion beam were 30 kV and 50 pA (beam current) with a total time of about 10 s until electrical in-situ measurements proved the separation (the second cut was done to ensure full separation). The FIB cutting was done with a single line which was pre-aligned with the electron beam prior to all experiments (see section 2.1.1).
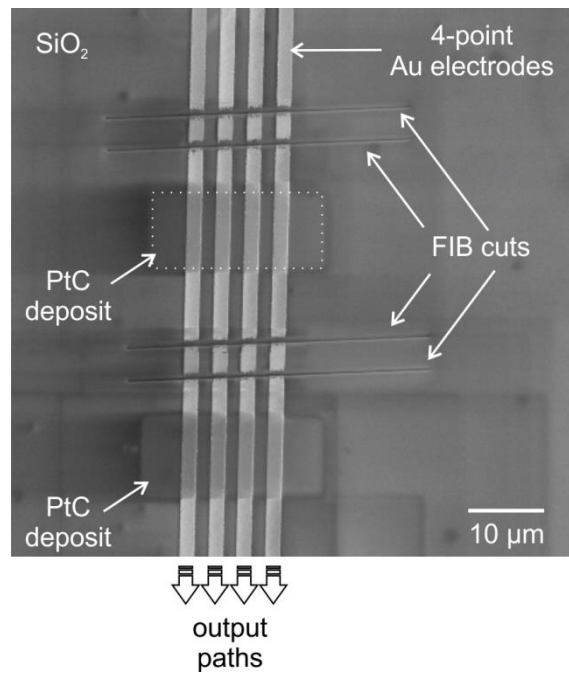
Figure 37: PtC deposits across a 4-point electrode structure on SiO₂ which has been separated via the ion beam.

3.2 AFM Assisted Height Calibration

Since the determination of ρ requires the knowledge of the deposit heights (see Equation 12 and Equation 13) it is essential to know the geometry of the deposits. While the length is given by the electrode distance to 2 μm and the width can be accurately controlled by the patterning engine, the deposit height is not directly accessible during or shortly after deposition. The only way would be through AFM measurements after each experiment which is time intensive because of the large number of deposits investigated during this thesis.
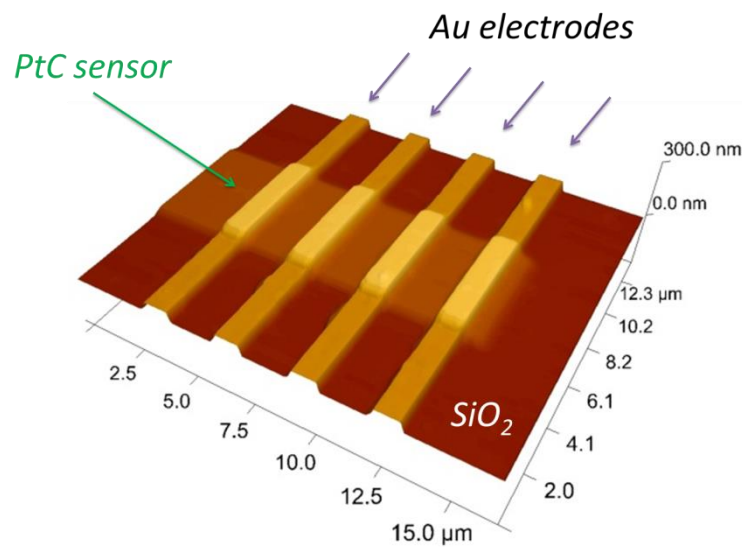
Figure 38: 3D image of the deposit and electrical 4 point structure reconstructed from recorded AFM data.

To compensate for this problem an alternative approach by means of a height correlation with one deposition parameter has been chosen. Basically, two parameters would work: 1) the number of patterning loops; and 2) the total exposure time (**TET**), both given set of the parameters specified in Table 2 and Table 3. The latter has been chosen for the correlation parameter since the deposit footprint has been kept constant throughout this thesis which justifies the usage of this parameter.
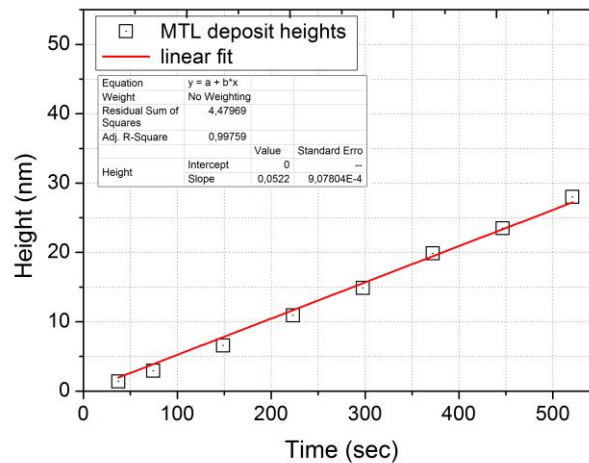
Figure 39: deposit height in dependence of TET fabricated in the MTL regime.
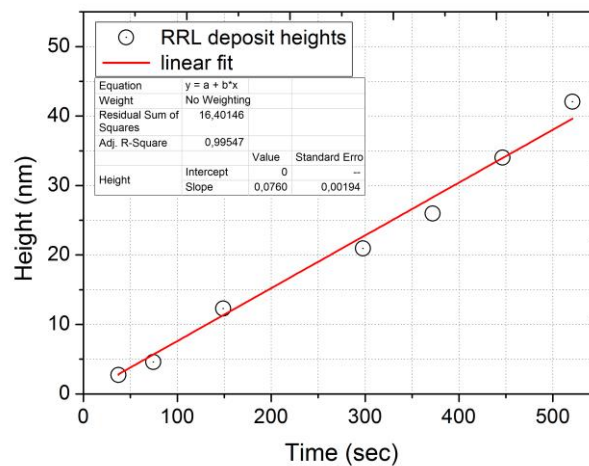
Figure 40: deposit height in dependence of TET fabricated in the RRL regime.

The heights of the PtC deposits were measured with AFM and the results plotted in dependence on the used TETs. Figure 38 shows a representative AFM height image of a PtC layer across a 4-point Au structure used for further calculations. Fitting the obtained data points with the ORIGIN software revealed a linear behaviour of the height growth as shown in Figure 39 and Figure 40 for MTL and RRL conditions, respectively (see also section 2.1.10.3). As it is known from previous investigations, the resulting heights in the RRL regime are about 45 % higher than for MTL conditions. In more detail, the growth rates have been found to 0.76 $\mu m^3 s^{-1}$ and 0.52 $\mu m^3 s^{-1}$ for RRL and MTL conditions, respectively. Basically, the difference is the result of depletion effects of the local precursor coverage due to varying *electrons-per-molecule ratios* (increasing ratio for MTL conditions) [12,18].

By knowing the functional relation between TETs and the growth heights, it is now easily possible to produce devices with any desired height with a small insecurity of about ±2 nm. The only constrain is that the same preparation parameters and the same footprint has to be used since lateral downscaling would change the refresh time (RT), which is responsible for the repopulation of precursor molecules on the substrate surface.

To compensate the final insecurities via AFM correlation (specified above) another cross-check prior to any measurement has been introduced. All deposits used for AFM analyses have been investigated electrically as well. The obtained values act now as double cross check after deposition. If the as-prepared current deviated clearly from the reference values, the deposit was not used and another one has been prepared (see also section 3.3.3).

By that, TETs could be used for controlling the deposit heights and by that allow the recalculation of reliable ρ values.

3.3   U / I Characterization

3.3.1   Basic Behaviour

The U / I measurements have been done in the range ± 1 V and consisted of 4 individual voltage sweeps (branches) as representative shown in Figure 41 for a 10 nm PtC deposit (MTL): *i)* 0 V $\rightarrow$ +1 V $\rightarrow$ 0 V (black); *ii)* 0 V $\rightarrow$ -1 V $\rightarrow$ 0 V (red); *iii)* 0 V $\rightarrow$ -1 V $\rightarrow$ 0 V (green); and *iv)* 0 V $\rightarrow$ +1 V $\rightarrow$ 0 V (blue). To account for time dependent charging effects, a break of 1700 sec has been introduced in between branch *ii)* and *iii)*. Furthermore, the polarity sequence of branch *iii)* and *iv)* has been reversed to emphasize polarity related effects of the applied voltage. All branches are subdivided into 3 sections each having different voltage increments to increase the accuracy of the measurement for low and medium voltage values (see measurement points in Figure 41).

As can be seen in Figure 41, U / I characterization reveal a linear (= ohmic) behaviour which has been found for all investigated deposits in the mentioned voltage range. Even very thin layers of 5 nm show linear dependence of the measured current. A closer look on the region of ±100 mV reveals also fully linear behaviour around 0 V (see inset in Figure 41) which has been found for all deposits fabricated throughout this thesis. All measurements were performed at room temperature explaining the linear behaviour and the absence of a Mott-gap, which is typical for nanogranular material in the Arrhenius conduction regime at low temperatures (see section 2.1.10.4). To account for polarity induced effects, additional experiments have been performed by changing the polarity quickly at constant voltages. The obtained current was always identical which excludes a polarity dependent effect. Please note, previous studies focused on the influence of a permanent current vs. single measurements which revealed no effect on the electrical resistivity [25].

However, as a closer look to Figure 41 reveals, the 4 branches are not lying on each other. Since the individual measurements require 850 sec acquisition time each, this indicates that the electrical resistivity is not constant after deposition. Considering the evolution of the slopes it becomes evident that the resistivity decreases with time which requires a careful characterization of self-curing effects discussed in the following chapter.
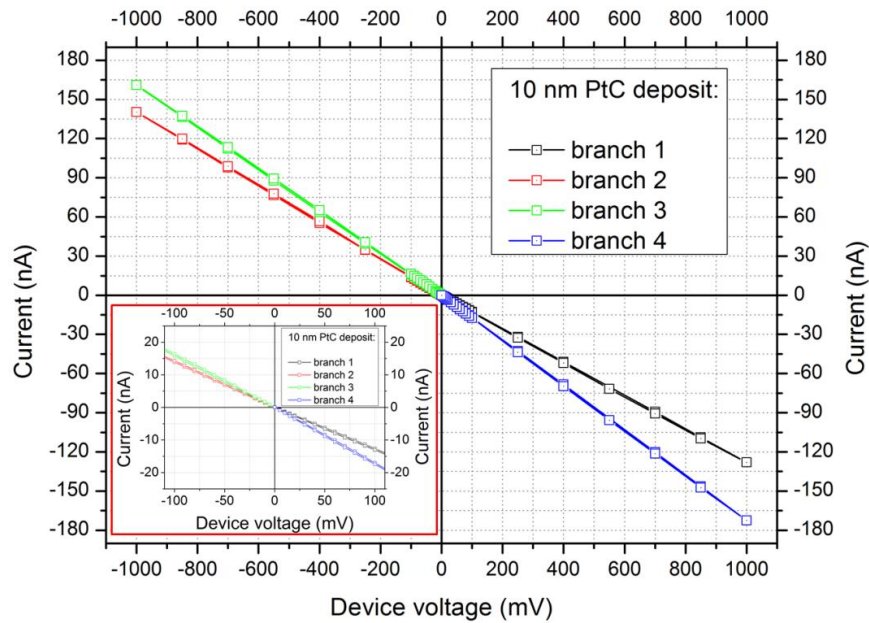
Figure 41: representative multi U / I sweep performed for each deposit made (shown are the results for a 10 nm MTL deposit). The inset shows the linear behaviour from -100 mV to +100 mV.

3.3.2 Time Dependency

As described in the previous section and depicted in Figure 41 the resistivity changes with time, especially after the deposition process. Since this would imply that following humidity measurements depend on the storage time after deposition, it is essential to know about this self-curing effect qualitatively and quantitatively. In the following to sub-sections, this time dependency is discussed for vacuum and ambient conditions.

3.3.2.1 *Vacuum Conditions*

First investigations have been performed in vacuum conditions due to the absence of any (reactive) gas which can e.g. penetrate into the layers and / or change its chemical peculiarities. By that, only intrinsic effects are observed which might be outwards diffusion, internal chemical reactions or rearrangements of the inner structure.

To do so, the relative resistivity change (calculated by Equation 13) of two subsequent measurement branches (see Figure 41) have been calculated and plotted individually for increasing layer thicknesses in both precursor regimes (Figure 42).

As can be seen in Figure 42 by the circles, the resistivity for RRL reveal a stronger variation for thin devices and saturates at a more or less constant value which is, however, not zero. Furthermore, it can be seen that the changes are slightly stronger for early stages (from top to bottom) but not too different. In contrast, MTL deposits changes generally much stronger for different thicknesses and for different time states (from top to bottom). Also a reduced variation could be observed for later stages.
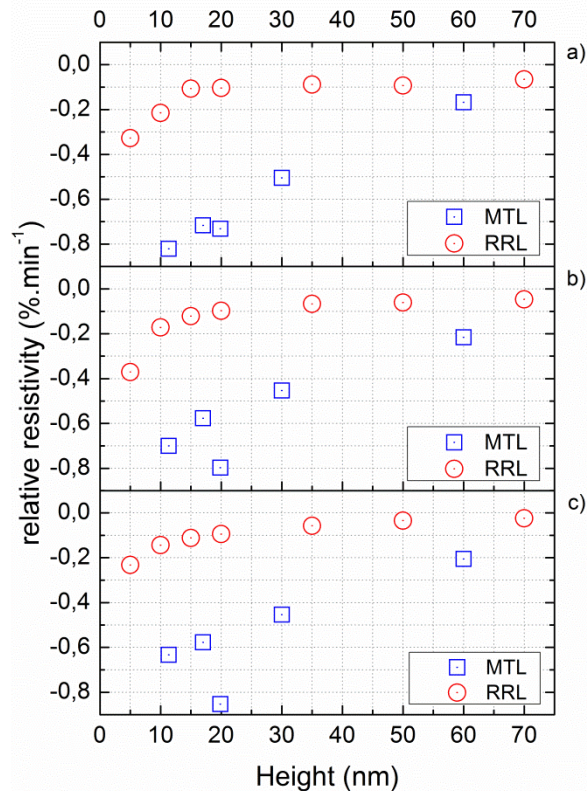
Figure 42: relative change of the resistivity during the U / I characterization; a) transition branch 1 to branch 2, b) transition branch 2 to branch 3, c) transition branch 3 to branch 4.

From previous studies at the FELMI it is known that RRL conditions are defined by a lack of dissociating electrons compared to available precursor molecules. This leads to the incorporation of incompletely dissociated molecules in the deposit. On the other hand, MTL conditions are achieved by an excess of dissociating electrons compared to available precursor molecules. This leads to the situation of electron beam induced polymerization of precursor fragments which are then incorporated in the deposits [16]. Such carbon complexes can be reactive or even mobile after the deposition process. This explains why the resistivity changes for MTL deposits are stronger compared to the incompletely dissociated RRL deposits where it is known from literature that auto-dissociation is unlikely for the precursor used [12,17]. Basically, two effects are conceivable for the observed resistivity variations:

1. Interdiffusion of mobile fragments leading to chemical effects
2. Diffusion of volatile fragments to the surface where it can leave the deposit

Considering that the self-curing process is a function of the layer thickness for both regimes, an interdiffusion effect is less likely since thicker and thinner layers should contain the same relative content of responsible fragments. Hence, the variation should be similar which is contradictory to the observations in Figure 42.

On the other hand, diffusion effects of volatile fragments towards the surface where they can leave is more reasonable: the very small pathways of carbon in between the Pt nanocrystals complicate the outwards diffusion which explains the lower relative variations for thicker layers.

Hence, it can be stated that such vacuum experiments of the self-curing effect suggest strongly, that the observed variation effects might be driven mainly by diffusion of volatile products towards the layer surface where they can leave. This is furthermore stronger for MTL deposits where a higher number of radicals / (di)polymerized fragments are incorporated into the deposit as a consequence of the deposition conditions. All deposits show an increasing current for the early stages considered in this experiment meaning decreasing resistivities.

In the next step, same experiments are performed in ambient conditions which are discussed in the next section.

3.3.2.2 Ambient Conditions

According to the results in Figure 42 where MTL deposits have been found to be more demanding, further investigations concerning the temporal resistivity evolution have been conducted and expanded to ambient conditions during self-curing. This was done since it was unclear how long the deposits will need to settle completely (if so) which was impossible to do in the vacuum chamber for a long time (blocked instrument). The basic preparation parameters were chosen according to Table 3 and different layer thickness between 5 nm and 60 nm have been fabricated to investigate both, time- and thickness-dependency. After successful fabrication of all deposits on one single substrate, the sample was exposed to an air conditioned room (~ 20 °C and 30 % humidity). After mounting the sample in a special sample holder, which is actually used for active AFM measurements with same sample geometries, a long time measurement was started. During a monitoring period 54 days a single current measurement per day at a voltage of +1 V was performed (less than one minute) to reduce the risk of current induced effects although it has been shown before that such effects are not occurring [25]. In Figure 43 the measured data normalized to its initial values can be seen and reveal immediately a basic difference compared to vacuum conditions: the currents decrease on a long time scale while they increase for early stages as discussed in the previous section.

As found for early stages, the self-curing rate for the resistivity is related to the height of the deposits: thin layers (< 10 nm) decay significantly faster and steady current values are reached in less than a week and settle around a value of 3-5 % of the initial current value (see next chapter in more detail). Thick layers, in contrast, require very long curing times of 50 days and more, then settling at current values of about 10 % from the initial values. A closer look on the 60 nm deposits (stars in Figure 43) show furthermore an initial increase of about 50 % after the first day followed by the typical decay. Together with the results in Figure 42 (bottom) it becomes obvious that all layers show an initial decrease which lasts longer for thicker deposits. This is the reason why the 60 nm layer shows its initial current increase also in the long time measurements while the large time steps in Figure 43 prevent the direct observation of this effect for thinner deposits.

Therefore, we can summarize so far that the layers show always an initial current increase after deposition followed by strong current decrease to about 3 – 10 % of the initial values on a time scale between 5 and 50 days for thin and thick deposits, respectively.
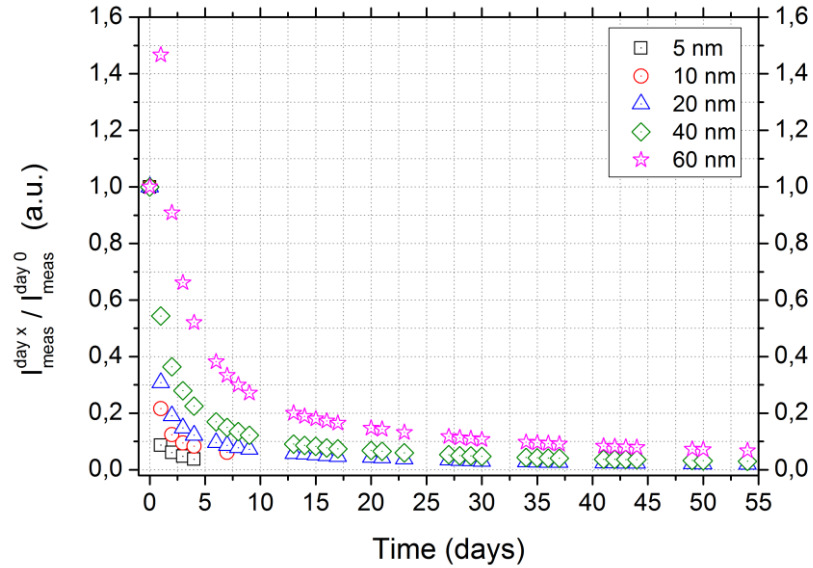
Figure 43: relative current decrease during long-time characterization over a period of 54 days for differently thick deposits.

The previously stated assumption that diffusion of volatile / reactive fragments is responsible for the variations also holds for the long time investigations shown in Figure 43. Due to the exposure to ambient conditions, another diffusion effect is conceivable by ambient gas molecules which can diffuse into the deposit and cause chemical / structural changes. Although it is not subject of this thesis to determine the diffusion processes in detail (an according Master Thesis is scheduled in fall at the FELMI), it is possible to analyse the decay functions by numerical fitting according to the custom fit function:

$$\frac{I_{meas}^{day\,x}}{I_{meas}^{day\,0}} = \frac{1}{(1 + c * t)^{\frac{3}{4}}}$$

Equation 14

The fitting function has the time **t** as variable parameter and introduces an additional factor **c** [t^{-1}], which describes how fast the curing process takes place. Pre-testing confirmed the suitability of Equation 14 for deposit heights from 5 to 60 nm investigated during this thesis. As can be seen in Figure 44 the chosen function fits very well to the measurement points (see green curves) with R^2 deviation values of 0.99 and better. In case of 60 nm depositions the measured data had to be reshaped to fit properly in the assumed curing function (see Figure 45) by exclusion of the first value which is lower than the second measurement point as a result of the longer initial current increase, discussed above.
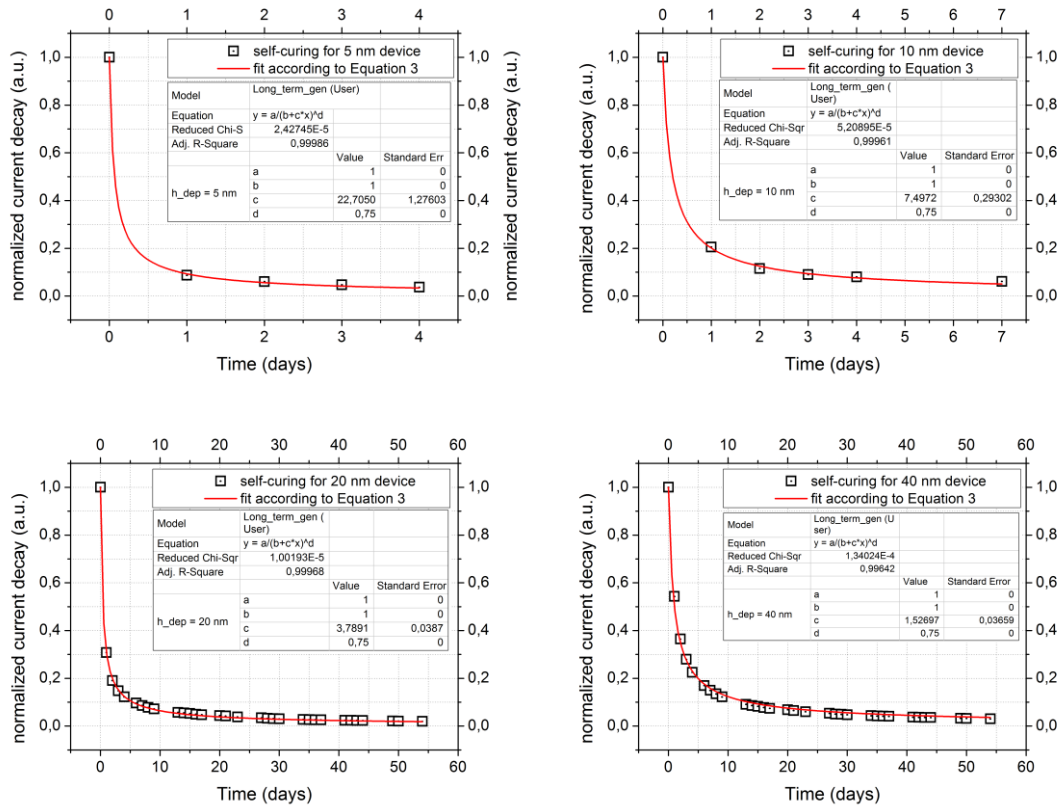
Figure 44: long-time current behaviour of differently thick deposits, including the fit function according to Equation 14.

As a result of the numerical fits, the curing factor c from Equation 14 can be determined for all thicknesses which are summarized in Figure 46. As it can be seen, the curve shows an exponential increase for thinner layers, meaning high self-curing speeds for such thin deposits. Considering the Pt grain size of about 2 nm (see section 3.1), it becomes obvious that very thin layer represents a 2D PtC network where all volatile fragments can leave the deposit almost immediately. Hence, a 3 nm layer has been fabricated and tested with same experiment conditions, however, with a strongly reduced voltages of 50 mV (instead of +1 V) in order to prevent current induced damage.
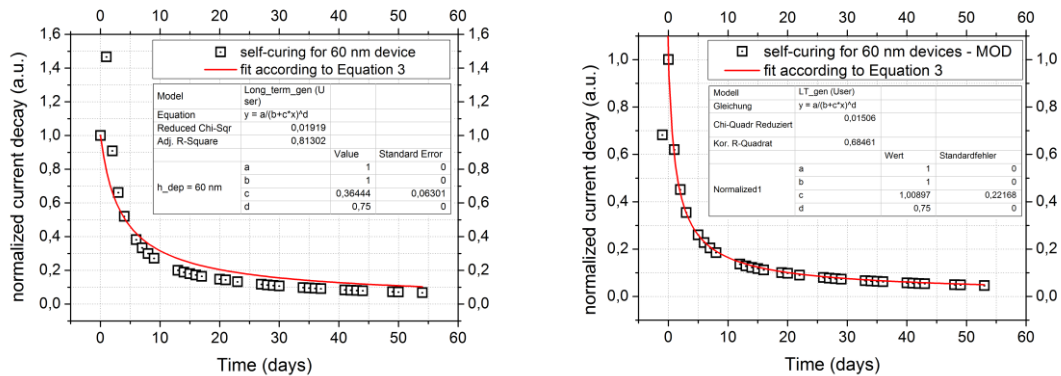
Figure 45: (a) long-time behaviour of the 60 nm deposit and the best non-linear fit; (b) rescaled long-time behaviour to the maximum relative current value and exclusion of the first measurement point (explanation see text).

The result is shown in Figure 47 revealing the same decay function as observed and fitted for other deposits. However, the curing factor *c* is massively increasing as a result of the 2D network (curing factor around 1000). Here, there is no underlying layer and all volatile fragments can directly leave the deposit without any diffusion. Once the layer thickness increases, it becomes more and more complicated for deeper embedded fragments to diffuse through the very fine network to escape the deposit. Hence, the curing factor decreases strongly for increasing thicknesses, meaning a longer time before the random diffusion based volatile fragments can leave the deposit.
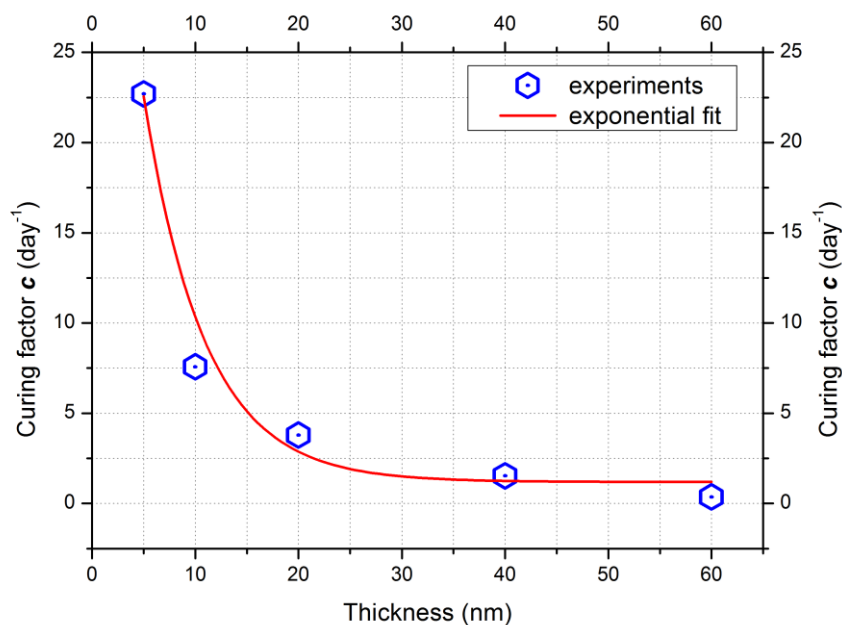
Figure 46: fit-parameters *c* obtained from the best non-linear fits of the deposits versus thicknesses.

Applying even a small voltage during the whole investigation leads to different behaviour of the measured current (Figure 47). However changing the exponent at the already known fitting function leads to a new curing function, which is in good agreement with the measured current. The variation of the functional behaviour could be due to the applied voltage affecting the diffusion processes or triggering interaction processes between substrate, deposition and the surrounding gas species. Further studies will be needed to figure out how the different possibilities of diffusion affect the curing process and why curing can be controlled by an applied voltage.

As a summary of the last two sections it can be said that the observed self-curing consists of a two-step process: **1)** slight decrease of resistivity for very early stages which attributed to remaining chemical reactions after the rapid dissociation process followed by **2)** a strong resistivity increase based on diffusion effects of volatile fragments (e.g. precursor remaining, incorporated (radical) (hydro)carbons from the chamber / sample surface). The thinner the deposit the easier the diffusion from underlying layers resulting in short settling times after fabrication. Please not, the effect of chemical reactions during diffusion cannot be excluded but is assumed not to be the major influence. This assumption is based on the fact that there should be a similar amount of reactive component in a relative volume independently on layer thickness. This however, is contradictory to the results which reveal strong thickness dependences. This can easily explained by random diffusion of fragments which need to find the surface before they can leave. Additionally, the very fine pathways

in between the Pt nanograins complicate the situation even more which is in agreement with the strong thickness dependence found during the long time experiments.
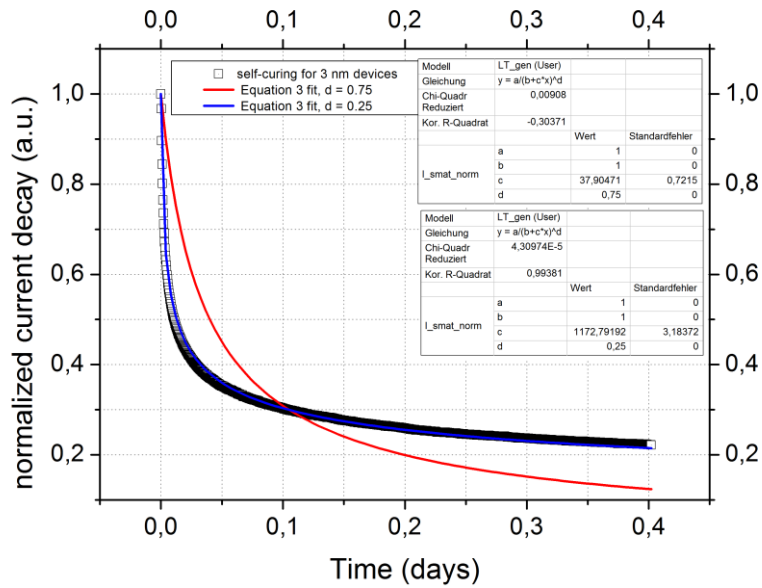
Figure 47: time dependent current variation and fitting functions for 3 nm deposit with an applied voltage of 50 mV.

3.3.3   Skin Effect

As discussed in the previous section 3.3.2, the deposits need some time before its resistivity reaches a constant value. Since a thickness dependency was found for their self-curing, it is very likely that also the final resistivities show a thickness dependency. For this purpose we first measured the U / I characteristics after the self-curing has been settled. The results are shown in Figure 48 for a thickness range of 5 – 70 nm. As it can be seen the linear characteristics, as observed directly after deposition in Figure 41, is still present even for very thin devices (inset) and low voltages around 0 V.
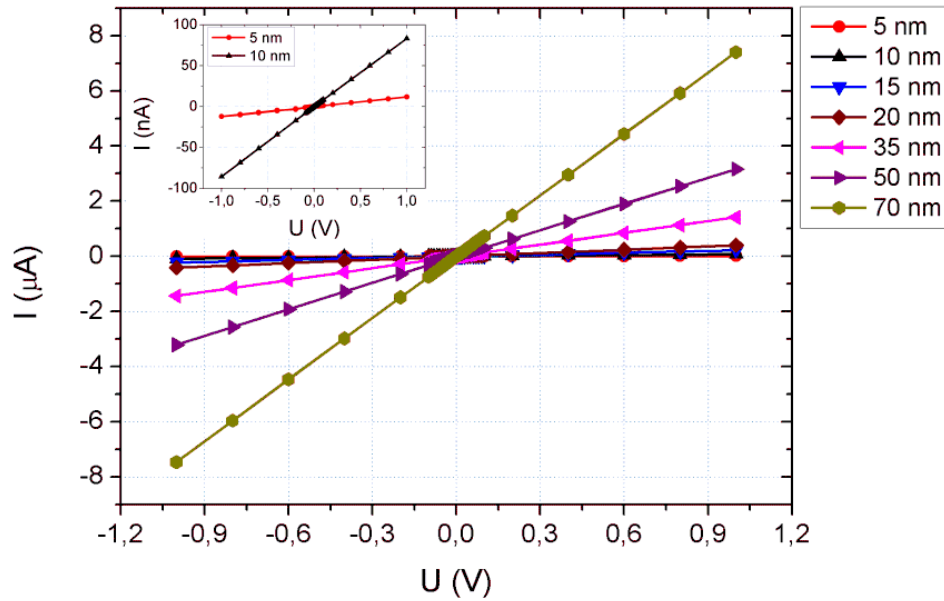
Figure 48: U / I characterization of depositions with varying height fabricated MTL regime.

Based on the results in Figure 48 and the knowledge about the deposit cross sections, the settled resistivities can be extracted which is summarized in Figure 49 for both, MTL and RRL regimes. The semi log plot reveals strongly nonlinear behaviour of the resistivity in dependence of the height for both precursor regimes. As can be seen, the resistivity increases for very thin layer by more than 2 orders of magnitude while the different working regimes show only differences for layers < 10 nm. The most remarkable detail however, is the fact that the resistivity increases strongly for thicknesses below 20 nm (see Figure 49).
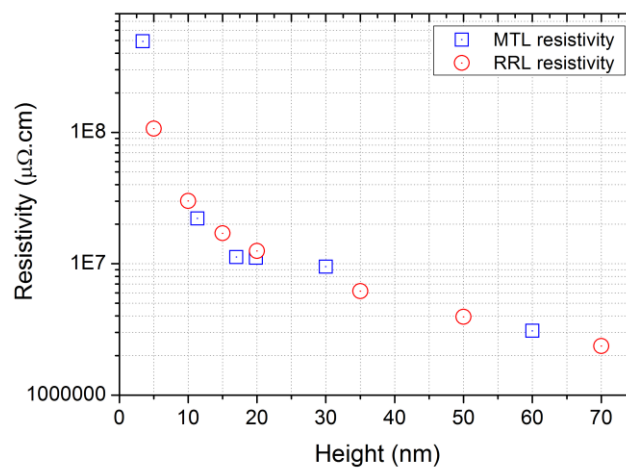
Figure 49: final resistivities of the PtC deposits after settled self-curing for both precursor regimes.
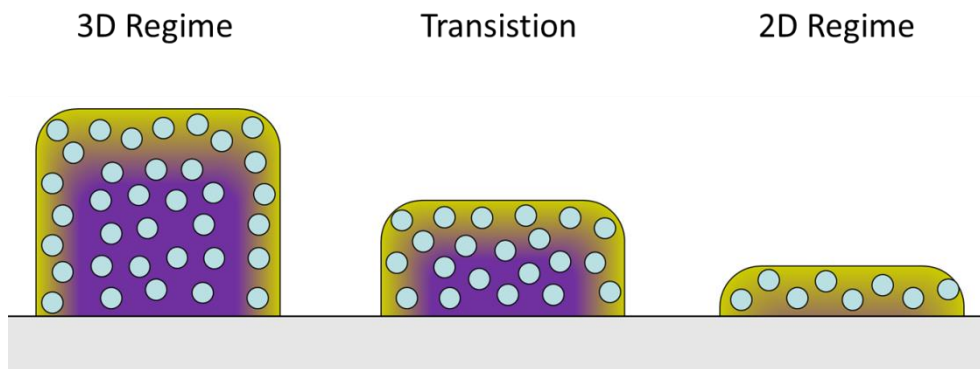
Figure 50: schematic of the nanogranular materials and its effects during downscaling. Purple areas represent bulk areas whereas green areas indicate the quasi-single layer with a 2D conduction network.

This observation can be explained by geometrical changes which influences the electrical transport in such deposits. Figure 50 shows a cross sectional schemes for different heights taking into account the nanogranular nature of the PtC deposits. The metallic nanoparticles (blue circles) are isolated from each other and embedded in a non-conducting carbon matrix [12,15,17]. Starting at the left deposit, the cross section can be subdivided in two different regions, as indicated by different colours in Figure 50: **1)** bulk areas (purple) in deeper regions where all particles are surrounded by other Pt grains in all three directions; and **2)** quasi-single layer on the deposit surface (green) where a reduced number of adjacent grains can be found. The thickness of this second layer is defined by the grain size and its in-plane orientation and can be estimated in the range of about 3 nm. For decreasing thicknesses (from left to right in Figure 50) the bulk component is more and more reduced which ends up in the situation of a quasi-single layer for very thin layers (right). Considering the electron transport in such nanogranular materials (see section 2.1.10.4) this change implies the change from a 3D conduction into 2D conduction regimes which results in a massive increase of the resistivity as the number of the available grain sides for an electron hopping from one grain side are decreased massively. This effect, which is further denoted as skin effect, explains the strongly increasing resistivities for thinner devices (Figure 49) by a regime change for the conduction from 3D towards 2D. Furthermore, this concept might also explain why extremely thin layers of about 3 nm, as shown in Figure 47, behave strongly different compared to slightly thicker deposits. Hence, 5 nm deposits have been defined as thinnest deposits under investigations to prevent problems with significance and comparability to other data.

3.3.4   Non-Linear Behaviour at Elevated Voltages

As has been shown in previous literature by Gazzadi et.al., strong electric fields and the entailed high current densities can cause non-linear behaviour PtC nanowires [35]. According to these results we enhanced our U / I measurements up to ±12 V. As representatively shown in Figure 51 for 5 nm (top row) and 20 nm (bottom row) the non-linear behaviour starts at an electric field of 2.5 V.µm^{-1} (see top axes) which equals a voltage of 5 V for all 4 measurement branches (left column), as specified in section 3.3.1. The right column in Figure 51 shows only branch 1 and 2 corresponding to positive and negative voltages, respectively, together with the linear fit based on linear range between ±2 V. This indicates clearly the non-linear behaviour, its individual starting points and the fact that both polarities lead to the same effect.
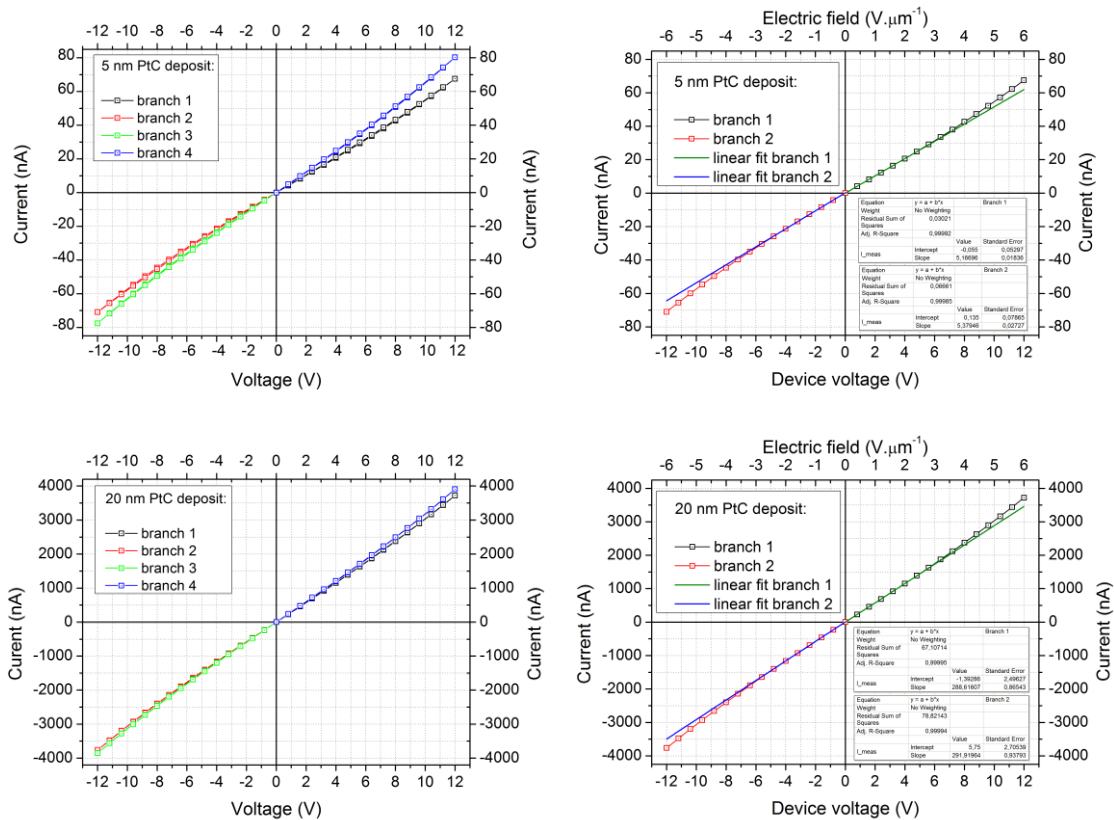
Figure 51: U / I characteristics for 5 nm (top row) and 20 nm (bottom row) PtC deposits, showing all four measurement branches (left column) up to ±12 V. The right column shows only branch 1 (positive sweep) and branch 2 (negative sweep) together with the linear extrapolation accodring to the linear range between ±2 V to visualize the non-linear behavior for higher voltages.

Decreasing the voltages back to lower levels restores the linear characteristics again, which indicates that the PtC deposits do not undergo an irreversible structural and / or chemical transition. While the study of Gazzadi mentions a structural transition for electric field above 4.7 V.μm^{-1}, our experiments do not show any sign of irreversibility even for 6 V.μm^{-1}. The discrepancy between these experiments is the geometry investigated. While Gazzadi et.al. characterized nanowires with diameters around 100 nm, we have a footprint of 10 μm^2. Therefore, we can conclude that although it is known that PtC nanostructure can tend to electromigration, by means of phase separation between Pt nanograins and the carbon matrix, this effect does not play a major role for our layers. As will be shown in section 3.4, further analytic measurements via X-ray spectroscopy based elemental mapping confirm the absence of any electromigration effects for the actual devices.

3.4 Reference Measurements

Prior to the actual sensing investigations the influence of the electrode geometry has to be investigated. It is known from literature that a thin water film can be electrical conductive for sufficiently high electrical fields depending on the electrode geometry. Therefore the used electrode structure with an electrode-to-electrode distance of 2 µm is investigated in dependency on the applied voltage. To imitate a very high humidity, simple breath-on experiments have been done which lead to obvious humidity condensation between the electrodes. The results for different voltages can be seen in Figure 52 on the left. The breath-on experiments starts at 10 s reflected by

the increasing current for higher voltages. Afterwards, the condensed humidity desorbs again which is reflected by the following current decay. As can be seen, there is a clear influence for voltages above 1 V. To summarize these findings the plateau values of the current has been plotted versus the applied voltages as shown by the right graph of Figure 52. As it is evident, the influence becomes recognizable for 1.5 V and higher. Therefore, all further experiments have been limited to a maximum voltage of 1 V. This is reasonable because of two reasons: 1) the breath-on experiments represent a humidity condensation and by that an overestimation of the actual experiments which has been limited to 80 % humidity to prevent condensation; and 2) U / I non-linearity starts for voltages above 5 V as has been discussed in section 3.3.4, which means linear behaviour for 1 V and by that no non-linear influences during the actual sensing experiments.
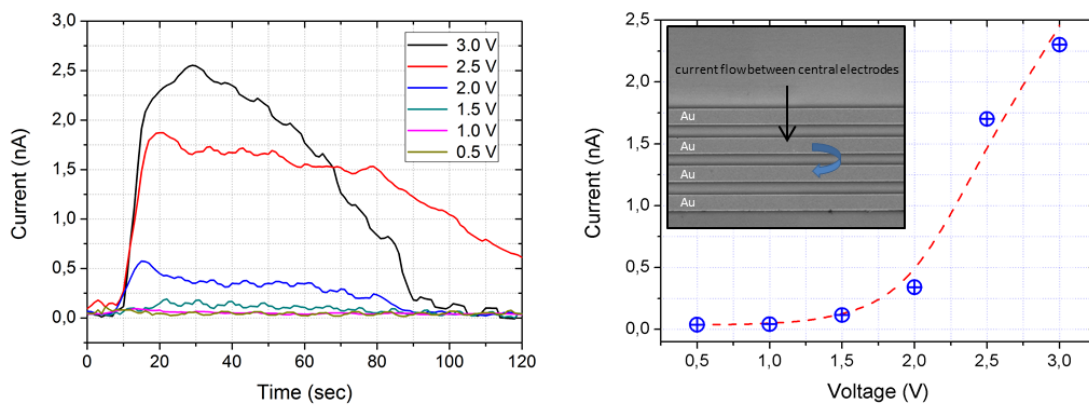
Figure 52: left: voltage related currents for a 10 nm deposit at condensed phase measurements; right: current increase versus applied voltage with a SEM inset to show the measurements situation.

The second aspect concerns possible electromigration effects for the Pt nanograins as discussed in section 3.3.4. A comparable narrow PtC deposit with a width of 500 nm was subjected to a 1 week operation at 1 V in ambient conditions. Figure 53 shows the mentioned PtC deposit between the Au electrodes after the long-time operation via a SEM image (top). In the bottom, an X-ray (EDXS) based elemental map of Pt (green) for the same area is shown which indicates no tendencies of any electromigration along the deposit. Please note, the relevant X-ray lines for Au and Pt are very close together which explains the green appearance for the electrodes as well. The used deposit is on purpose much more narrow compared to the real footprints used for the sensors (500 x 2000 nm versus 5000 x 2000 nm) to establish more critical conditions towards electromigration.
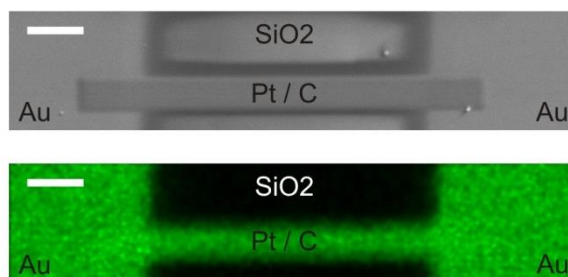
Figure 53: SEM image of a PtC deposit between two Au electrodes (top) after 1 week permanent operation at 1 V. The bottom image shows an Pt elemental map via EDXS of the same area (green), revealing no inhomogeneous distribution of Pt along the deposit, hence, excluding electromigration effects for the operation conditions used (white scale bar is 500 nm).

In conclusion we found that 1) the used electrode structure does show a negligible influence of ionized water for voltages of 1 V and less; and 2) electromigration is not an issue for PtC deposits used in this thesis operated at 1 V or less. By that, the actual sensing experiments can be started which will be discussed in the following section.

3.5 Sensing Capabilities

In the following the PtC deposits have been systematically investigated on their response upon defined humidity exposure. In more detail, the response in the gaseous phase will be discussed in section 3.5.1 including their reversibility, selectivity, quantitative characteristics and temperature related influences. Section 3.5.1 focuses then on basic effects during condensed phases. Section 3.5.3 discusses the suggested working principle for the PtC sensors which is supported by theoretical modelling in section 3.5.4. Finally, section 3.5.5 focuses on the fact that the PtC devices work with nanocurrents and introduce a simple approach how such low currents can be used for driving macroscopic low cost equipment in order to underline the practical and economic aspect of the developed sensors.

3.5.1 Gaseous Phase

Figure 54 shows the relative current response (top panels) of PtC sensors upon humidity exposures for 5 nm (left) and 60 nm (right) devices. As can be seen by the correlated chamber humidity (central panels), the relative current variation, normalized to the initial current, reacts synchronic to humidity variation. The PtC deposits react very fast in a sub-10 sec range for increasing humidities but with a delay for decreasing humidity levels. This can be explained by water molecules residing on the deposit surface before they are completely desorbed again. A closer look to the 5 nm deposits show also a small spike at the beginning which is attributed to condensation heat on a molecular level due to the rapid humidity increase. However, this could only be observed for very thin devices which will be discussed later in section 3.5.3. The next important detail is the different current variation which has been found to be lower for increasing thicknesses. The most important detail, however, is the fact that cyclic humidity exposure confirms a reversible character of the current and by that a reversible device characteristic which is essential for their practical application. This suggest strongly that the effects, responsible for the electric response, are more based on physisorption and

desorption than on chemical effects which tend to show irreversible characteristics. Finally, the bottom panels in Figure 54 show the corresponding temperatures of the substrate and the gas phase which have been found widely constant. Nevertheless, the influence of temperature has to be discussed which can be found in the following section 3.5.1.1.
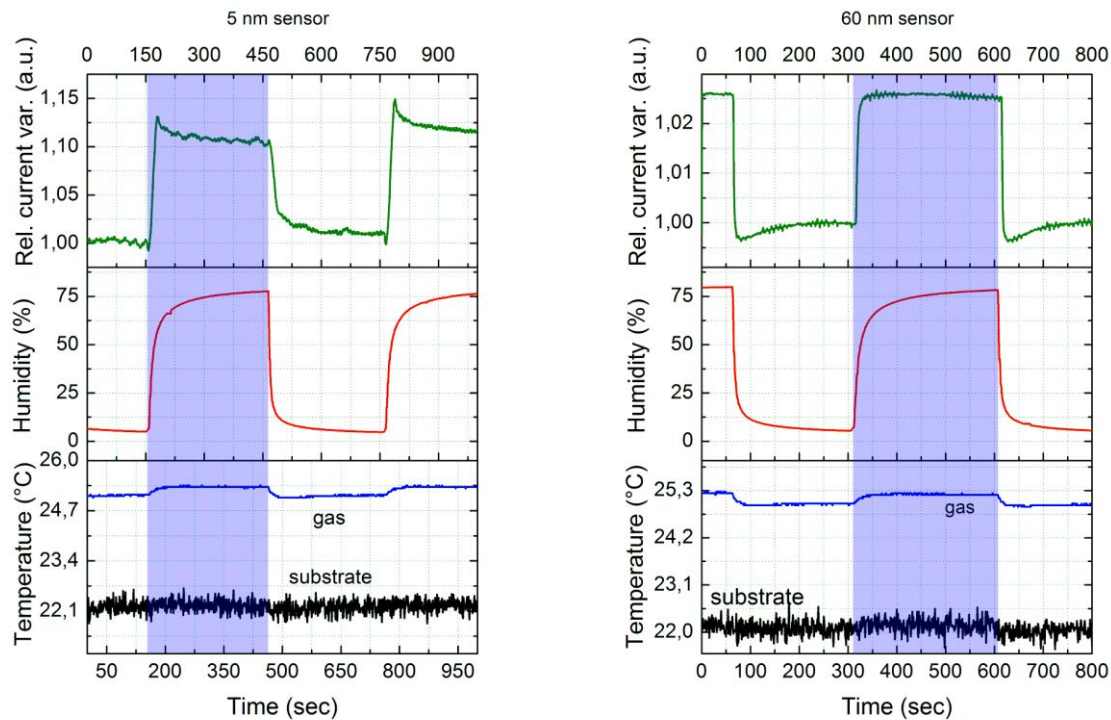
Figure 54: relative current response (top) in dependency on humidity cycles (5-80%) (center) together with substrate and gas phase temperatures (bottom) for 5 nm (left) and 20 nm (right) PtC devices. The blue bars indicate the humidity exposure period.

3.5.1.1   Temperature Related Effects

As can be seen in Figure 54 (bottom panels) there is low temperature response of the gas phase upon humidity exposure which has been found to be less than 0.5 °C. Furthermore, there is a temperature difference between the gas phase and the substrate of about 3 °C. To exclude a temperature influence to the sensor characteristics shown in Figure 54 (top panels), temperature dependent current measurements have been performed under vacuum conditions. Figure 55 shows the relative current variations for different device thicknesses in a temperatures range of 10-45 °C via the Peltier heating stage (section 2.3.3). For the full temperature range, it can be seen that the 5 nm device varies about 10 %, which is quite much compared to the highest current variation of 12 %. However, assuming a maximum temperature variation of 6 °C, based on the difference between substrate and gas phase (red bar in Figure 55), the respective current variation can be estimated to about 1 % (green bar in Figure 55) for thinnest PtC devices. Hence, although influencing the final performance, local temperature effects can be widely excluded as main driving force for the current variations upon humidity exposure.
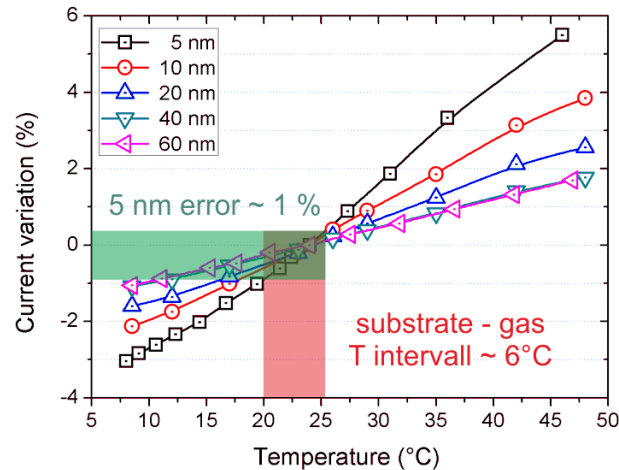
Figure 55: influence of substrate temperature on the device current for 10 – 45 °C for different layer thicknesses. The red bar indicates the overestimated temperature range while the green bar represents the maximum influence on 5 nm devices.

3.5.1.2 Qualitative Sensing Performance

In order to attribute the current response to one or more gas species, the sensing characteristics of the PtC sensors have been investigated for individual gas species: N_2, O_2, CO_2, H_2O and for vacuum conditions. The motivation behind this gas selection was the chemical composition of ambient air. The experiment started with vacuum conditions, followed by N_2 exposure up to ambient pressure. Such pre-experiments revealed no change of the current. Hence, N_2 as detectable analyte can be excluded. Afterward, three different experiments have been conducted with vacuum and N_2 flushing steps in between: 1) 80 % H_2O, 2) pure O_2 (> 99,99 % purity), and 3) CO_2 (> 99,99 % purity). Figure 56 shows the summary of these experiments with a 20 nm device where the left hand side shows always the N_2 state followed by a 60 sec custom gas exposure specified above. As can be seen, in case of exposure to polar gases, like water vapour, the current is increased and reaches initial values when the amount of water molecules in the measurement cell is decreased again. However, the currents are not changed during contact with O_2 or CO_2 which are both non-polar gases. Even in case of chemical reactive gas species like pure oxygen the current stays almost the same, indicating that the chemical structure of the deposits is stable and the current variation is not caused by chemical reactions between the gas species and the PtC sensors. Hence, we conclude that the reversible response is mainly caused by polar analytes like water.
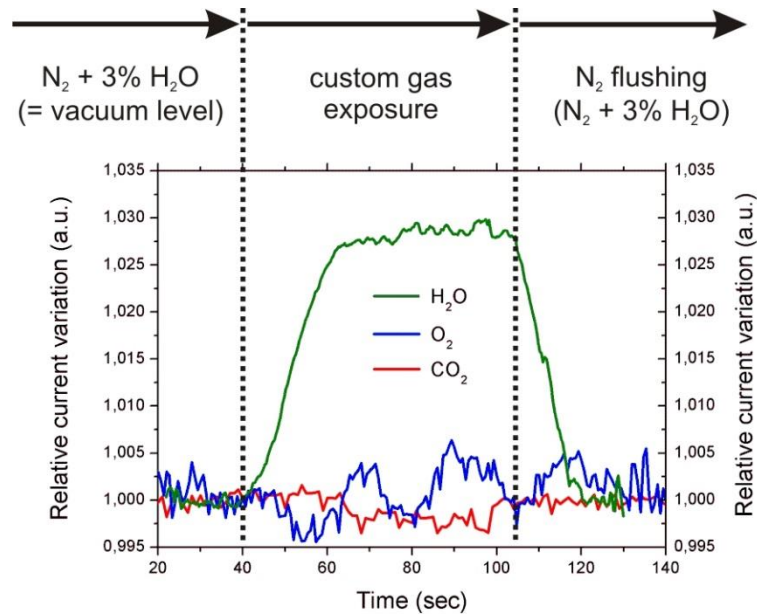
Figure 56: current response of a 20 nm PtC sensor during H_2O, O_2, and CO_2 exposure. The vacuum value has been found identical to pure N_2.

3.5.1.3   *Quantitative Sensing Performance*

The final step is the investigation on quantitative sensing capabilities. Defined humidity control was used together with current measurements for differently thick PtC sensor devices summarized in Figure 57. All values have been normalized to the currents at 5 % humidity since the experiments have not been done at the same day and the lowest achievable humidity level was varying between 2 and 5 %. As can be seen the current response allow quantitative humidity measurements for all device thicknesses. However, thinner deposits show a stronger current increase than thicker PtC devices. Furthermore, thin depositions react significantly more sensible to changes of the humidity level, especially at very low values (black curve). Higher humidity levels, in contrast, lead to a flattened but still usable increase of the electric current as the surface gets more and more covered with water molecules. For thicknesses above 20 nm the difference between the current responses is less significant. This increase in sensitivity for thinner deposits has already observed before by means of resistivities (Figure 49) and motivated to take a closer look on its dependency.

Figure 58 shows the relative current increase at a level of 75 % humidity in dependency on the device thickness. As it can be seen, the sensitivity is strongly increased for devices below 20 nm thickness. From these observations it can be concluded that the current variation is caused by a limited interaction depth of the physisorped water molecules with the nanogranular deposition and more dedicated to a thin surface layer (see skin effect in section 3.3.3) than to a bulk effect. By that, a diffusion effect deep inside the deposit can also be excluded as main driving force for the observed sensing effect.
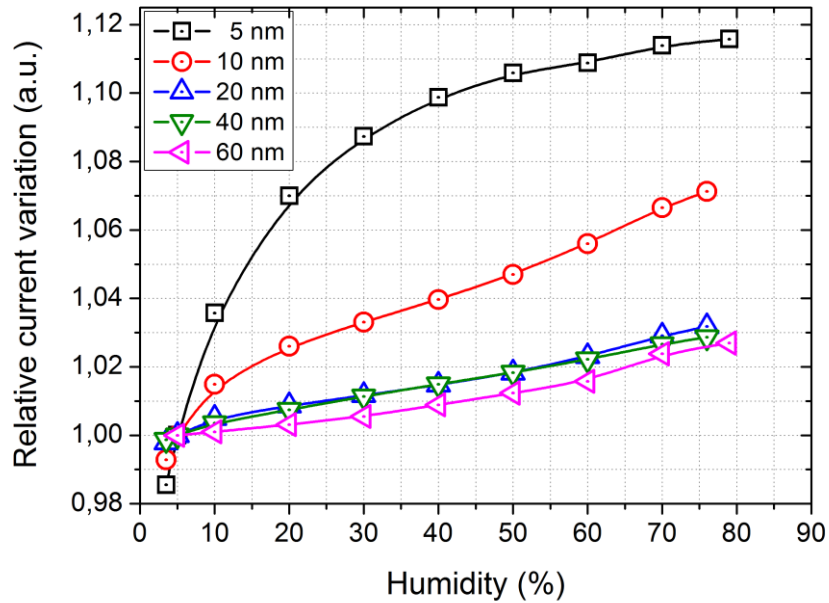
Figure 57: relative current variations for deposits with varying height at different humidity levels (referenced to 5 %).
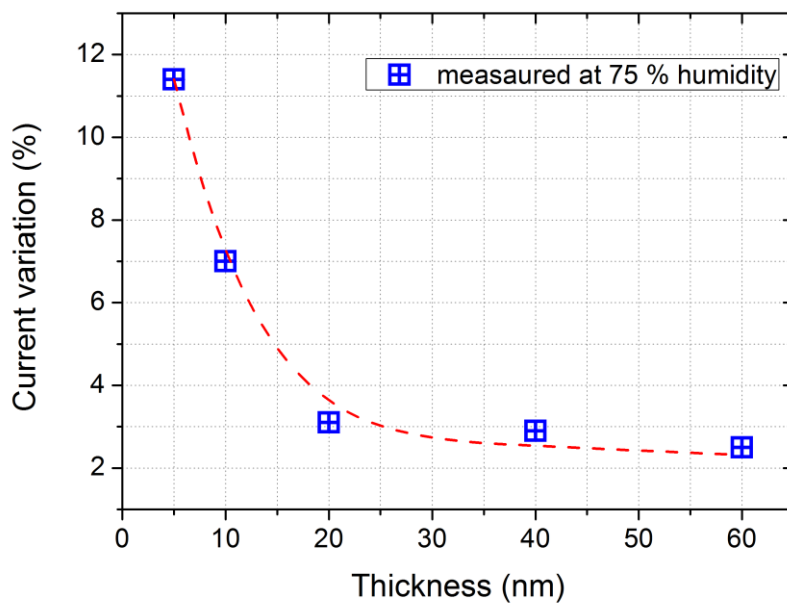
Figure 58: current variation in dependency on the layer thickness for identical humidities of 75 %.

3.5.2   Condensed Phase

Finally, it was interesting to investigate the response during a condensed phase of water on the PtC sensors. Figure 59 shows the response of a 20 nm device exposed to thin water films (~ 37 °C) covering the whole surface of the deposition. As it already has been observed during the exposure to

gas phases the sensor reacts very fast to the presence of the water film. The currents response, however, is much higher as for gas phase exposure (about 700 %, see right axis) at even highest level (80 % humidity). Desorption of the water film leads to a steady decay of the electric current until the initial value is reached again, proving also reversibility for condensed phases. However, this process takes a longer period due to a more complicated desorption situation by diffusion and slow evaporation.
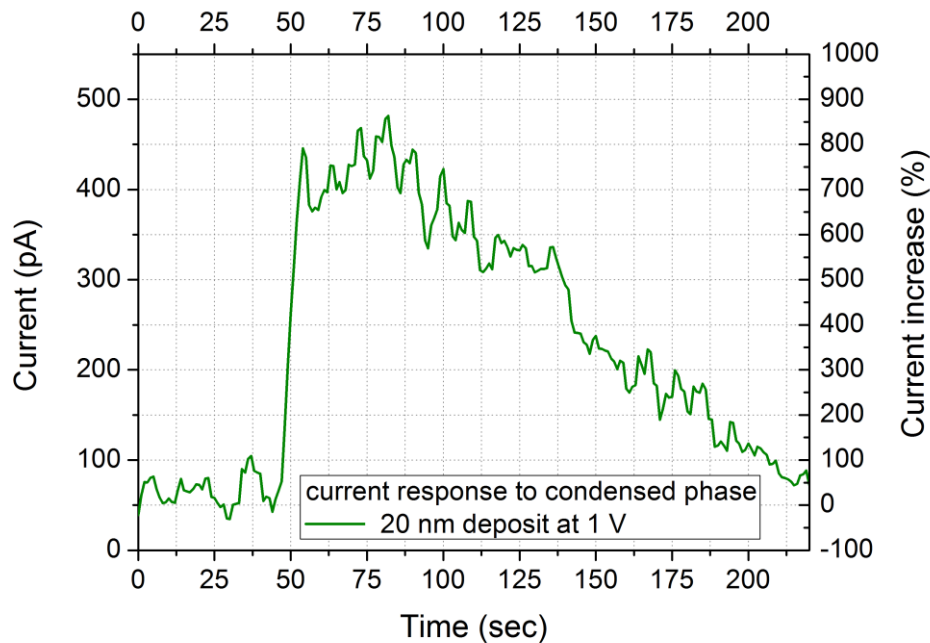
Figure 59: current variation of a 20 nm PtC sensor during a condensed phase measurement at an applied voltage of 1 V.

Cyclic condensation and evaporation at room temperature of the water film on PtC devices causes a according and reversible reaction of the measured current as shown in Figure 60 (condensed phase pulses are indicated by the red bars). This supports further, that chemical effects are not a main effect in contrast to more likely physisorption on the surface. The spike at the beginning of each condensation process can be explained again by higher temperature due to condensation heat of water on a surface, hence, improving the conductivity of the deposits. The oscillating behaviour of the decreasing current can be caused by the temperature related effects during the vaporization of the water molecules but are more likely a measurement artefact. An astonishing result, however, are the achievable jump ratios of about 20 and more (without the initial spike). This opens new application possibilities as wetting sensor (e.g. rain sensors) while the reversibility allows to think about applications in liquid environments.
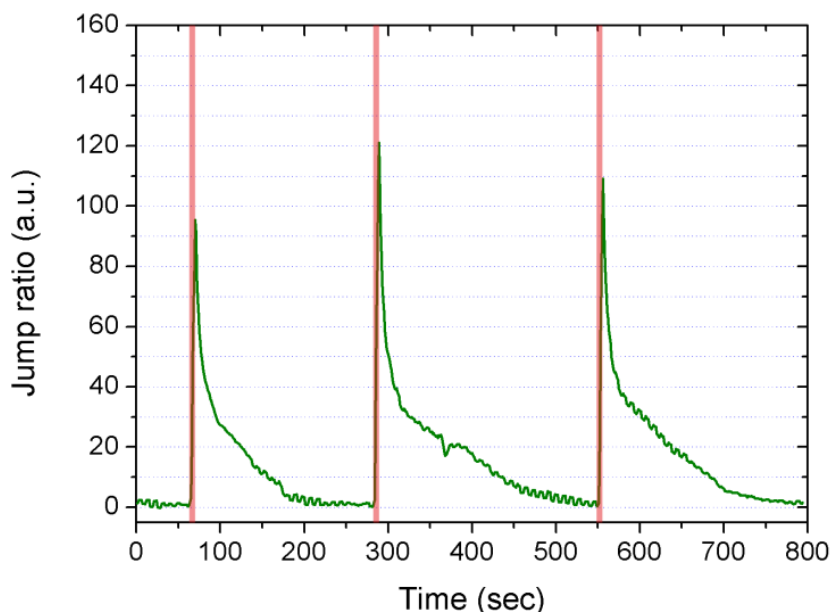
Figure 60: massively increased current responds to cyclic condensed phase measurements indicated by the red bars.

3.5.3 Model

Summarizing the experimental results obtained during the investigations of the sensing capabilities, we can state that the change of the currents induced by a variation of the humidity levels is not caused by the temperature variation of the gas phase or the substrate. The FEBID layers responds to an exposure to water vapour, which is a polar gas, while it is not affected by nonpolar gas species like O_2, CO_2 or N_2. The sensitivity of the sensors strongly increases for decreasing layer thicknesses (especially below 20 nm). The sensor response to a variation of the humidity level is **fast**, **reversible**, and it **scales with the quantity** of water vapour in the gas phase. Meaning that an increased vapour level entails higher current variations. The strongest response was observed during condensation of the water vapour at very high humid levels (< 90%) based on the massive increase of water molecules physisorped on the sensor surface. The aim of this chapter is to define a theoretic model explaining the behaviour of the FEBID when exposed to humid environments or more general to polar gases / liquids. Figure 61 schematically shows the situation during the experiments. The FEBID structures are deposited across the Au electrodes and consist of nanogranular Pt particles (blue spheres) embedded in an insulating carbon matrix (green). The Pt particles have diameters of 2-3 nm and are randomly distributed over the whole deposit volume with a finite distance between each other in the Å range [12,15,16,17]. Applying a voltage to the electrodes leads to a polarization of the dielectric carbon matrix in between individual Pt grains as shown in Figure 62 by the black vector (E_{CARBON}). The polarization field acts contrary to the applied electric field, resulting in a final electric field between the Pt grains which is smaller than the initial electric field defined by the derivative of the applied voltage (red vector E in Figure 62). Consequently, the charge transport determined by a field dependent tunnelling probability is suppressed (section 2.1.10.4) and only a small electric current is measured.
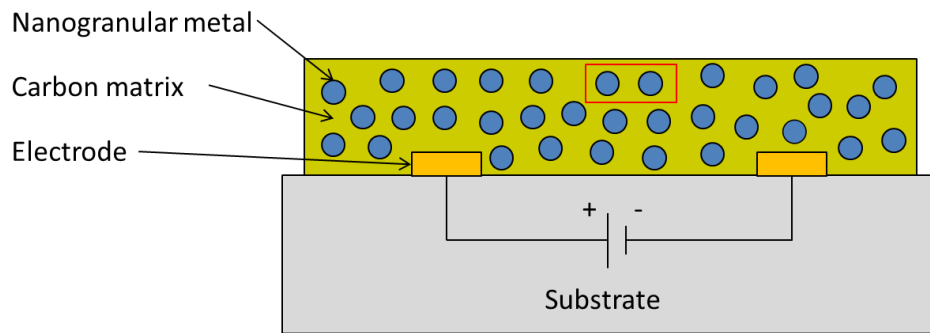
Figure 61: schematic of the situation during the different characterization experiments

When a polar molecules approaches the surface of the FEBID structure the electric dipole moment of the adsorbed molecule and the electric field of the dielectric carbon matrix (E_{CARBON}) start to interact. This leads to a rotation of the polarization field *out-of-plane*, which reduces the *in-plane* component of the polarization field between two adjacent nanograins while the electric field E of the applied voltage stays the same (Figure 62 at the right). Superposition of both electric fields results in a higher *in-plane* electric field between two neighbouring nanograins. This, however, influences the tunnelling probability from one grain to the next one which increases the *in-plane* current across the device (see Figure 62 at the right). As a result the measured currents with adsorbed polar molecules are higher compared to FEBID structures in vacuum or exposed to non-polar gases, due to the absence of any dipole momentum.
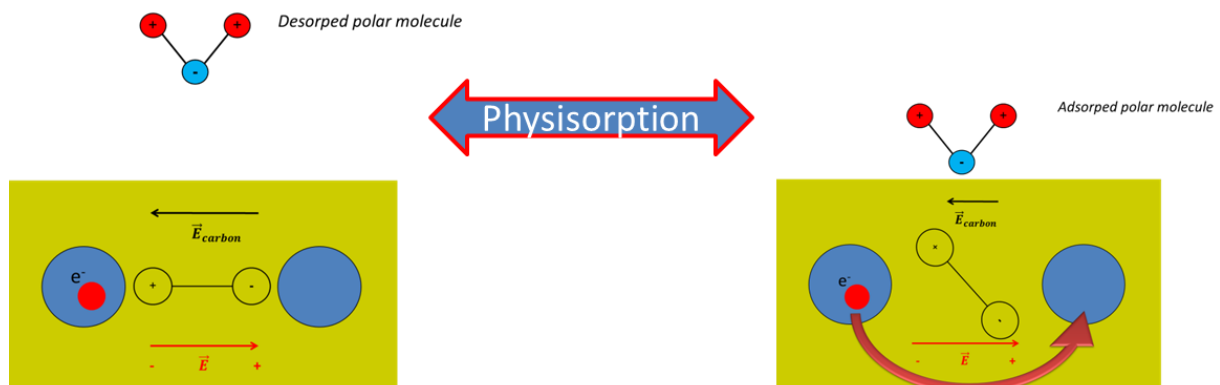
Figure 62: schematic visualization of the theoretic model developed to explain the current variation due to the exposure to polar gases. The polarization field of the carbon matrix is indicated as $\vec{E}_{carbon}$ (black arrow), while $\vec{E}$ is for the electric field of the applied voltage during measurement (red arrow). Right: physisorbed polar molecules interact with the carbon matrix dipole $\vec{E}_{carbon}$ which leads to an increasing electric field between the Pt grains resulting in higher tunneling probabilities.

The height dependency of the current variation as discussed in section 3.5.1.3 can be explained through the limited interaction depth between polar molecule and carbon matrix, involving only the topmost layers of the nanogranular structure: the skin effect (see section 3.3.3). Due to the reversibility observed during the measurements with a varying humidity level the molecules are considered to be physisorped at the surface of the deposit. Hence the interaction process between the molecule and the polarization field does not lead to permanent binding of polar molecules on the surface of the structure which is in agreement with both theory and experiment.

However, to investigate the interaction process between the electric field of the dielectric matrix and the electric dipole moment of the molecule in more detail further studies are currently subject of investigations. These studies could for example answer the question if there is a significant change of the current variations responding to the exposure to polar gases / liquids while a high frequency AC voltage is applied. Further studies could be also concerned on the investigation of the interaction length between polar molecules and dielectric matrix, resulting in the definition of an optimal height of FEBID deposits, working as sensors for polar molecules. The result of these investigations would lead in the development of nanostructures having high current variations responding to the varying amount of polar molecules, while the responding behaviour is not being affected of influences induced by the adjacent substrate.

3.5.4 Theoretical Background

While the model developed in chapter 3.5.3 described the variation of the currents as an interaction process of an adsorbed polar molecule with the polarization field of the dielectric carbon matrix, the aim of this chapter is to expand the theoretic model to the behaviour of nanogranular structures in the c-VRH regime. Figure 63 gives a graphically survey of the different coupling / conduction regimes that are encountered for nanogranular structures in dependence of the coupling strength g, the number of neighbours adjacent to a grain side z and the temperature applied during measurements. For further details concerning the functional behaviour of the conductivity and their parameters for structures in the c-VRH regime presented in Figure 63 the reader is referred to chapter 2.1.10.4. The resulting formalism describing the origin of the sensing capabilities mathematically was provided by Prof. Dr. Michael Huth (Institute for Physics, Goethe University, Frankfurt, Germany).
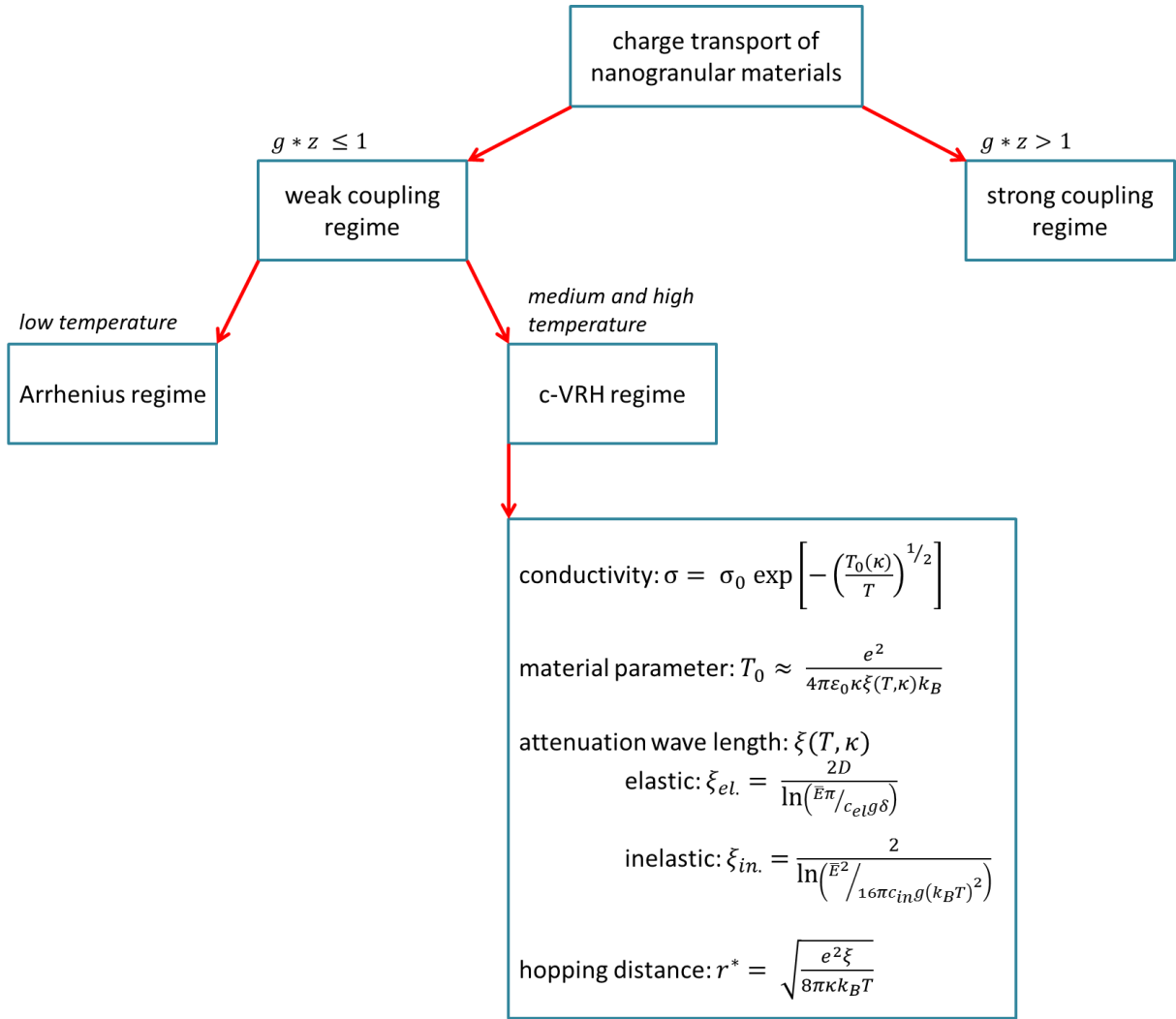
Figure 63: survey of the charge transport for nanogranular material in the different coupling / conduction regimes.

In general the polarization of a dielectric material is defined as $\vec{P} = \varepsilon_0(\kappa - 1)\vec{E}_{appl.}$ with $\vec{E}_{appl.}$ as the derivative of the applied voltage and κ as the relative permittivity, also called *dielectric constant*, of the nanogranular material. The polarization field can be varied by the applied electric field or by changing the relative permittivity. In accordance to the developed theoretic model the *in-plane* component of the polarization field between two neighbouring grain sides is reduced by a variation of the relative permittivity. Consequently, a parameter has to be defined that takes the dependency of the conductivity on the relative permittivity into account. The mathematic expression of this parameter resembles to the so called *gauge factor*, developed by Prof. Dr. Michael Huth to describe the variation of the conductivity in dependence of the changing average grain separation encountered at the nanogranular stress-strain sensor. In our case the parameter is called *sensitivity factor* and is defined as the ratio of the relative change of the conductivity to the relative change of the dielectric constant:

$$\lambda = \frac{\Delta\sigma/\sigma}{\Delta\kappa/\kappa} = \frac{\kappa}{\sigma}\frac{\partial\sigma}{\partial\kappa} \qquad\qquad \text{Equation 15}$$

Applying the equations, preliminary introduced in chapter 2.1.10.4 (or else see Figure 63), describing the functional behaviour of the conductivity for nanogranular structures, the sensitivity reads as:

$$\lambda = \frac{\Delta\sigma/\sigma}{\Delta\kappa/\kappa} = \frac{e^2}{8\pi\varepsilon_0 Da\xi_{in}k_B(T_0(\kappa)T)^{1/2}} = \frac{1}{4}\frac{e}{\sqrt{\pi\varepsilon_0\kappa D\xi_{in}k_B T}} \qquad \textbf{Equation 16}$$

The sensitivity is increased for nanostructures with a small grain size and at low temperatures. Furthermore, with the knowledge of the sensitivity it is now possible to estimate the relative change of the conductivity (equal to the relative current variations) in dependence of the relative change of the dielectric constant. It has to be noted at this point that the sensitivity depends on the (inelastic) attenuation wave length, whose value is controlled by the coupling strength g and the geometrical averaged excitation energy $\overline{E}$, both influenced by the dielectric constant. However, due to the logarithm in the denominator of the inelastic wave attenuation, whose argument is always greater than 1 the dependence could be considered as very small.
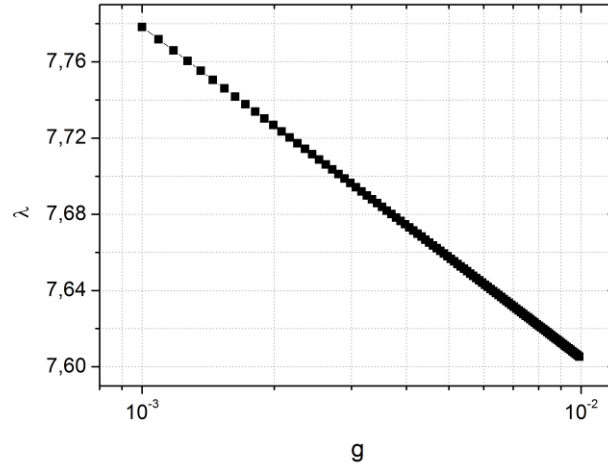
Figure 64: functional behaviour of the sensitivity factor in dependence of the tunnel coupling *g*.

Figure 64 shows the functional behaviour of the sensitivity in dependence of the tunnel coupling. A change of the coupling strength by one order of magnitude leads to a relative variation of the sensitivity by approximately 2 %. To finally correlate the electrical conductivity variation with the relative dielectric *in-plane* constant, according simulations have been performed which are shown in Figure 65. These calculations assume a PtC device of 5 nm, resembling a quasi-monolayer system of the nanogranular material with a grain size D of 3 nm, a dielectric constant κ of 2 and a coupling strength of 10^{-3} to 10^{-2}. The results of this numerical estimations revealed that a variation of the relative dielectric constant of 1 % leads to a change of the relative conductivity of 7 %. Compared to the observed 12 % current variation for 5 nm devices (see chapter 3.5.1.3), these simulations suggest an in-plane variation for the dielectric constant of about 2 % as can be seen in Figure 65. Finally, it should be noted that the dependence of the dielectric constant on the tunnel coupling is considered to be only implicit [14].
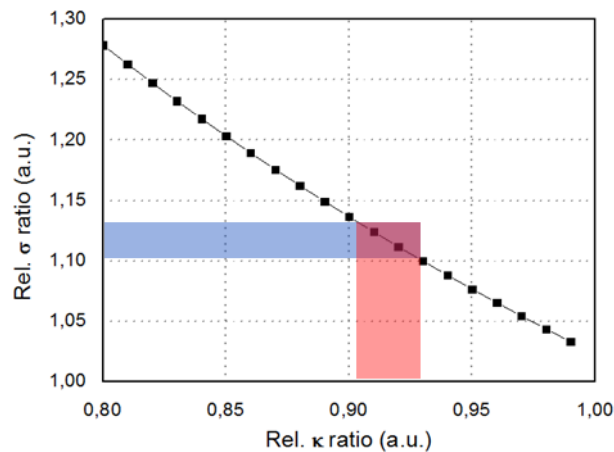
Figure 65: relative conductivity variation in dependency on the dielectric constant of the carbon matrix.

While the variation of the tunnel coupling parameter with a factor of 10 results only in a change of the conductivity by 2 % , a small change of the relative dielectric constant of 1 % leads to a variation of the relative conductivity by 7 %. This suggests that the influence of the tunnel coupling **g** on the sensitivity **λ** is very small and the change of the conductance during an exposure to polar gases is driven by a variation of the dielectric constant of the nanogranular material, which leads to a variation of the tunnel probability between two grain sides. However, further investigations need to be done to approve this concept, including simulations concerning the actual charge transport in the nanogranular PtC structure and the definition of proper dielectric constants for the metal / matrix system.

3.5.5 Nano drives Macro – A Practical Approach to use PtC Nanosensors

Encouraged by the results obtained during the investigations of the sensing abilities a device was designed to visualize the response without the necessity of extremely expensive equipment. The device represents the usability of current variations on nanoampere scale and by that the high potential of such sensors for simple applications. The device contains a RGB LED which changes its colour if the resistivity of the deposits reacts to humid environments. This can be done by transforming the change of the resistivity into a change of the voltage which affects subsequently the voltage applied on the RGB LED. The conversion of the resistivity change into a voltage change is realized by the integration of the deposit in a Wheatstone bridge. The realization of the demonstration box was kindly supported by Manuel Jelinek.
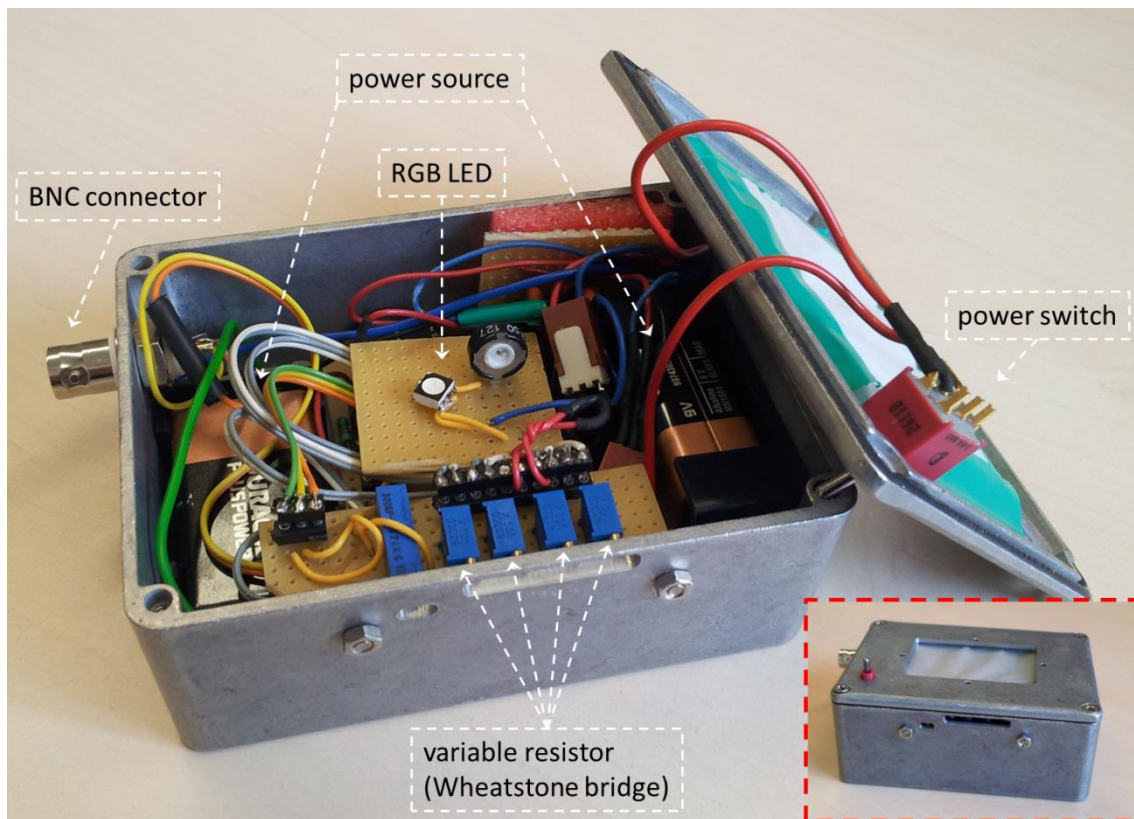
Figure 66: interior view on the demonstration box; front view of the assembled demonstration box (inlet)

The demo box shown in Figure 66 consists of two 9 V batteries supplying the electric circuit with the required power. Voltage regulators (L7805, STMicroelectronics) change the battery voltage into 2 different potentials with +5 V and − 5 V, which are required for the instrumentation amplifier (AD 620, Analog Devices) and the operational amplifier (MC33204, ON semiconductors). The Wheatstone bridge is realized by fixed and variable resistors. The RGB LED in the SMD design consists of three different LED emitting the colour red, green and blue. If the emission of all three LEDs has the same intensity the emitted light has a bright white colour. Figure 67 shows the arrangement of the electronic devices of the demonstration.

The PtC sensors are mounted on a specimen holder which was originally designed for active AFM investigations for same sample layouts. In the next step the specimen holder and the demonstration box is connected by a BNC cable. The Wheatstone bridge is brought into balance by adjusting the variable resistors, which can be checked by the white emission of the RGB LED. Please note, that only fully settled PtC sensors have been used for these experiments (see section 3.3.2). Otherwise the Wheatstone bridge would move consistently out of its balance and the other variable resistors have to be constantly readjusted. If the resistance of the deposits changes intentionally due to the exposure to a humid atmosphere the Wheatstone bridge moves out of its balance, generating a voltage between point 1 and point 2, which are indicated in the circuit diagram in Figure 67. This voltage is amplified to 5 V and acts against the supplying voltage of the blue and green parts of the RGB LED. Consequently, the RGB LED changes its colour from white to red, as at the green and the blue LED are not supplied by a sufficiently high potential. If the humid level is decreased the resistance of the deposit reaches the initial value and the colour emitted from the RGB LED changes back from red to white.

Hence, even if the changes of the resistance or of the currents are very small when exposed to humid atmospheres it is nonetheless possible to make this effect visible by commonly used electronic components with only little efforts (total costs are less than 50 € for the entire prototype).

This demo box shows clearly how nano can drive macro devices with very low demands. It is conceivable that such devices can easily be integrated in printed circuit boards with self-adjusting Wheatstone bridges which are standard chips in semiconductor industries. Considering the fast preparation time of about 30 seconds in optimized geometries together with the currently introduce multi-electron-beam instruments on fab scale (about 500.000 beams simultaneously), the usage of such PtC sensors for special purposes seem to be very promising.
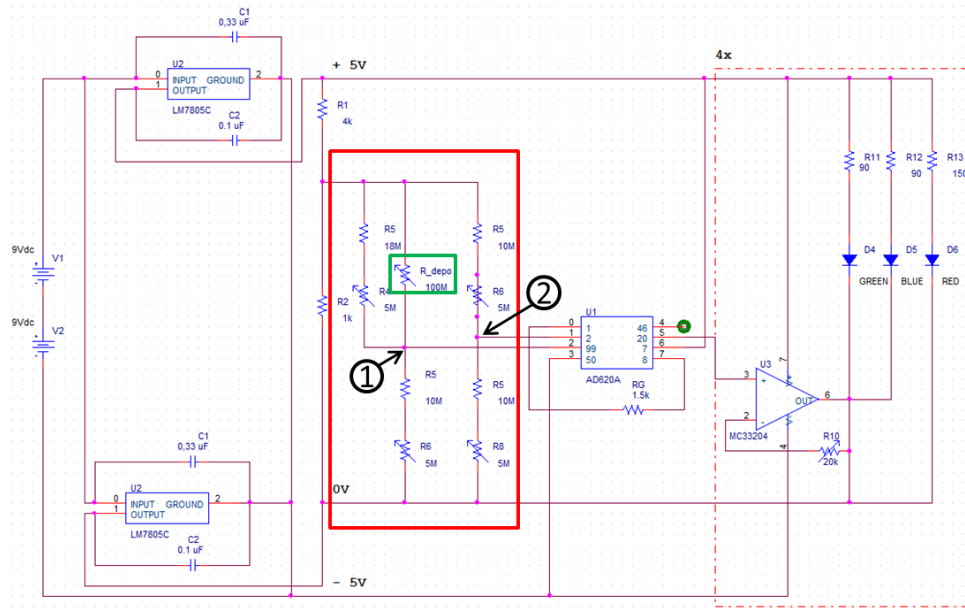
Figure 67: circuit diagram of the demonstration box; frames indicate the position of the Wheatstone bridge (red) and the deposition (green)

4 Summary and Outlook

This master thesis focuses on the development of a humidity sensor based on variable tunnelling barriers of nanogranular PtC metal-matrix materials fabricated via focused electron beam induced deposition (FEBID). The study is an advancement of the master thesis previously done by DI Stephan Georg Michelitsch at the FELMI (2011), which was more focused on feasibility studies of electrical *in-situ* measurements for the same nanogranular PtC material. During that thesis an electrical response of the PtC layers upon exposure to ambient conditions was observed for the first time. The current master thesis deepens the investigations concerning the behaviour of the PtC FEBID structures during specific exposure to humidity, O_2, N_2, and CO_2 at ambient pressure but also in vacuum conditions. The observed sensor characteristics are complemented by a theoretic model capable of explaining the observed behaviour together with calculations which are in good agreement with the experimental results.

The study starts with a correlation between deposition parameters and achieved layer thicknesses for different deposition regimes. Detailed electrical U / I characterizations of the fabricated deposits revealed a linear dependency for electrical fields below 2 V.μm^{-1} for all thicknesses and deposition regimes independently on the polarity. Higher fields lead to a non-linear behaviour of the U / I characteristics, independent on the thickness of the deposits. Long-time investigations revealed a self-curing process in which the resistivity increases asymptotically under ambient conditions. It is found that thinner devices settle much faster than thicker layers which suggest diffusion related effects of actually volatile products towards the deposit surface where they can leave and / or interdiffusion of radical groups leading to chemical reactions inside the carbon matrix as a result of the rapid dissociation process. Final resistivities of self-cured layers reveal a strong non-linear behaviour in dependency on the layer thickness with much higher resistivity values for very thin layers (2 orders of magnitude between 60 nm to 5 nm layers). This finding can be explained by the transition of the electrical transport from 3D (60 nm) towards 2D (5 nm) where a PtC quasi-monolayer determines the final electrical conductivity.

Prior to any gas response measurements, reference experiments have been performed to evaluate the cross influence of the electrode structure itself. It was found that operating voltages up to ±1 V are practically free of side effects which were then defined as working voltage for all further experiments. Furthermore, electromigration of the Pt nanograins during electric operation could also be excluded as cross influence.

Afterwards, the sensing experiments have been performed at the NTC Weiz. Cyclic increase from 5 % to 80 % humidity (mixed into N_2 atmosphere) leads to increasing electrical current through the PtC devices. The sensor response is fast (sub-10 sec range) and fully reversible without requiring any reformation cycles after the humidity level is decreased again to the starting level of 5 %. Since very small temperature variations are found during humidity increase / decrease, the temperature dependency has been investigated in vacuum. It is found that the temperature contributes with clearly less than 5 rel.-% of the total current response during humidity exposure which allows to exclude temperature effects as major driving force of the sensing effect.

Selective sensor exposure to N_2, O_2, CO_2 and humidified N_2 revealed an exclusive response to increasing H_2O levels. Hence, it can be concluded that only polar molecules induce an electric response of the devices. Furthermore, these selective gas experiments reveal that the PtC material is chemically stable and the response is not caused by chemical reactions between the analyte and the nanogranular structure. The reversibility during the cyclic humidity variations suggest therefore a physisorption effect of water molecules on the surface of the device.

Finally, defined humidity increase reveals the quantitative sensing abilities of the devices with strongly increased sensitivities for decreasing layer thicknesses: while only about 2 % current variation could be observed for 60 nm, a 12 % response is found for 5 nm devices. This characteristics show clearly that the effect is restricted to the topmost regions of the PtC layers instead of the bulk.

To explain the origin of the current variation caused by the exposure to polar H_2O gases a theoretic model is proposed. The main idea of this concept is that in nanogranular metal-matrix systems the final electrical current is governed by the tunnelling probabilities of charge carries between the Pt metal grains. This tunnelling is hindered by the insulating carbon matrix in between the Pt grains via an electrical counter-field generated by the applied external field according to the dielectric constant of the carbon matrix. Once a polar gas molecule is adsorbed on the PtC surface its electric dipole moment starts to interact with the polarization field of the carbon matrix. This reduces the carbon related tunnelling barrier and increases the tunnelling probability between Pt grains leading to an increasing macroscopic device current.

This model is physically reasonable and can explain the fast response (electrostatic effects), the reversibility (physisorption / desorption), the selectivity (only polar molecules contribute), the quantitative characteristics (proportional to the adsorbed dipoles) as well as the strong thickness dependency (only topmost layers can respond to this effect). Additional calculations, provided by Prof. Dr. Michael Huth, supports this theory by quantitative estimations which are in good agreement with the observed effects.

It seemed very important to us to demonstrate the application relevance of such sensors which work with currents in nano-Ampere range. As long as very expensive equipment has to be used for the read-out, the sensor advantages are of minor importance. Therefore, we have designed a simple electrical circuit which is basically included in many basic IC chips. The concept behind was a Wheatstone bridge which is brought out of balance once the sensor changes its current. The outgoing voltages controlled a simple RGB LED leading to a changing colour during the sensor response (Figure 68). This demo box enables us to show how nano drives macro with low efforts which demonstrate the potential of this concept to be used in special industrial applications.
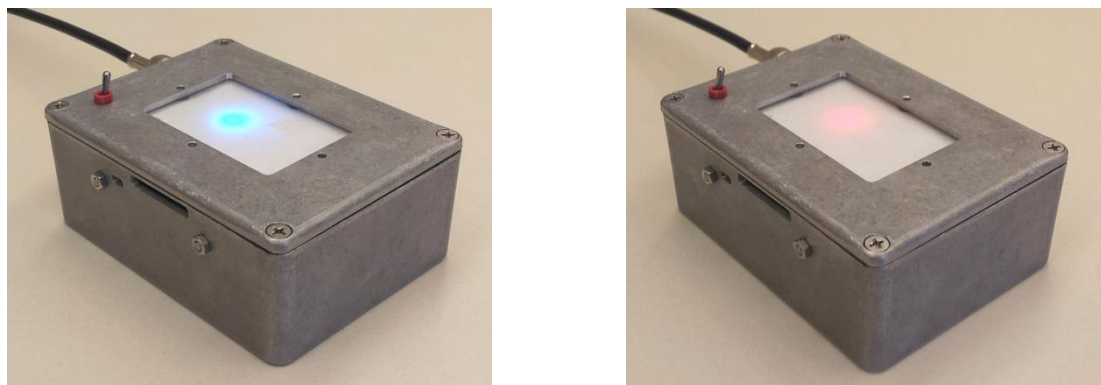
Figure 68: demo box connected to the PtC deposit; left: colour of the RGB LED at low humidity levels; right: increased humidity levels change the colour of the RGB LED

Finally, it has to be noted that the presented sensor is the first FEBID based gas sensor worldwide and the third FEBID sensing concept in general. The proposed model is based on the special charge transport properties of nanogranular metal-matrix systems and in agreement with numerical estimations based on the related theory. The concept itself is furthermore expandable to other sensing applications such as ions in liquids and electrical fields on the nanoscale which is subject of ongoing research projects at the FELMI. By this we hope to push FEBID based devices further towards industrial applications for special purposes due to the direct write character which allows a sensor fabrication even on non-flat surfaces where resist based techniques are unsuited.

Reference

[1] The FEI Company, Eindhoven, The Netherlands, www.fei.com

[2] Bruker Company, Billerica, USA , www.bruker.com

[3] Courtesy of Dr. Harald Plank, Institute of Electron Microscopy and Nanoanalysis, Graz University of Technology, Austria, **2013**.

[4] Volkert C A, Minor A M, *MRS Bulletin*, **2007**, 32, 389.

[5] Goldstein J, *Scanning electron Microscopy and X-Ray Microanalysis*, Plenum Press, **1992**.

[6] Drouin D, Couture A R, Joly D, Tastet C, Aimez V, Gauvin R, *Scanning,* **2007,** 29, 402.

[7] Giannuzi L A, Stevie F A, *Introduction to focused ion beams: instrumentation, theory, techniques, and practice*, Springer, New York, USA, **2005**.

[8] Orloff J, Utlaut M, Swanson L, *High Resolution Focused Ion Beams*, Kluwer Academic/Plenum Publishers, New York, **2002**.

[9] PdD Thesis by Dr. Meltem Sezen, Institute for Electron Microscopy and Nanoanalysis, Graz University of Technology, Austria, **2009**.

[10] Schmied R, Chernev B, Trimmel G, Plank H, *RSC Advances,* **2012**, 2, 6932.

[11] Master Thesis by Angelina Orthacker at the Institute for Electron Microscopy, Graz University of Technology, Austria, **2013**.

[12] Russell P E, Utke I *Nanofabrication using focused ion and electron beams: principles and applications* Oxford University Press New York 2012

[13] van Dorp W F, Hagen C W 2008 *J. Appl. Phys* **104** 1

[14] Huth M, Porrati F, Schwalb C, Winhold M, Sachser R, Dukic M, Adams J, Fantner G 2012 *Beilstein. J. Nanotechn.* **3** 597.

[15] Plank H, Gspan C, Dienstleder M, Kothleitner G, Hofer F 2008 *Nanotechnology* **19** 485302.

[16] Plank H, Haber T, Gspan C, Kothleitner G, Hofer F 2013 *Nanotechnology* **24** 1753605.

[17] Plank H, Michelitsch S G, Gspan C, Hohenau A, Krenn J, Kothleitner G, Hofer F 2011 *J. Vac. Sci. Technol. B* **29** 051801.

[18] Plank H, Smith D.A, Haber T,Rack P.D, Hofer F, ACS Nano, 6, 1, 286 - 294, **2012**.

[19] Botman A, Mulders J J L, Hagen C W 2009 *Nanotechnology* **20** 372001.

[20] Master Thesis by DI Roland Schmied, Institute for Electron Microscopy, Graz University of Technology, **2011**.

[21] Porrati F, Sachser R, Schwalb C H, Frangakis A S, Huth M 2011 *J. Appl. Phys.* **109** 0637151.

[22] van Dorp W F, Wnuk J D, Gorham J M, Fairbrother D H, Madey T E, Hagen C W 2009 *J. Appl. Phys.* **106** 0749031.

[23]Beloborodov I; Lopatin A; Vinokur V; Efetov K, *Rev. Mod. Phys.* **79** (2), S. 469–518, **2007**.

[24] R. C. García, *Amplitude modulation atomic force microscopy*, Weinheim, Chichester: Wiley-VCH; John Wiley, **2010**.

[25] Master Thesis by DI Stephan Georg Michelitsch, Institute for Electron Microscopy, Graz University of Technology, **2011**.

[26] Keithley Inc., United States, www.keithley.com

[27] National Instruments, United States, www.ni.com

[28] Origin 8.5, OriginLab, www.originlab.com

[29] LabVIEW 10.0, National Instruments, www.ni.com

[30] Matlab 2007b, The MathWorks, www.mathworks.de

[31] NanoTecCentrer Weiz Forschungs gmbH, www.ntc-weiz.at

[32] Diplomarbeit by DI Gerhild Wurzinger, Institute of Solid State Physics, Graz University of Technology, **2009**.

[33] Courtesy of Dr. Andreas Klug, NanoTecCenter Weiz Forschungsgesellschaft mbH, **2013**.

[34] Agilent Technologies, United States, www.agilent.com

[35] Gazzadi G C, Frabboni S, *Appl. Phys. Lett.* **94**, 173112, **2009**